APR 21 1997 0830-L-02 NASI.29/3-2:97-04

NASA TechBriefs

National Aeronautics and
Space Administration

Electronic Components and Circuits

Electronic Systems

Physical Sciences

Materials

Computer Programs

Mechanics

Machinery

Fabrication Technology

Mathematics and Information Sciences

Life Sciences

97-04

COMPLETED

April 1997

NE 98-034708

INTRODUCTION

Tech Briefs are short announcements of new technology derived from the research and development activities of the National Aeronautics and Space Administration. These Briefs emphasize information considered likely to be transferable across industrial, regional, or disciplinary lines and are issued to encourage commercial application.

Availability of NASA Tech Briefs and TSP's

Distribution of NASA Tech Briefs, a monthly periodical publication, is limited to engineers in U.S. Industry and to other domestic technology transfer agents. Requests for individual Tech Briefs or for Technical Support Packages (TSP's) announced herein should be addressed to

NASA Center for AeroSpace Information
Technology Transfer Office
800 Elkridge Landing Rd.
Linthicum Heights, MD 21090-2934
Telephone No. (301) 621-0245

Please reference the three-letter, five-digit control number located at the end of each Tech Brief. Information on NASA's Technology Utilization Program, its documents, and services is also available at the same facility.

Technology Utilization Officers and Patent Counsels are located at NASA field installations to provide technology-transfer access to industrial users. Inquiries can be made by writing to NASA field installations listed below.

Technology Utilization Officers and Patent Counsels

Ames Research Center
Technology Utilization Officer
Mail Code 223-3
Moffett Field, CA 94035

Patent Counsel
Mail Code 200-11
Moffett Field, CA 94035

Goddard Space Flight Center
Technology Utilization Officer
Mail Code 702-1
Greenbelt, MD 20771

Patent Counsel
Mail Code 204
Greenbelt, MD 20771

Lyndon B. Johnson Space Center
Technology Utilization Officer
Mail Code IC-4
Houston, TX 77058

Patent Counsel
Mail Code AL3
Houston, TX 77058

John F. Kennedy Space Center
Technology Utilization Officer
Mail Stop PT-PMO-A
Kennedy Space Center, FL 32899

Patent Counsel
Mail Code PT-PAT
Kennedy Space Center, FL 32899

Langley Research Center
Technology Utilization Officer
Mail Stop 143
Hampton, VA 23665

Patent Counsel
Mail Code 279
Hampton, VA 23665

Lewis Research Center
Technology Utilization Officer
Mail Stop 7-3
21000 Brookpark Road
Cleveland, OH 44135

Patent Counsel
Mail Code LE-LAW
21000 Brookpark Road
Cleveland, OH 44135

Jet Propulsion Laboratory
Technology Utilization Officer
Mail Stop 156-211
4800 Oak Grove Drive
Pasadena, CA 91109

NASA Resident Office-JPL
Technology Utilization Officer
Mail Stop 180-801
4800 Oak Grove Drive
Pasadena, CA 91109

Patent Counsel
Mail Code 180-801
4800 Oak Grove Drive
Pasadena, CA 91109

George C. Marshall Space Flight Center
Technology Utilization Officer
Code AT01
Marshall Space Flight Center,
AL 35812

Patent Counsel
Mail Code CC01
Marshall Space Flight Center,
AL 35812

John C. Stennis Space Center
Technology Utilization Officer
Code HA-30
Stennis Space Center, MS 39529

NASA Headquarters
Technology Utilization Officer
Code CU
Washington, DC 20546

Assistant General Counsel for Patent Matters
Code GP
Washington, DC 20546

Dryden Flight Research Center
Technology Utilization Officer
M/S D21-31
Bldg. 4832 Whse 7
Lilly Dr.
Edwards, CA 93523

NASA TechBriefs

National Aeronautics and Space Administration

April 1997
97-04

5 Electronic Components and Circuits

13 Electronic Systems

21 Physical Sciences

33 Materials

37 Computer Programs

43 Mechanics

49 Machinery

55 Fabrication Technology

61 Mathematics and Information Sciences

67 Life Sciences

This document was prepared under the sponsorship of the National Aeronautics and Space Administration. Neither the United States Government nor any person acting on behalf of the United States Government assumes any liability resulting from the use of the information contained in this document, or warrants that such use will be free from privately owned rights.

BLANK PAGE

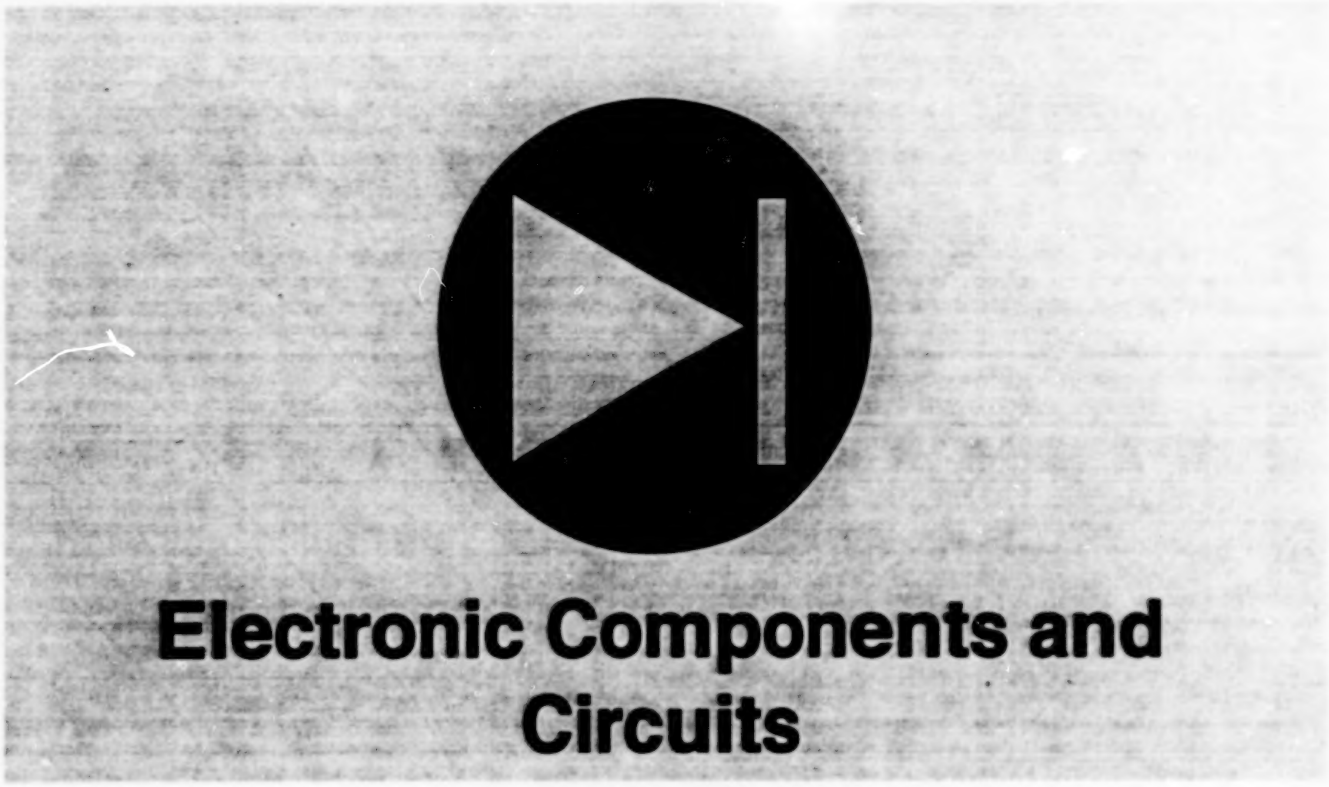

Electronic Components and Circuits

Hardware, Techniques, and Processes

7 Scheme for Single-Mode Pumping of a Solid-State Laser
8 Magnetic-Bubble Annihilator for Use in VBL Memories
9 Charge Amplifier/Discriminator With Wide Dynamic Range
10 Efficient, Fundamental-Transverse-Mode, Diode-Pumped Lasers
10 Laser-Diode-Source Module With Fiber-Optic Coupling
11 Ultra-Low-Resistance Metal Contacts on InP
11 Sinterless Formation of Contacts on Indium Phosphide: Part 2

BLANK PAGE

Scheme for Single-Mode Pumping of a Solid-State Laser

Best features of two older schemes would be combined.

Goddard Space Flight Center, Greenbelt, Maryland

A proposed scheme for side pumping of a solid-state laser rod efficiently in a single desired waveguide mode (the TEM_{00} mode) would combine the advantages of older end- and side-pumping schemes: It would afford efficiency approaching that previously attainable only through end pumping with focusing of the pump laser beam to a diameter of the order of tenths of a millimeter to match the desired mode; at the same time, it would afford the power scalability attainable only through side pumping by multiple laser diodes.

The scheme calls for side pumping by arrays of laser diodes that would be aligned so that the light would enter at angles favoring a high degree of absorption and conversion to laser light. The laser rod [which could be made of neodymium:yttrium aluminum garnet (Nd:YAG) or other suitable crystalline laser material] would be about 1 mm in diameter — unusually narrow for a laser rod but a convenient size for manufacture. This diameter would be only slightly wider than the region occupied by the major part of the electromagnetic energy in attainable laser modes; thus, in comparison with older side-pumping schemes involving wider laser rods, this scheme would cause a greater portion of the cross section of the laser rod to contribute to laser action and a lesser portion to merely convert the absorbed pump light to heat.

The laser head (see Figure 1) would include the laser rod and arrays of laser diodes mounted in a heat sink. The pump light would enter the laser rod from the two arrays of laser diodes through two longitudinal stripes, each 100 μm wide and located diametrically opposite the other. Each of these stripes would be antireflection (AR) coated for low reflection at the wavelength of the pump light (809 nm in the case of the laser diodes used to pump Nd:YAG). The remainder of the cylindrical surface of the rod would be coated for high reflection at the pump wavelength.

The sideways offset between the two arrays of laser diodes is an essential feature of the pump geometry, shown in more detail in Figure 2. With this geometry, pump light that entered the rod from the laser diodes would traverse the cross section several times, confined to the interior of the rod by reflection. Ray-trace calculations show that pump light would typically undergo three reflections before

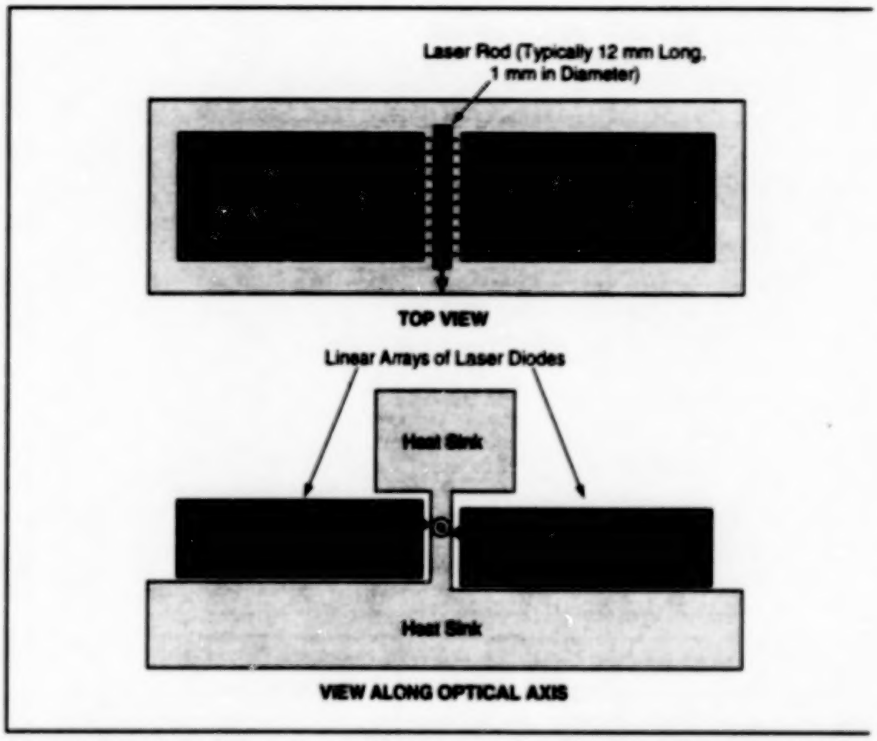
Laser Rod (Typically 12 mm Long, 1 mm in Diameter)
TOP VIEW
Linear Arrays of Laser Diodes
Heat Sink
Heat Sink
VIEW ALONG OPTICAL AXIS

Figure 1. Two Linear Arrays of Laser Diodes would pump the laser rod from opposite sides.

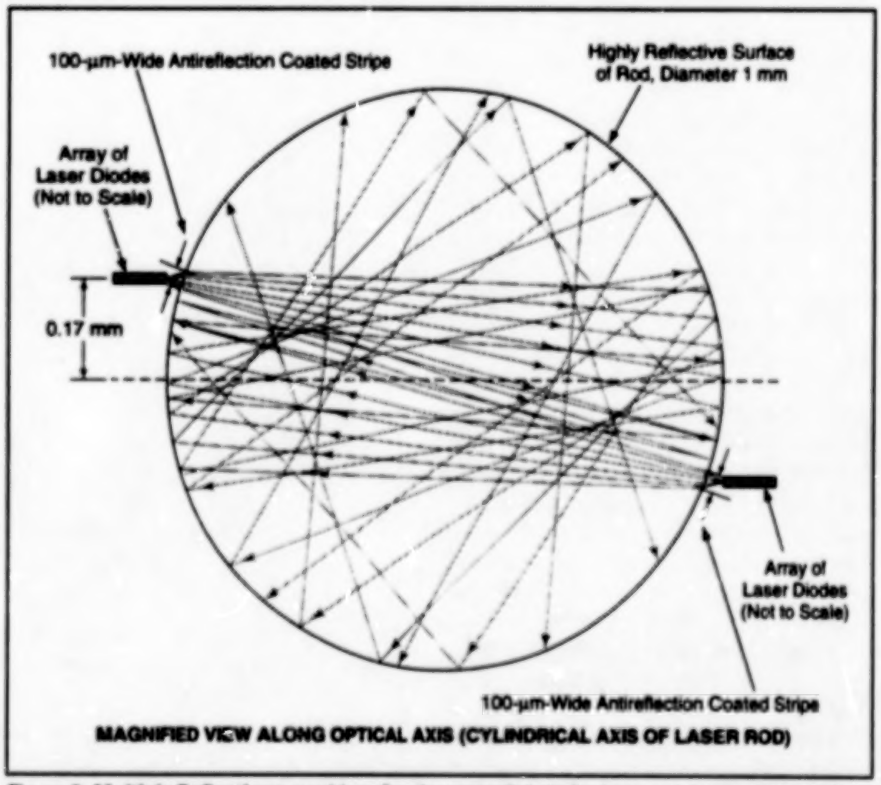
100-μm-Wide Antireflection Coated Stripe
Highly Reflective Surface of Rod, Diameter 1 mm
Array of Laser Diodes (Not to Scale)
0.17 mm
Array of Laser Diodes (Not to Scale)
100-μm-Wide Antireflection Coated Stripe
MAGNIFIED VIEW ALONG OPTICAL AXIS (CYLINDRICAL AXIS OF LASER ROD)

Figure 2. Multiple Reflections would confine the pump light in the laser rod, increasing the effective optical path length for pump light to about 4 times the diameter, thus increasing the utilization of the pump light.

escaping from the rod through one of the antireflection coated stripes. Thus, more than 90 percent of the pump would travel 4 mm before escaping through the AR stripes, in a rod of only 1 mm diameter, and most of the path would lie generally in the central region, where coupling to the desired laser mode would be greatest. A 4-mm path in Nd:YAG for a wavelength of 809 nm results in 84-percent absorption of the pump light in the laser medium.

This work was done by D. Barry Coyle of **Goddard Space Flight Center**. *Further information is contained in a TSP [see page 1].*
GSC-13636

Magnetic-Bubble Annihilator for Use in VBL Memories

Enlarged loop increases tolerance to misalignment of the magnetic bubble.

NASA's Jet Propulsion Laboratory, Pasadena, California

Vertical-Bloch-Line (VBL) memories are a new class of high-density magnetic-storage devices in which the information is represented by magnetic structures (VBLs) in the domain walls, rather than by the domains themselves as in magnetic-bubble memories. Writing and reading of VBLs in long stripe domains is achieved by interaction of the stripe heads with bubbles of input/output (I/O) lines. Because the VBLs are propagated along the stripe walls by an external field, the bubbles must be propagated by local fields, e.g., created by meandering current loops. Although this "current access" mode had long been proposed for bubble memories, details for bubble nucleation and annihilation by current loops had not been worked out. This article describes a substantial improvement of an earlier bubble annihilator for current access technology.

An improved design for a magnetic bubble annihilator in a magnetic memory device features an enlargement (relative to a previous design) of an electrically conductive loop. This enlargement increases the electrical current needed to annihilate a magnetic bubble, but also increases tolerance to misalignment of the bubble and increases tolerance to variation in the amplitude and duration of the annihilating current pulse.

In general, a magnetic memory device of the type in question (see figure) includes a magnetic garnet film with its "easy" direction of magnetization perpendicular to the surface. A magnetic bubble is a round cylindrical domain, wherein the direction of magnetization is opposite the direction of magnetization in the surrounding area of the garnet film. Magnetic bubbles are confined within a bubble track, which is a groove in the garnet film. A metal-film loop connected to metal-film strip conductors is laid across the bubble track for use in annihilating bubbles; this is the loop mentioned above. The device also includes a meandering strip of metal film laid along the track; this strip is part of a structure that propagates magnetic bubbles along the track.

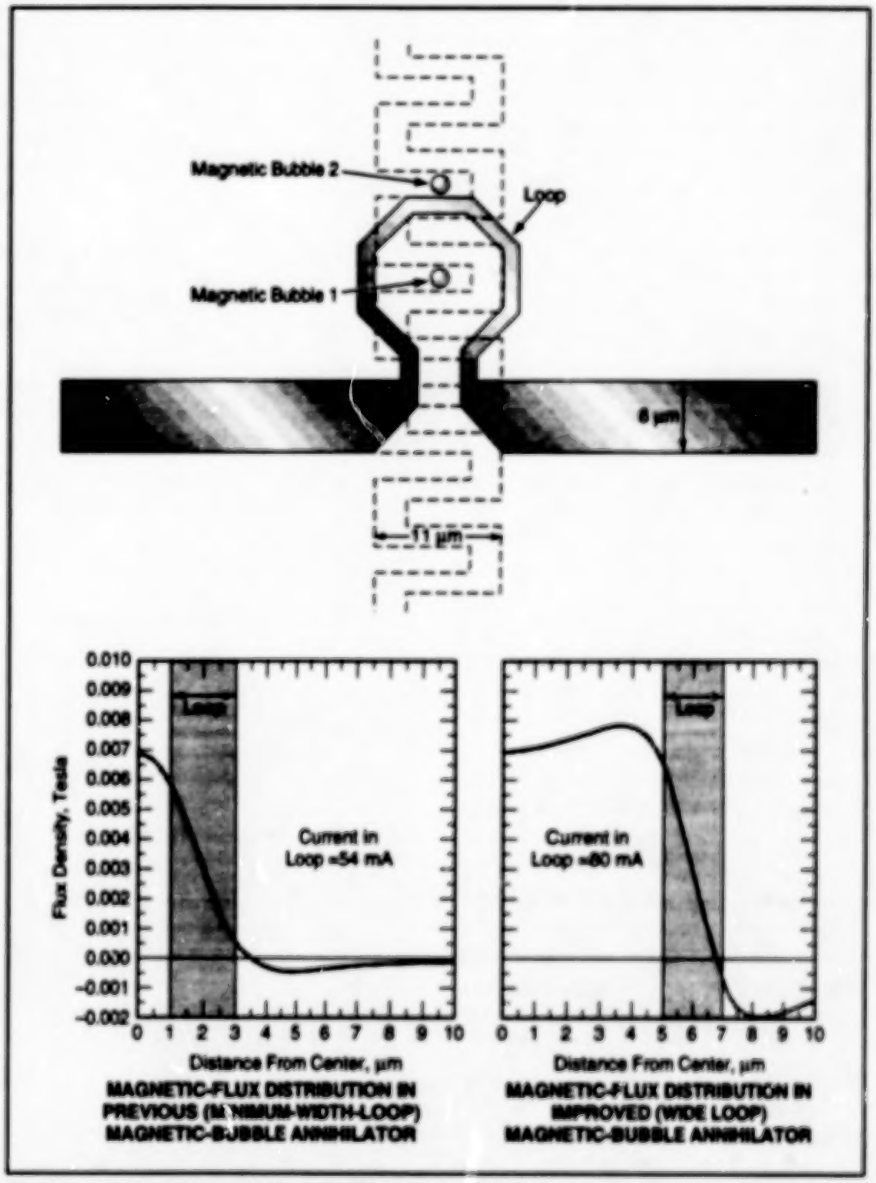

The Loop in the Improved Magnetic Bubble Annihilator is 5 times as wide as it was in the prior version; the resulting distribution of magnetic flux density is more favorable to retention of a magnetic bubble in the loop.

A loop of the previous design was made with an opening of minimum width in the hope of generating a strong local magnetic field that would reverse the magnetization of a bubble. The magnetic flux density produced by the pulse of current in the loop was maximum at the center of the loop. The current needed to annihilate a perfectly or nearly perfectly centered magnetic bubble was estimated to be about 44

mA. However, it was observed that when a bubble was not well centered in the loop, either the bubble was pushed away from the loop instead of annihilated, or else it was necessary to use a very large and very short current pulse to achieve annihilation.

In a loop of improved design with the wider opening, the magnetic flux density reaches a maximum at a distance of a few microns from the center, with a shallow local minimum at the center. This shallow local minimum in the magnetic field helps to hold the magnetic bubble in the loop when the average magnetic field is raised by increasing the current. This design is consistent with state-of-the-art track widths of 4 to 5 μm, bubble diameters of 2 to 3 μm, and bubble misalignments of the order of 1 μm. As long as the magnetic bubble lies entirely within the loop, it can be annihilated by a current of about 80 mA. The optimum size of the loop is determined in conjunction with the requirement that the next bubble in line not be pushed away by the magnetic field outside the loop.

This work was done by Udo Lieneweg, George N. Patterson, and David Opalsky of Caltech for **NASA's Jet Propulsion Laboratory**. *Further information is contained in a TSP [see page 1].*
NPO-19716

Charge Amplifier/Discriminator With Wide Dynamic Range

Output includes two logarithmic bar graphs.

NASA's Jet Propulsion Laboratory, Pasadena, California

The figure shows the major functional blocks and some of the circuitry of a charge amplifier/discriminator that accepts, as input, the output of any of a variety of electron, photon, and ion detectors operating in the pulse-counting mode at rates up to 500 kHz. This instrument generates a 20-segment logarithmic-bar-graph display of the threshold level and of each input pulse that exceeds a threshold charge-detection level. Calibrated charge-detection thresholds can be adjusted within the range of 8.8×10^{-15} to 3.2×10^{-10} Coulombs, (5.5×10^4 to 2×10^9 electrons); this amounts to a dynamic range of about 91 dB.

Each pulse of charge arriving at the input terminal is stored in the total input capacitance, $C_{total} = C_{test} + C_{in} +$ (when switched in) C_D. The durations of the pulses are much shorter than the characteristic times of the input circuitry and the following pulse-shaping circuitry, so that a given pulse can be regarded as an impulse of infinitesimal duration and total charge q; thus, the voltage across the total input capacitance immediately after the arrival of the pulse is $v_{in} = q/C_{total}$. For calibration (instead of discriminating unknown input charge q), pulses of calibrated charge $Q_{cal} = C_{test}V_{peak}$ are obtained from the negative transitions of a square wave of peak-to-peak voltage V_{peak} applied to the test input terminal.

The input voltage is fed to a pulse-shaping amplifier which produces a semisinusoidal (positive half) output voltage pulse proportional to the input charge, with full width at half maximum (FWHM) of 1 μs. The switch labeled "+10" can be closed to connect C_D to increase the input capacitance by a factor of 10, thus dividing the input voltage and extending the dynamic range of the instrument by this factor. To maintain the FWHM of 1 μs, shunt resistor R_D is switched in along with C_D. The pulse-shaping circuit is followed by an amplifier stage that can be set to a gain of either 1 or 10, thus enabling further extension of the dynamic range.

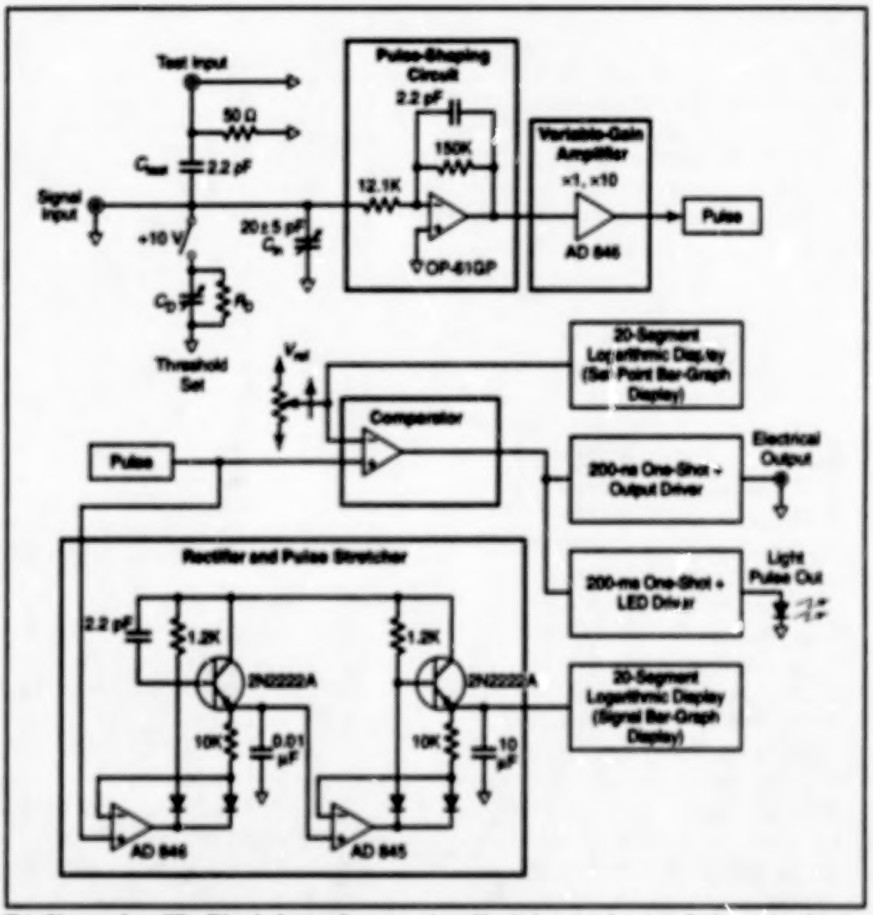

This Charge Amplifier/Discriminator features a logarithmic-bar-graph output display and a charge threshold that can be adjusted within a dynamic range of about 91 dB.

The novelty of the design lies in a high-speed, half-wave, peak-detector circuit (denoted "rectifier and pulse stretcher" in the figure) configured in two stages with time constants of 100 μs and 100 ms, respectively. The first stage must drive a 0.01-μF output capacitor to at least 10 V in 500 ns, requiring a maximum current of 200 mA. A pass transistor is added to supply this current. Biasing the transistor to class A with the various diodes improves the small-signal response by decreasing the dead band to approximately the bias voltage (which is of the order of 28 mV per stage (56 mV total) and depends on temperature. Both stages are underdamped such that their small-signal responses

include overshoots of approximately 20 mV. The overshoot voltage can be subtracted out, reducing the remaining offset error with input signal to 36 mV. Any real signal exceeding this limit is accurately displayed at the output. Inasmuch as an analog output signal is also available, an oscilloscope can be used to monitor signals at levels less than 36 mV, if necessary. The bar-graph output display is most accurate for inputs in the frequency range of 3 kHz to 200 kHz.

This work was done by Christopher J. Wrigley, Geoffrey K. James, and Brian O. Franklin of Caltech for **NASA's Jet Propulsion Laboratory**. *Further information is contained in a TSP [see page 1].*
NPO-19597

Efficient, Fundamental-Transverse-Mode, Diode-Pumped Lasers

Intra-cavity apertures are not necessary for operation in the fundamental transverse mode.

Goddard Space Flight Center, Greenbelt, Maryland

A class of efficient, rugged, solid-state lasers is based on a combination of (1) side pumping by diode lasers and (2) configuring the gain regions, in conjunction with the side pumping, so that the fundamental transverse electromagnetic mode (TEM_{00}) is automatically selected. The configuration overcomes the practical limitation on power available for longitudinal pumping by devices that were on the market when the information for this article was submitted. It also eliminates the need for the intra-cavity apertures that are used in older side-pumping configurations to ensure operation in the TEM_{00} mode. Typically, an intra-cavity aperture induces substantial loss in energy or power, and diffraction around the aperture can degrade the quality of the emitted laser beam.

The figure schematically illustrates a typical laser of this class. The pump beam is a thin sheet of light generated by a bar-shaped laser diode placed above and aligned parallel with the gain region of the laser crystal. The beam is collimated by a cylindrical microlens and aimed at the TEM_{00}-mode region of the laser crystal. Thus, the pump beam overlaps the TEM_{00}-mode region, which, as explained below, contains part of the gain region.

The lasers of this class exploit a modified version of the principle that if the gain region of the laser crystal is smaller than the region occupied by the TEM_{00} laser mode, then the selection of the TEM_{00} mode is assured. In the modified version that applies here, the gain region of the laser crystal is constrained in the following sense: The longitudinal (*z*-axis) dimensions of the gain region and the TEM_{00}-mode region in the laser crystal are the same, while the gain region of the laser crystal is narrower than the TEM_{00}-mode region in one of the lateral dimensions (the *x* axis in the figure).

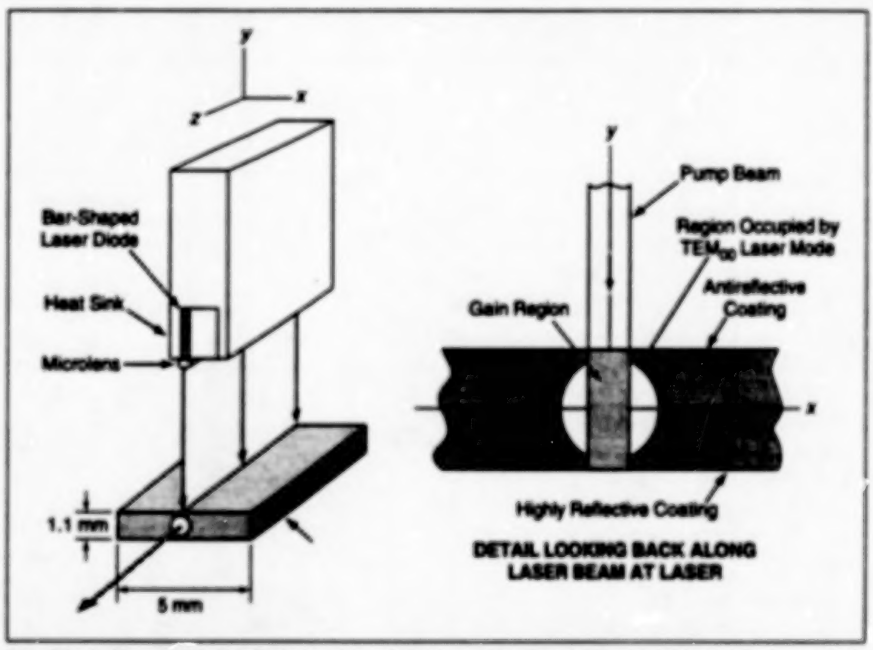

This Diode-Pumped Solid-State Laser exploits a combination of side pumping, a gain region that is narrower than the TEM_{00} mode in the *x* dimension, and reflection losses at the top and bottom surfaces of the laser crystal to suppress non-TEM_{00} modes in the *y* dimension.

Selection of the TEM_{00} mode in the other lateral dimension (the *y* axis in the figure) is accomplished by using the gain region as an aperture; that is, by exploiting the losses induced by the top and bottom of the laser crystal. To obtain optimum performance of the laser, it is necessary to balance the need for complete absorption of the pump beam (for which the crystal should be made deeper in the *y* dimension) against the need to use the top and bottom of the laser crystal as an aperture to strip off electromagnetic modes of higher order along the *y* axis.

This work was done by Robert Afzal and Mark Seker of **Goddard Space Flight Center**. *Further information is contained in a TSP [see page 1].*

This invention is owned by NASA, and a patent application has been filed. Inquiries concerning nonexclusive or exclusive license for its commercial development should be addressed to the Patent Counsel, Goddard Space Flight Center [see page 20]. Refer to GSC-13602.

Laser-Diode-Source Module With Fiber-Optic Coupling

A flexible design enables the use of alternative components and coupling schemes.

Marshall Space Flight Center, Alabama

A module of optoelectronic equipment has been developed to satisfy requirements to (1) couple light from a laser diode into a single-mode optical fiber and (2) send a portion of the light through a reference cell. The module incorporates the following components:

- A laser diode in a TO-type can;
- A thermoelectric cooler;

- A collimating lens;
- An optical isolator;
- A beam splitter for the reference and fiber beams;
- A commercial fiber collimator;
- A mount that holds the fiber collimator and that is adjustable in translation along, and rotation about, the two coordinate axes perpendicular to the nominal optical axis;
- A reference cell; and
- A reference detector.

The module features a flexible design that enables the use of different laser diodes and different reference cells and that provides the option for either fiber-optic or free-space coupling of the laser beam. The design also facilitates adjustments to maximize coupling of laser light into the fiber and minimizes both optical interference fringes and reflection of light back into the laser diode.

This work was done by Fritz Bien, Michael E. Gersh, Neil M. Goldstein, and Jamine Lee of Spectral Sciences, Inc., for **Marshall Space Flight Center**. *No further documentation is available.*

Inquiries concerning rights for the commercial use of this invention should be addressed to the Patent Counsel, Marshall Space Flight Center [see page 20]. Refer to MFS-26438.

Ultra-Low-Resistance Metal Contacts on InP

Metal contacts on InP semiconductor devices can be made to exhibit electrical resistivities close to the theoretical minimum value — of the order of 10^{-6} Ω·cm^2. Heretofore, the lowest contact resistivities were of the order of 10^{-7} Ω·cm^2; these were achieved by use of Ni and other metals and alloys as the contact materials. The present ultra-low-resistance contacts are formed by first depositing Au on the InP surfaces, then depositing Ni on the Au, then sintering. During sintering, Ni diffuses through the Au into the InP, but the Au retards the diffusion of In from the InP into the contacts. As a result, after sintering, the concentration of In at the interface between the semiconductor and the metal is greater than it is when Au is not used; the net effort of the higher concentration of In and the diffusion of nickel into the subcontact bulk material is to reduce the interfacial barrier height and thus the resistivity.

This work was done by Victor G. Weizer and Navid S. Fatemi of Sverdrup Technology, Inc., for **Lewis Research Center**. *Further information is contained in a TSP [see page 1].*

Inquiries concerning rights for the commercial use of this invention should be addressed to NASA Lewis Research Center, Commercial Technology Office, Attn: James Martz, Mail Stop 7-3, 21000 Brookpark Road, Cleveland, Ohio 44135. Refer to LEW-15816.

Sinterless Formation of Contacts on Indium Phosphide: Part 2

An alternative intermediate contact material can be used in the technique, described in "Sinterless Formation of Contacts on Indium Phosphide," *NASA Tech Briefs*, Vol. 19, No. 10 (October, 1995) page 45, for sinterless formation of low-resistivity (≈10^{-6} Ω·cm^2) electrical contacts on InP semiconductor devices without damaging the devices. The alternative material is Ni_3P. A layer of this material is deposited, between the InP and the metal contact layer, to the same thickness (40 Å) as that of the AgP_2 intermediate contact layer described in the prior noted article.

This work was done by Victor G. Weizer and Navid S. Fatemi of Sverdrup Technology Corp. for **Lewis Research Center**. *Further information is contained in a TSP [see page 1].*

Inquiries concerning rights for the commercial use of this invention should be addressed to NASA Lewis Research Center, Commercial Technology Office, Attn: James Martz, Mail Stop 7-3, 21000 Brookpark Road, Cleveland, Ohio 44135. Refer to LEW-15815.

BLANK PAGE

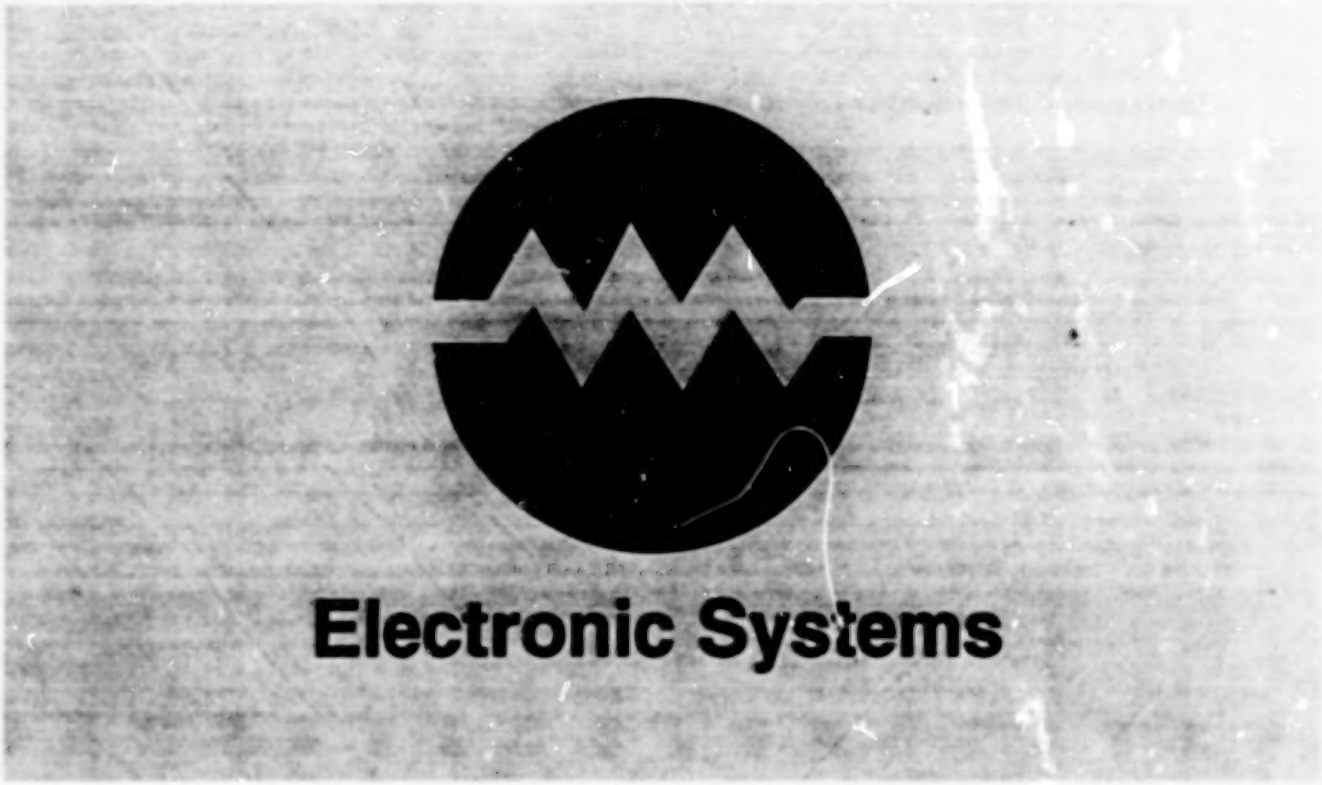

Electronic Systems

Hardware, Techniques, and Processes

15 Single-Camera Stereometric Laser Ranging System
16 Improved Video Sensor System for Guidance in Docking
17 Powering a Lightweight Airplane With Phased Microwave Beams
18 Radio Beacon Indicates Direction to Receiver
19 Analog/Digital Potential-Mapping System for Robotic Guidance

BLANK PAGE

Single-Camera Stereometric Laser Ranging System

Distances could be measured and computed quickly, with relatively simple equipment.

Lyndon B. Johnson Space Center, Houston, Texas

A proposed laser ranging system would provide measurements of distances to nearby objects in real time, with accuracy sufficient for many robotic, telerobotic, and teleoperation applications. In comparison with other ranging systems developed for the same purpose and based on various optical, radio, and acoustic measurement principles, this system would offer the advantage of relative simplicity of hardware and software. In particular, the data-processing aspects of this system would involve relatively simple algorithms that could be implemented with the requisite speed without having to resort to expensive high-speed computers.

Figure 1 illustrates the ranging system and ancillary equipment in a telerobotic scenario. The ranging system would include a low-power eye-safe laser (e.g., a 1-mW laser diode) mounted on a camera platform at a fixed baseline distance, b, to the side of a video camera. In the simplest example of alignment, the camera and the laser would be aimed along parallel lines. The video image would be projected to an operator through a helmet-mounted display system. The camera and laser would be positioned and aimed toward an object of interest by turning the camera platform under remote control, in imitation of movement of the operator's head as measured by position and orientation sensors in the helmet.

Ranging in this system would be based on stereometry (see Figure 2). That is, the distance to a point on the object of interest illuminated by the laser beam would be computed from a stereoscopic disparity. In this case, the stereoscopic disparity would be the distance x, on the focal plane of the video camera, between the central pixel (coinciding with the optical axis of the camera) and the image of the laser-illuminated spot on the object. Then from the basic geometric principle of stereometry, the distance, z, from the camera to the illuminated spot on the object would be approximated by $z = fb/x$, where f is the focal length of the camera.

The sequence of functions in ranging would be as follows: First, a frame grabber would acquire an image of the object without laser illumination and send the image data to a computer. Shortly thereafter, the laser would be turned on and the frame grabber would acquire an image of the object, including the laser-illuminated spot and send the image data to the computer. The computer would effectively subtract the first image from the second image to obtain a difference image that would contain only the laser-illuminated spot on the object. The computer would then calculate the centroid of the laser-illuminated spot. Then setting x equal to the distance between this centroid and the pixel on the optical axis (at the center of the image frame), the computer would calculate z from the equation shown above.

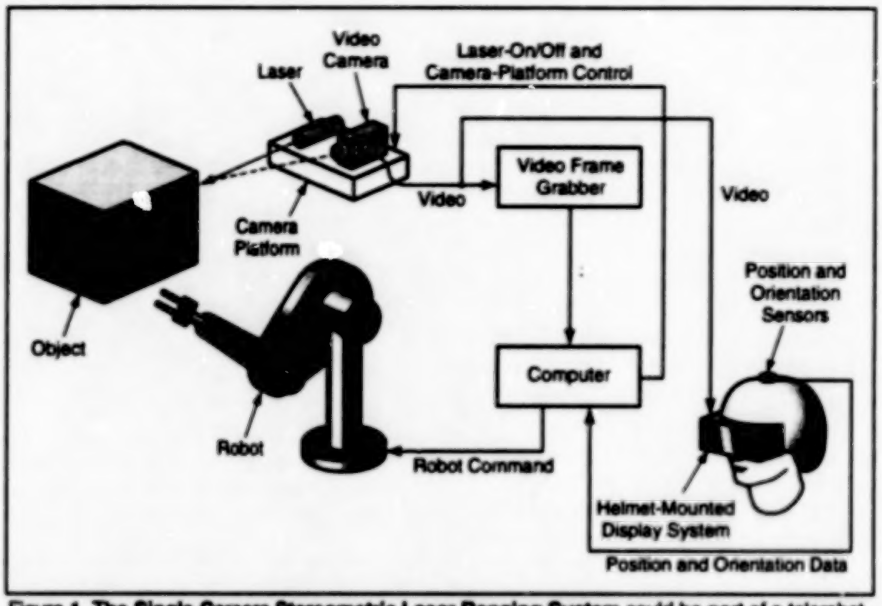

Figure 1. The Single-Camera Stereometric Laser Ranging System could be part of a telerobotic system. The ranging system would measure distances to nearby objects along the optical axis of the camera. The measurements would provide guidance for controlling the robot.

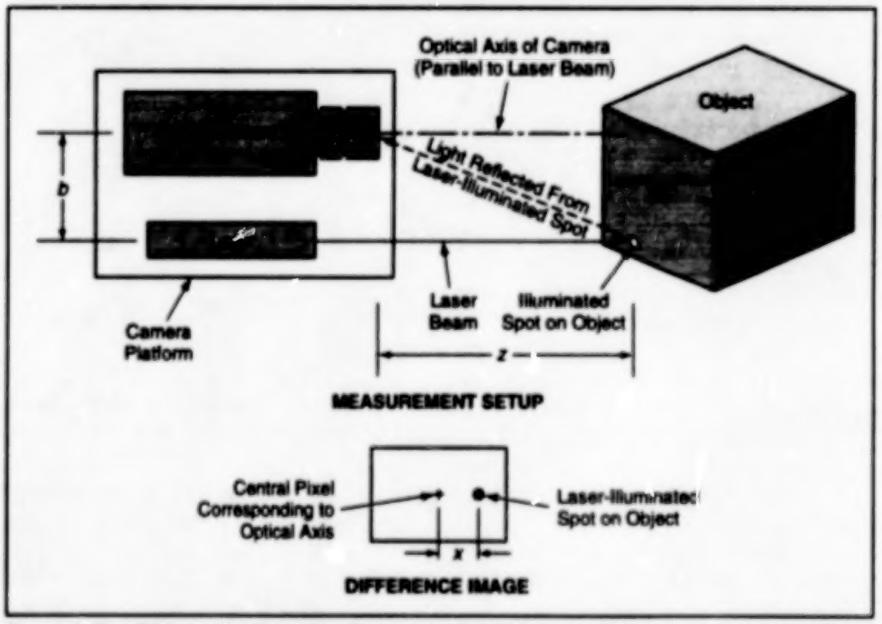

Figure 2. The Distance (z) From the Camera to the Object would be measured by a straightforward stereometric technique.

This work was done by Larry Li and Dennis L. Wells of **Johnson Space Center** *and Brian Cox of Lockheed Engineering and Sciences Co. Further information is contained in a TSP [see page 1].*

This invention is owned by NASA, and a patent application has been filed. Inquiries concerning nonexclusive or exclusive license for its commercial development should be addressed to the Patent Counsel, Johnson Space Center [see page 1]. Refer to MSC-22549.

Improved Video Sensor System for Guidance in Docking

The principal advantage over a prior system would be greater speed.

Marshall Space Flight Center, Alabama

A proposed video sensor system to be mounted on a tracking vehicle would automatically determine the relative orientation of a tracked vehicle during approach. The proposed system is intended to replace a current video sensor system that functions similarly and is used to guide the approach, which ends in the docking of the two vehicles with each other. The principal advantage of the proposed system would be greater speed.

A description of the current system is prerequisite to understanding the proposed system. The current system (see Figure 1) includes a video camera and two pulsed lasers of different wavelengths on the tracking vehicle. Three reflective targets are mounted at the corners of a triangle on one surface of the tracked vehicle, and a fourth reflective target is mounted at the tip of a stalk that protrudes from the surface. The reflective targets are covered by filters that absorb light at one of the laser wavelengths.

At the beginning of an operating cycle, the tracked vehicle is illuminated by a pulse of light from one of the lasers, and a frame grabber captures the resulting video image of the targets. Next, the other laser emits a pulse of light and the frame grabber captures the resulting video images. The two images are digitized and subtracted from each other in a fast computer, leaving only a digitized image of the targets. The orientation of the tracked vehicle relative to the tracking vehicle is then computed from the known geometric relationships among the positions of the targets in the image, the positions of the targets relative to each other, and the orientation of the video camera. A large fraction of time of each operating cycle is taken by the image-subtraction process; this limits the frequency with which orientation data can be updated and makes the system vulnerable to losing track of rapidly moving targets.

The proposed system would be based on similar principles but would implement them in a different way to reduce the time taken by the image-subtraction process. The camera in the proposed system (see Figure 2) would incorporate a prism assembly, wherein the beam of light focussed by the camera lens would be split to form images on two charge-coupled-device (CCD) imaging arrays. An absorptive filter would be placed in front of one CCD array. The analog output from the CCD array with the filter in front of it would be amplified by a factor of 2, and the analog output of the other CCD array would be subtracted from it. The analog output of the subtraction circuit would contain only the images of the targets because the subtraction would remove the background image. The analog output of the subtraction circuit would be fed to a frame grabber for digitization. The digitized image would then be processed to calculate orientation as in the current system.

The image-acquisition process takes about 30 ms, and the digital subtraction process takes about 250 ms for a 1,024 × 1,024 array on a 40-MHz digital signal processor. In comparison, the analog subtraction process takes negligible time. Thus, depending on the time taken by the orientation-calculation process, the proposed system might offer a considerable speedup over the current system. Another advantage of the proposed system is that unlike the current system, there would be no possibility of jitter between the subtracted images, because in the proposed system, the two subtracted images would be formed simultaneously.

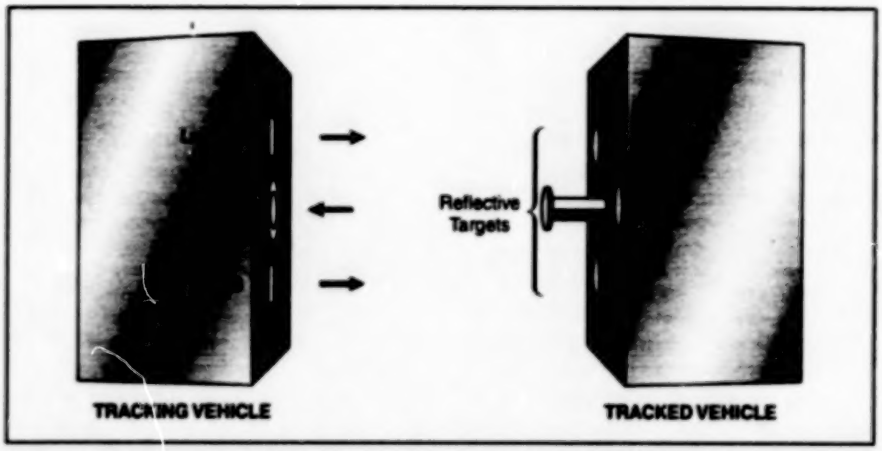

Figure 1. Video Images of Reflective Targets are acquired under illumination by two different lasers, digitized, subtracted from each other, and processed to determine the orientation of the tracked vehicle relative to the tracking vehicle.

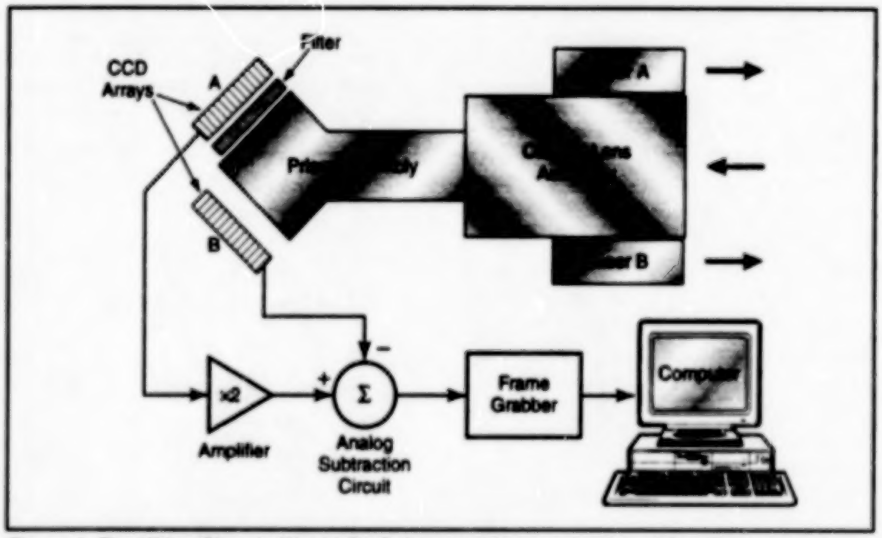

Figure 2. The Video Signals Would Be Subtracted from each other while still in analog form; this would take much less time than does subtraction of digital image data.

This work was done by Tom Sutherland of **Marshall Space Flight Center**. *Further information is contained in a TSP [see page 1].*

Inquiries concerning rights for the commercial use of this invention should be addressed to the Patent Counsel, Marshall Space Flight Center [see page 1]. Refer to MFS-31150.

Powering a Lightweight Airplane With Phased Microwave Beams

A radio beacon aboard the airplane would transmit signals for aiming and phasing.

NASA's Jet Propulsion Laboratory, Pasadena, California

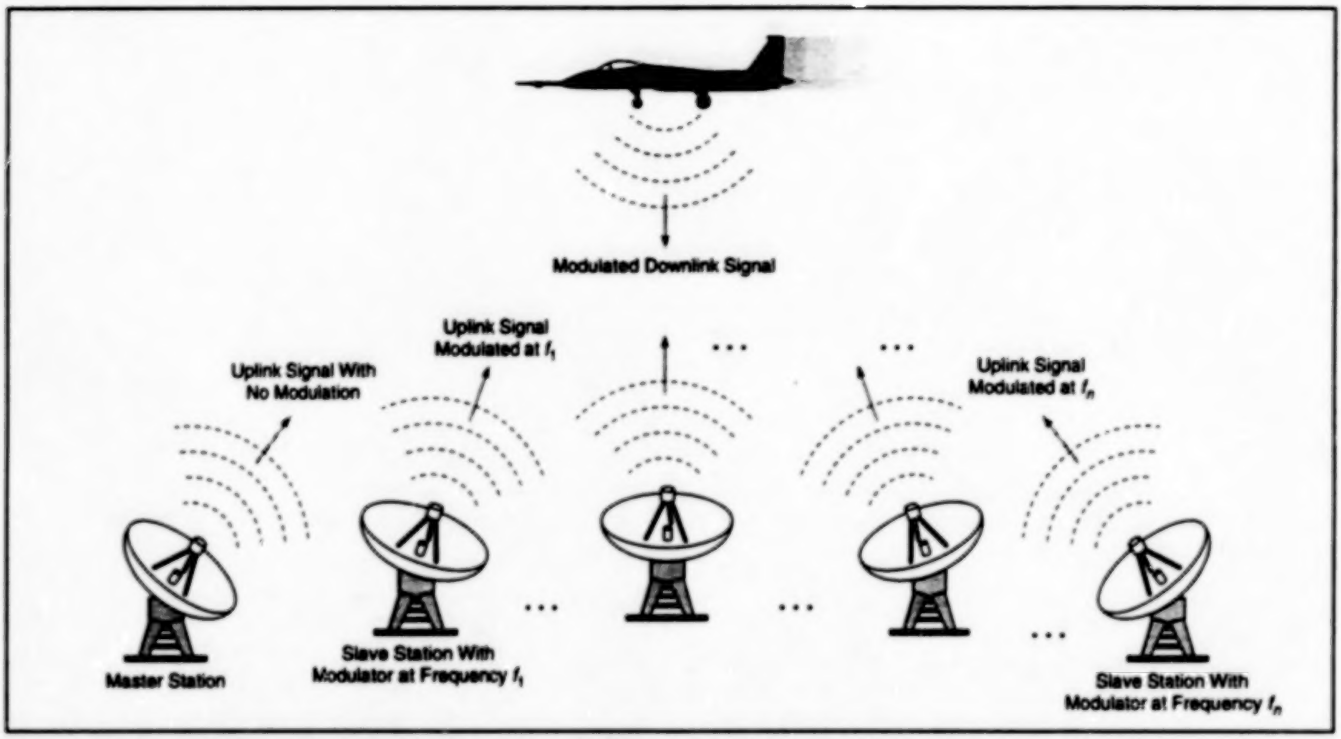
Modulated Downlink Signal
Uplink Signal Modulated at f_1
Uplink Signal With No Modulation
Uplink Signal Modulated at f_n
Master Station
Slave Station With Modulator at Frequency f_1
Slave Station With Modulator at Frequency f_n

Figure 1. The Downlink Transmitter in the Airplane would provide phase information for adjusting the relative phases of the uplink transmitters, plus a beacon signal for monopulse tracking.

Figures 1 and 2 illustrate aspects of a proposed system for microwave beaming of power from multiple phased microwave antennas at ground stations to a lightweight airplane flying in the vicinity. The system would operate independently of any other telemetry links between the airplane and ground, would contain a minimal number of components, and could be expanded by adding ground stations.

All of the ground stations would transmit high-power microwave uplink signals at the same carrier frequency, at controlled phases with respect to each other. One power signal would not be modulated, while each of the others would be phase-modulated at a unique frequency. A rectenna on the airplane would convert several uplink signals to dc to power the plane. The amplitude of the resulting dc will contain a ripple component at each of the unique uplink modulation frequencies, which is proportional to the phase error of the signal with that modulation frequency. The airplane would carry a low-power microwave downlink transmitter operating at a higher carrier frequency. The downlink signal would serve as a beacon for aiming the ground-station antennas. (Optionally, some antennas could be aimed in preparation, without turning on their high-power transmitters until needed or until the airplane was close enough.)

The downlink signal would also be modulated with the amplitude ripples from the rectenna. These ripples contain sufficient information to serve as feedback for adjusting the phases of the uplink signals at the ground stations so that the uplink signals would be made to arrive at the rectenna in phase with each other to maximize the power delivered to the rectenna.

The ground station transmitting the unmodulated uplink signal would be denoted the master; the other ground stations would be denoted slaves, and the phases of their uplink signals would be adjusted relative to that of the master, as described below. The rectenna would receive a composite of master and slave signals. A sample of the modulation in the composite signal would be extracted via low-pass filter 2 and used to modulate the downlink signal. The modulated downlink signal would thus contain information on the relative phase of each slave transmitter.

The uplink carrier frequency would be provided to each slave station through a common radio-frequency distribution subsystem. In each slave station, the distributed common carrier signal would be phase-modulated at its unique frequency, then passed to a high-power amplifier via a phase shifter, which would adjust the phase in response to the feedback phase-control signal. The high-power output signal would be bounced off a dichroic reflector, which would reflect at the uplink carrier and thereby direct this signal along the uplink path.

The dichroic reflector would be transparent at the downlink carrier frequency, and would thus allow the simultaneously received downlink signal to pass through the dichroic reflector into a monopulse receiving feed. Error and sum signals would be generated, filtered, and used to point the antenna to higher accuracy. In addition, a sample of the sum signal would be demodulated in a phase-locked loop, and the unique frequency of the modulation component from this particular slave would be separated from those of the other slaves; the modulation from this slave would be extracted from the composite modulation by use of a bandpass filter. The conditioned output of the phase-locked loop would serve as a control signal for adjusting the phase shifter.

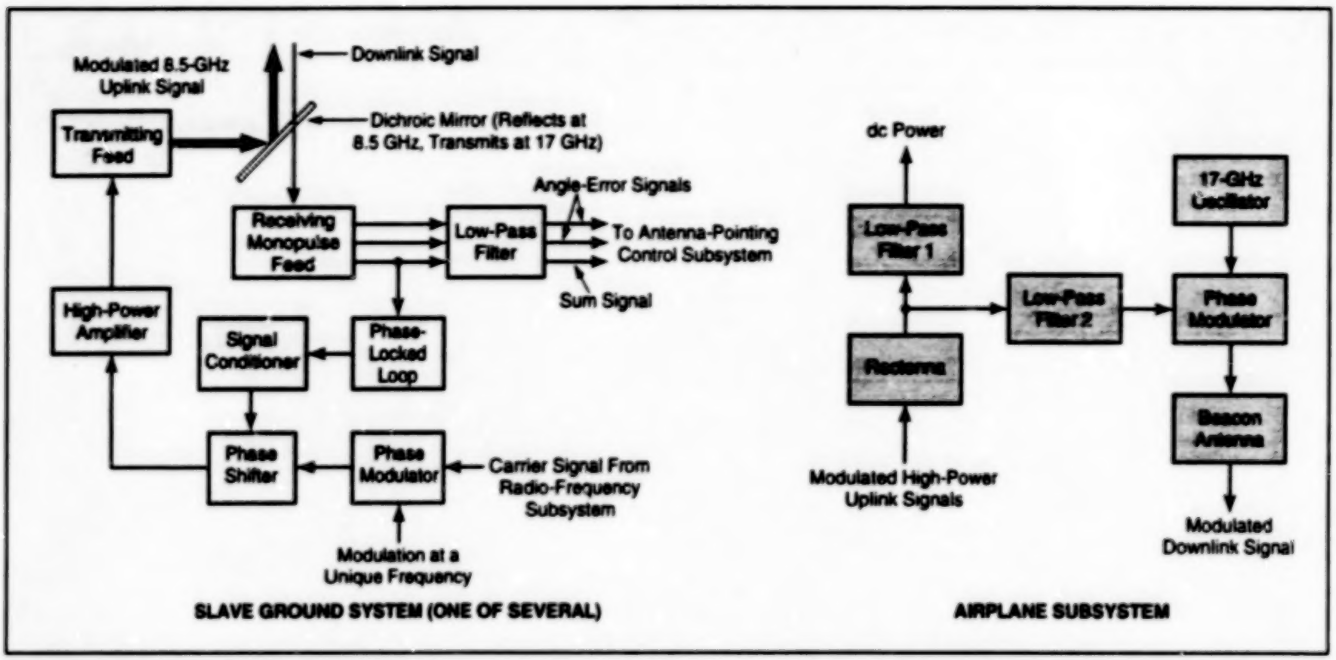

Figure 2. Airplane and Ground-Station Subsystems would cooperate as parts of an aiming and phase-controlling system to maximize the uplink power delivered to the rectenna.

This work was done by Bruce L. Conroy and Daniel J. Hoppe of Caltech for **NASA's Jet Propulsion Laboratory**. *Further information is contained in a TSP [see page 1].*

In accordance with Public Law 96-517, the contractor has elected to retain title to this invention. Inquiries concerning rights for its commercial use should be addressed to

Larry Gilbert, Director
Technology Transfer
California Institute of Technology
Mail Code 315 - 6
Pasadena, CA 91125
(818) 395-3288

Refer to NPO-19647, volume and number of this NASA Tech Briefs *issue, and the page number.*

Radio Beacon Indicates Direction to Receiver

The receiver need not be equipped with a directional antenna.

Marshall Space Flight Center, Alabama

A radio-beacon system provides information on the direction of a receiver relative to a transmitter, without need to equip the receiver with a directional antenna. The major advantage of this system is that by eliminating the need for a directional antenna, it also eliminates the need for antenna-steering mechanisms and circuitry, which can be expensive. In a typical application, the transmitter and receiver would be mounted in two different vehicles, and the operator of the receiving vehicle would use the directional information along with other information to prevent a collision with the transmitting vehicle.

The basic idea is to transmit a radio signal with amplitude that varies with time and direction according to prescribed waveforms that the receiver can recognize. The directional information is encoded in a repeating sequence of direction-dependent amplitude steps, which are generated in the following way: The amplified continuous-wave signal from an oscillator is fed through vector modulators to vertically oriented antenna elements mounted over a horizontal ground plane (see figure). Modulation waveforms that produce amplitude and phase modulation are applied to each vector modulator; these waveforms are designed to provide the required amplitude steps and the required variation in the antenna radiation pattern with time, the net result being that the amplitude steps of the signal radiated in a given direction differ from the amplitude steps of the signal radiated in a different direction.

The sequence can comprise any number of different amplitude steps and radiation patterns; the optimum number depends on the design of the antenna and the required performance of the system. The receiver includes a digital processor and a memory that contains digital representations of the prescribed waveforms that correspond to a set of directions. In the processor, a digital representation of the amplitude-vs.-time waveform of the received signal is compared with each prescribed waveform. The direction from the transmitter to the receiver is then assumed to be the direction associated with whichever prescribed waveform most closely matches the received waveform. It should also be possible to modulate the transmitted signal to convey information on the heading or orientation of the transmitting vehicle; in that case, the absolute direction from the transmitter to the receiver would also be known.

This work was done by James W. Harper of Science Applications International Corp. for **Marshall Space Flight Center**. *Further information is contained in a TSP [see page 1].*

MFS-31083

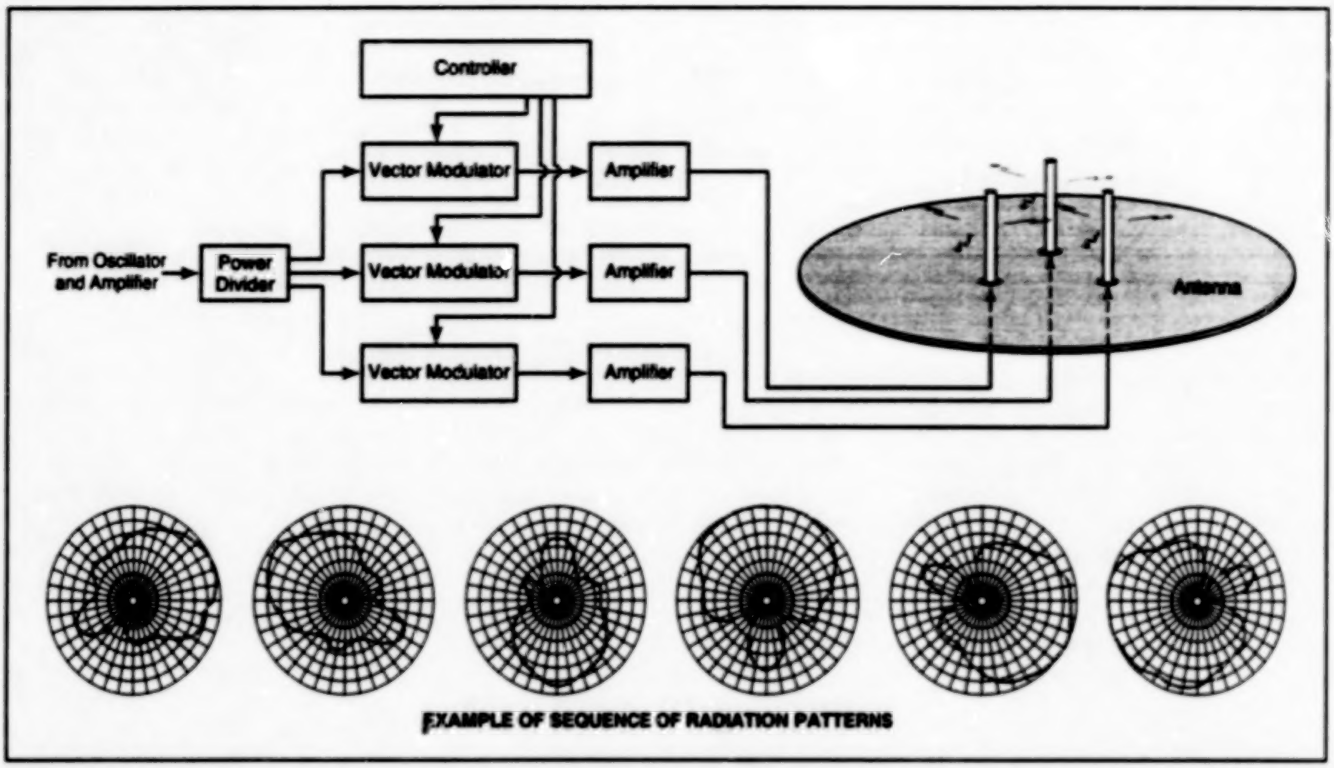

A Phased-Array Antenna is excited through vector modulators to radiate a signal with stepped amplitude and a radiation pattern (in the horizontal plane) that varies with time. The prototype system contains three antenna elements, but other numbers of elements could be used.

Analog/Digital Potential-Mapping System for Robotic Guidance

A potential field around obstacles and a goal is simulated.

Ames Research Center, Moffett Field, California

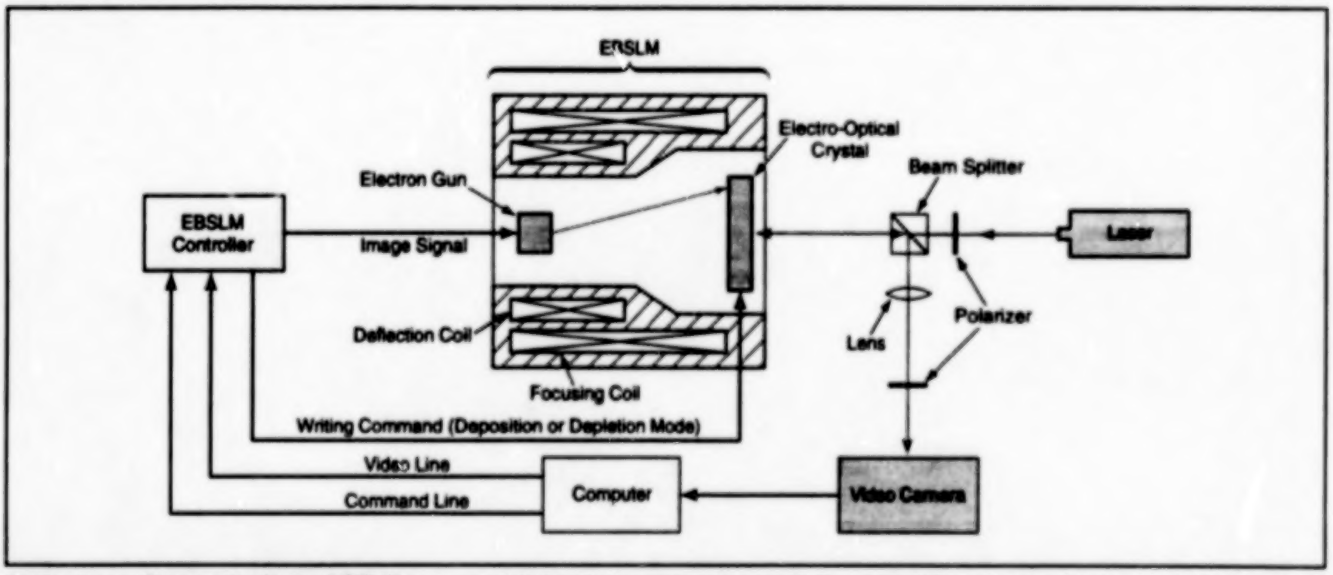

Analog Image Processing in the EBSLM and associated optical components speeds the computation of a simulated potential field in which a robot is repelled by obstacles and attracted by a goal, with an all-"downhill" path from any robot location to the goal.

An analog/digital electronic system generates an image that represents a simulated two-dimensional potential field for use in planning the trajectory of a robot across a floor or platform where there are obstacles (e.g., machines and people) that the robot must avoid on its way to a goal. As in other implementations of the potential-field method of robotic guidance, (1) the simulated potential field resembles an electrostatic field, (2) the potential between the robot and the obstacles is repulsive (as between objects of like electric charge), while the potential between the robot and the goal is attractive (as between objects of opposite electric charge), and (3) one seeks to compute a trajectory along the gradient of the potential field from any position to the goal. In typical other implementations of the potential-field method, the potential fields sometimes include local

minima wherein robots can become trapped. One advantage of the present system is that it simulates a potential field without any minima other than that of the goal; in effect, the system is designed to guarantee an all-"downhill" obstacle-avoiding path from any location to the goal.

The system generates a gray-scale video image, in which increasing brightness in a given pixel represents increasing repulsive local potential. Starting with bright areas for the obstacles and a dark spot for the goal, the image is generated in an iterative feedback process in which the attractive potential field propagates outward from the goal spot and surrounds all obstacles, filling the scene. A potential field generated in this way has a single minimum at the goal, as desired, but the field computation could take excessive time if performed by digital means only. In this system, the inherent speed of optical analog means is harnessed to reduce the field-computation time.

The figure schematically illustrates one version of the system. Under digital control by a computer, the analog image is written by use of a modulated electron beam that is scanned across the back (left) surface of an electro-optical crystal in an electron-beam-addressed spatial light modulator (EBSLM). At a given time, the computer commands the EBSLM to operate in either an electron-deposition or an electron-depletion mode. In the electron-deposition mode, the electro-optical crystal is biased at a high voltage and charge accumulates on the back surface of the crystal in the places exposed to the electron beam. In the electron-depletion mode, the electro-optical crystal is biased at a low voltage and there is net depletion of charge from places exposed to the electron beam. In either mode, the charge pattern that remains after electron-beam writing gives rise to an electric field that alters the index of refraction of the crystal in a corresponding pattern.

There is an important difference between the two modes: patterns written in the electron-depletion mode have sharp edges and remain within their original boundaries, whereas patterns written in the electron-deposition mode expand beyond their original boundaries (because of secondary emission of electrons from the surface of the crystal). Initially, the dark goal spot is written in electron-deposition mode and begins to expand. Then the bright obstacle patches are written in electron-depletion mode. The resulting image is digitized and sent to the computer for processing into a feedback pattern, which is then written in the electron-deposition mode to enhance the expansion of the dark goal spot. This sequence of operations is repeated to obtain further enhancement and expansion of the dark spot. During each cycle of the iteration, the computer compares the image with the image from the preceding cycle. When the difference between the two images is less than some small amount related to the noise level, the iteration is terminated and the average of the images is used to compute the potential field.

This work was done by Max B. Reid of **Ames Research Center**. *Further information is contained in a TSP [see page 1].*

This invention has been patented by NASA (U.S. Patent No. 5,483,168). Inquiries concerning nonexclusive or exclusive license for its commercial development should be addressed to the Patent Counsel, Ames Research Center [see page 1]. Refer to ARC-11997.

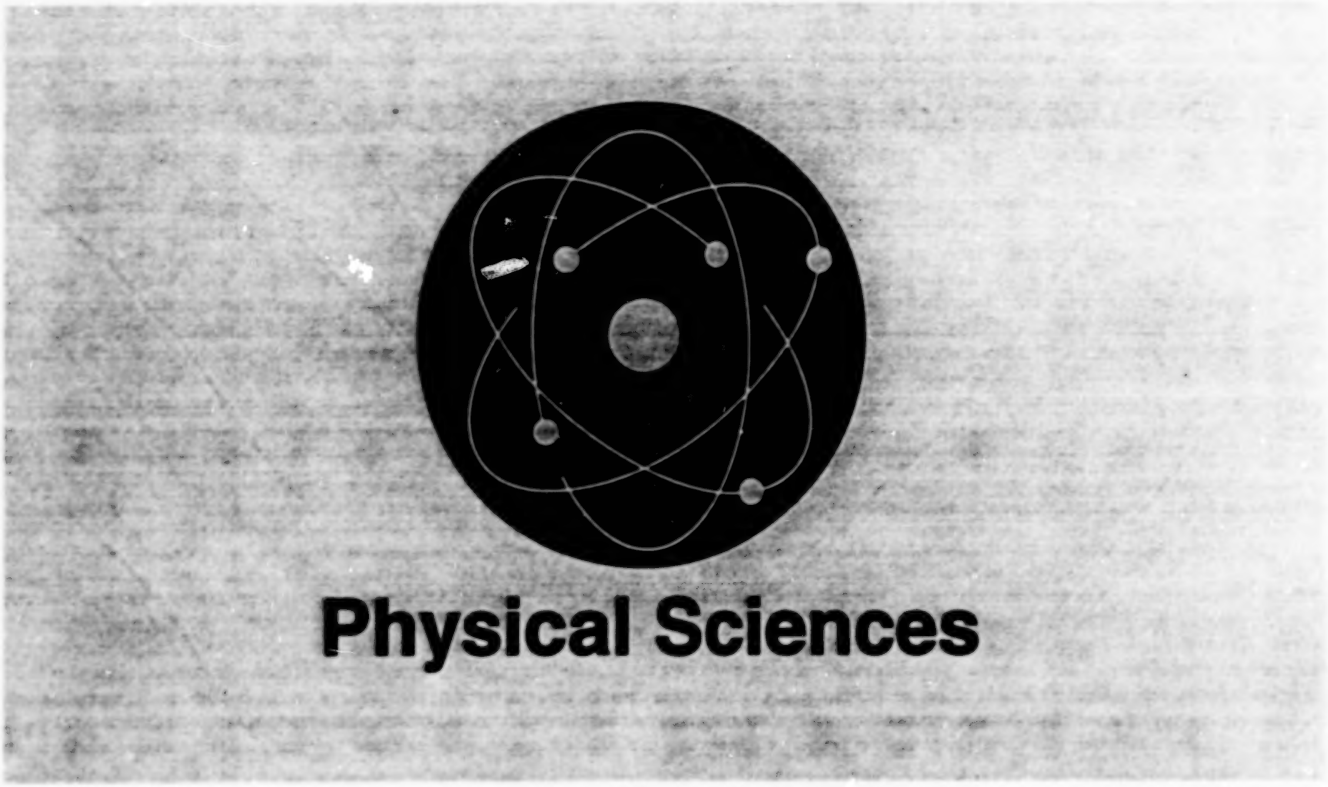

Physical Sciences

Hardware, Techniques, and Processes

23 Enhancing the Ultrasonic C-Scan of a Second Interface
24 Variable-Buoyancy Balloons for Tracking Tropical Storms
24 Kinematic Positioning With GPS Pseudorange and Carrier Phase
25 The γ-μ Method of Designing Achromatic Lenses
26 Evaluating Effects of Weather on Optical Communications
27 Apparatus for Advanced Ultrasonic C-Scan Imaging
28 Ultrasonic Instrument Produces Thickness-Independent Velocity Images
29 Optically Implementing an Algorithm for Representing Images

BLANK PAGE

Enhancing the Ultrasonic C-Scan of a Second Interface

A signal-processing algorithm corrects for the effect of the first interface.

Goddard Space Flight Center, Greenbelt, Maryland

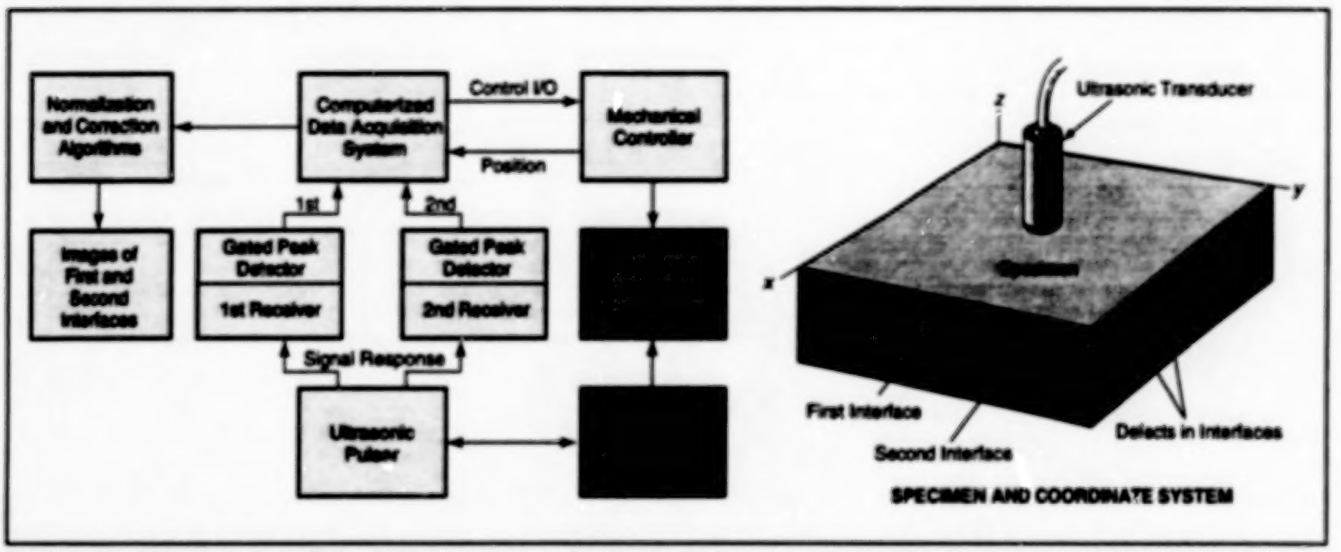

Figure 1. This Ultrasonic Pulse/Echo System produces a C-scan of a laminated specimen. When the specimen contains two interfaces, it produces independent C-scans of the first and second interfaces.

Figure 1 illustrates schematically an ultrasonic pulse/echo inspection system that yields C-scan images of flaws in two interfaces at different depths in a laminated specimen. The system corrects for the effect of flaws in the first interface, which could otherwise mask or distort the image of flaws in the second interface.

The masking or distortion arises because a flaw in the first interface alters the probing ultrasonic signal on its way to the second interface. Thus, if a flaw in the second interface lies behind (that is, at the same x,y position as that of) a flaw in the first interface, then this second flaw is insonified by the altered probing ultrasonic signal, and the resulting ultrasonic image is altered accordingly.

The present system processes the ultrasonic signals to separate the ultrasonic echoes from the two interfaces and applies a correction algorithm, which is based on the following two equations derived from the fundamental equations of transmission and reflection of ultrasonic pulses:

$$A_f(x, y) = C_1 R_{12}(x, y) \text{ and}$$

$$A_g(x, y) = C_2 R_{23}(x, y) - C_3 A_f^2(x, y) R_{23}(x, y);$$

where $A_f(x,y)$ and $A_g(x,y)$ denote the position-dependent amplitudes of the ultrasonic signals returned from the first and second interfaces, respectively; $R_{12}(x,y)$ and $R_{23}(x,y)$ denote the position-dependent ultrasonic reflection coefficients of the first and second interfaces, respectively; and C_1, C_2, and C_3 are constants. $A_f(x,y)$ and $A_g(x,y)$ are measured ultrasonic parameters. $R_{12}(x,y)$ and $R_{23}(x,y)$ are the interface properties that one seeks. C_1, C_2, and C_3 are derived from combined transmission coefficients, attenuation coefficients, thicknesses, and other material parameters.

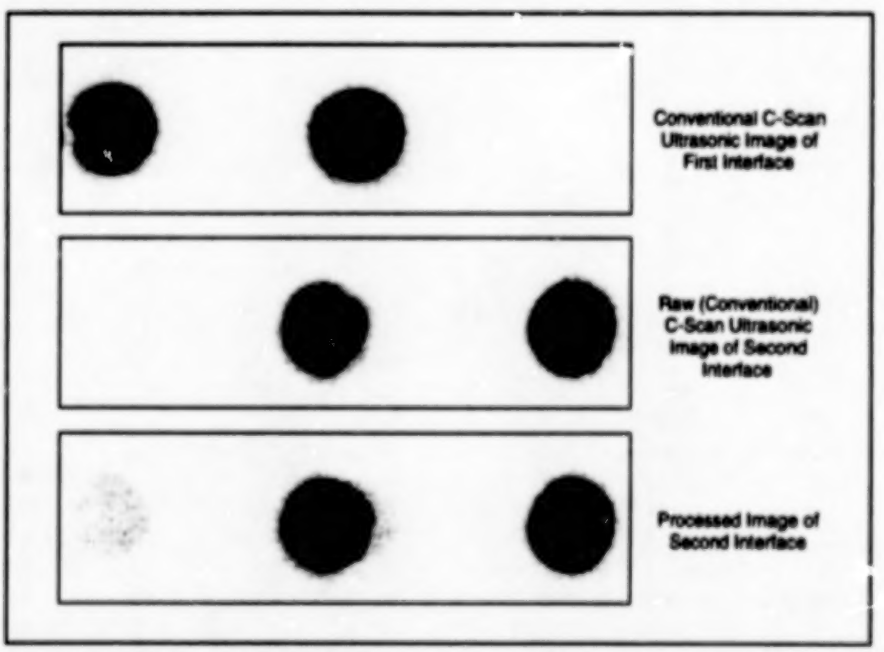
Conventional C-Scan Ultrasonic Image of First Interface
Raw (Conventional) C-Scan Ultrasonic Image of Second Interface
Processed Image of Second Interface

Figure 2. Processing of the Raw Scan from the second interface of a demonstration specimen illustrates the ability of the correction algorithm to filter out the effect of an overlying defect in the first interface.

The system gates the ultrasonic return signals by round-trip travel times to separate the returns from the first and second interfaces, then peak-detects the gated returns to measure the amplitudes $A_f(x,y)$ and $A_g(x,y)$. The correction algorithm then computes normalized versions of these amplitudes and, in the case of $A_g(x,y)$, applies a correction in the form of an approximation

$$A_g'(x, y) = A_f^2(x, y) A_g(x, y)$$

Thus, the output of the system is a normalized amplitude proportional to $R_{12}(x,y)$

and a normalized, corrected amplitude approximately proportional to $R_{23}(x,y)$.

In an experiment to demonstrate feasibility, the system was used to scan a specimen that contained two defects in the first interface and two defects in the second interface, positioned so that one of the defects in the first interface partly shadowed a defect in the second interface. As shown in Figure 2, processing in the system by use of the correction algorithm recovered the shadowed portion of the image of the second interface.

This work was done by E. James Chem of **Goddard Space Flight Center**. *Further information is contained in a TSP [see page 1].*
GSC-13792

Variable-Buoyancy Balloons for Tracking Tropical Storms

Evaporation and condensation of a secondary buoyancy fluid helps maintain approximately constant altitude.

NASA's Jet Propulsion Laboratory, Pasadena, California

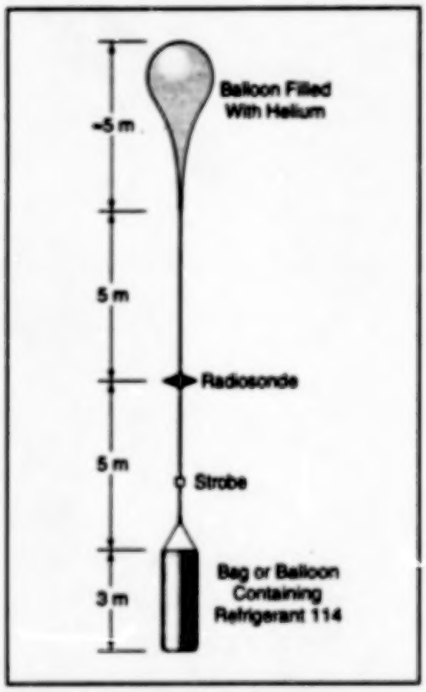

Figure 1. A Dual-Balloon System carries a radiosonde and strobe.

Radiosonde-balloon systems for tracking tropical storms at approximately constant altitudes over both land and sea are undergoing development. Customarily, a radiosonde balloon, which is attached to a floating ocean buoy, is launched into a tropical storm and is quickly drawn into the eye of the storm, even if it is launched hundreds of miles away. The balloon, however, are destroyed when the storm eye passes over land. It would be highly desirable for a balloon system to track the eye and maximum hurricane winds over both land and sea from some altitude(s) in the troposphere.

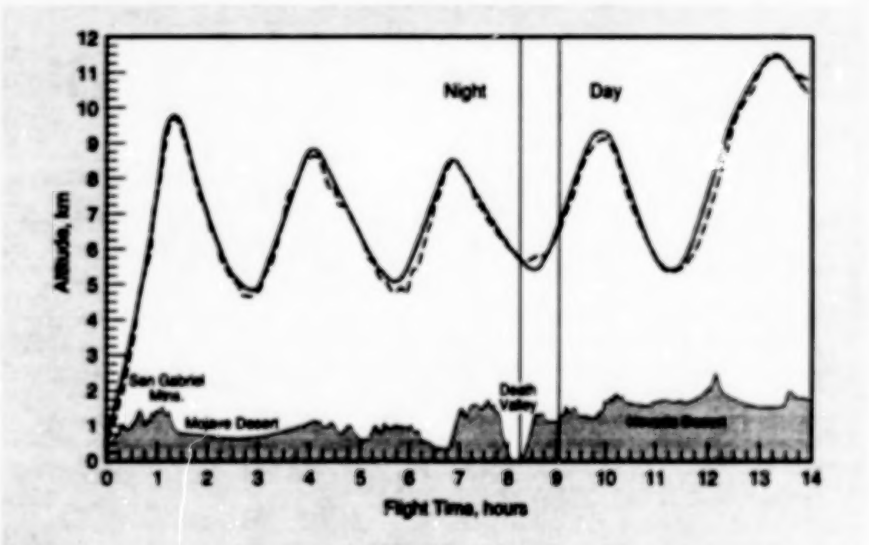

Figure 2. The Altitude of a Balloon System like that of Figure 1 was tracked until radio contact was lost over the Nevada Desert.

A balloon system of the type undergoing development contains a primary buoyancy fluid and a secondary buoyancy fluid. The buoyancy fluids are contained in separate balloons (see Figure 1). The primary buoyancy fluid is typically helium, while the secondary buoyancy fluid is a phase-change fluid [(for example, butane, ethyl chloride, or refrigerant 114 (dichlorotetrafluoroethane)]. The type and amount of secondary buoyancy fluid is chosen so that under the prevailing conditions of temperature and pressure, this fluid condenses above the desired altitude and evaporates below the desired altitude, causing the balloon to bob around the desired altitude.

The feasibility of this bobbing altitude concept was demonstrated in clear weather in an experiment with a two-balloon system like that of Figure 1. The system was released over California and went through several cycles of bobbing about an altitude of about seven kilometers (see Figure 2). In an actual hurricane, the balloon is likely to repeatedly travel to the eye, be drawn up to high altitude and be forced outward and downward, and then travel to the eye, thus continuously measuring the hurricane wind-distribution patterns.

This work was done by Jack A. Jones of Caltech for **NASA's Jet Propulsion Laboratory**. *Further information is contained in a TSP [see page 1].*
NPO-19709

Kinematic Positioning With GPS Pseudorange and Carrier Phase

Accuracy would be 2 to 3 times that of positioning with pseudorange alone.

NASA's Jet Propulsion Laboratory, Pasadena, California

Three techniques have been proposed to increase the accuracy of real-time kinematic positioning via the Global Positioning System (GPS). These techniques involve the processing of simultaneous GPS pseudorange and carrier-phase measurements to estimate position with accuracy greater than that achievable by use of pseudorange alone. The techniques are computationally efficient and thus suitable for implementation in compact navigational electronic equipment

that could be carried aboard airplanes, land vehicles, boats, and Earth-orbiting satellites.

GPS pseudorange measurements provide absolute but crude positioning information, while carrier-phase measurements provide precise information on changes in position; thus, one can determine position with greater accuracy from a combination of pseudorange and carrier-phase data. The "catch" in using carrier-phase data is that each continuous pass of carrier phase measurements is accompanied by an unknown phase bias, so that it is necessary to remove or estimate this bias in processing the data for accurate real-time positioning. The three proposed techniques provide various means to account for phase biases and to use pseudorange and carrier-phase data for kinematic positioning.

For all three techniques, an on-board GPS receiver must be capable of producing pseudorange and carrier phase measurements from multiple GPS satellites. The pseudorange measurements at a single epoch are used to obtain crude estimates of three-dimensional position and time. These estimates are then used as the nominal values for calculation of partial derivatives of measurements with respect to position and time, and are combined with the carrier-phase measurements in the subsequent precise estimation. Pseudorange measurements are valuable in speeding up the convergence of the phase-bias estimates, and thus the position and time estimates. On the other hand, carrier-phase measurements provide ties between successive time points, thus enhancing positioning accuracy.

The three techniques are called "nondifferential," "simple time differential," and "modified time differential." In the nondifferential technique, the estimation process is carried out in a square-root information filter formulation. The estimated parameters include the four-dimensional current state (position and time) and carrier-phase biases. All these are treated as white-noise parameters; the four-dimensional state is to be reset (i.e., white-noise updated) at every epoch, whereas each of the phase biases is to be reset only when its continuity ceases.

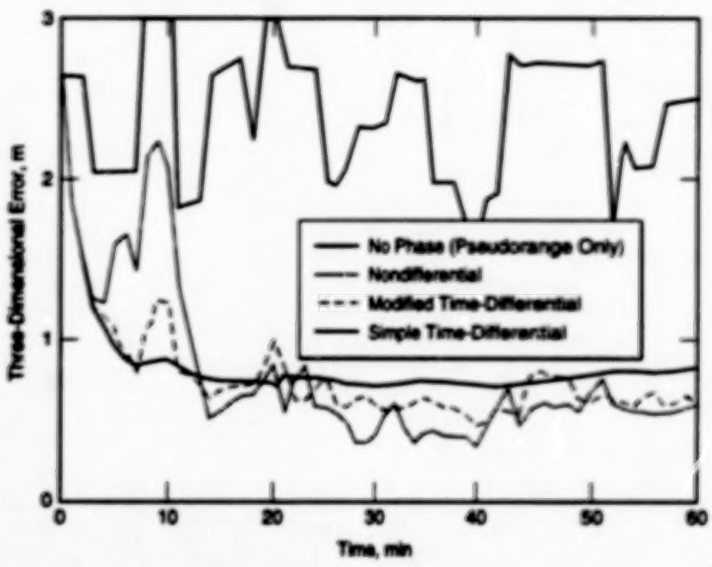

Three-Dimensional Position Error would be reduced by processing carrier phase data along with pseudorange data, using any of the three proposed techniques.

In the simple time-differential technique, phase biases are eliminated by taking differences between phase measurements at consecutive sampling times, and the current four-dimensional state is estimated by use of a recursive formula that incorporates the preceding estimate and the current pseudorange and differenced carrier-phase measurements. In the modified time differential technique, carrier-phase biases are removed in such a way as to recover the absolute-position information embedded in the carrier phase; this involves, among other things, simultaneously estimating the four-dimensional state for both the current and the immediately preceding sampling times.

Without information from ground GPS observations, on-board kinematic positioning is limited by dithering of GPS clock signals pursuant to a policy called "Selective Availability," (SA) in which the precision available to unauthorized users is limited by introducing pseudorandom errors that can be corrected by use of codes available to authorized users. Pseudorange and carrier-phase measurements are equally corrupted by these effects, which are typically tens of meters in magnitude. The SA effects can be removed if, at any epoch, each GPS satellite observed by the user is also observed by a ground station and the information retransmitted to the user for differencing.

The figure is a plot of selected results from a numerical simulation that was conducted to assess the positioning accuracies achievable with the proposed techniques. The simulation was carried out for a GPS user aboard a satellite in orbit around the Earth at an altitude of 700 km. The results of the simulation show that when wide-area differential GPS data for reducing SA clock errors and GPS ephemeris errors are available and the proposed techniques are used, it should be possible to estimate position to within a three-dimensional root-sum-square (rss) accuracy between 0.5 and 0.8 m; this level of accuracy is between 2 and 3 times that achievable with pseudorange measurements alone.

This work was done by Sien-Chong Wu and Thomas P. Yunck of Caltech for **NASA's Jet Propulsion Laboratory**. *Further information is contained in a TSP [see page 1].*
NPO-19575

The γ–μ Method of Designing Achromatic Lenses

Both group and phase indices of refraction are taken into account.

NASA's Jet Propulsion Laboratory, Pasadena, California

The γ-μ (gamma minus mu) method is a powerful and convenient method of designing multiple-element achromatic lenses. The γ-μ method is so named because it involves consideration of the group index of refraction (γ) and the phase index of refraction (μ) of the glass used in each lens element, plus consideration of γ-μ as a measure of the wavelength-dispersive power of the glass.

In the traditional method of designing achromatic lenses, the only index of refraction that is considered is the phase index of refraction, which is what is customarily meant by the unmodified term "index of

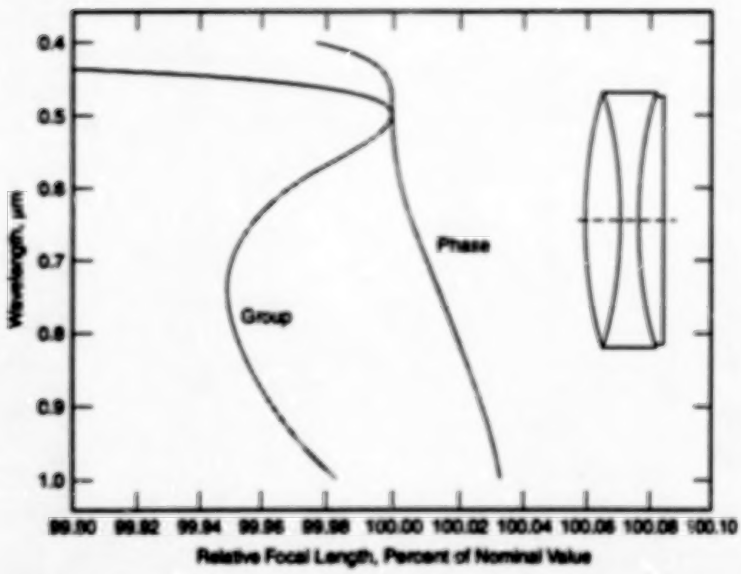

The Wavelength Dependence of Focal Length was computed in thin-lens approximation for a three-element group achromat. The first and second derivatives of phase power with respect to wavelength are constrained to be zero at a wavelength of 0.5 μm, making the lens achromatic and confocal in group and phase power at that wavelength. The inset shows the lens as a cemented triplet at f/7.8 corrected for spherical aberration.

refraction." The measures of wavelength-dispersive power ("dispersion" for short) in the traditional method are the Abbe number and the partial dispersion, which are ratios of differences between phase indices of refraction at different arbitrarily chosen wavelengths. The traditional method is algebraically cumbersome and unduly restrictive when applied to a lens of three or more elements. Unlike the traditional method, the γ-μ method does not involve the arbitrariness of the traditional measures of dispersion and is a practical means for designing a lens of N elements (where N can exceed 3). In addition, the γ-μ method elucidates — perhaps for the first time — the physical significance of group velocity in the performance of a lens.

Some definitions of terms are prerequisite to a summary of the γ-μ method: The group velocity (v_g) in a material is the velocity at which a signal, a wave packet, or photon propagating in the material carries information or energy. The group index of refraction of the material is given by $\gamma = c/v_g$ where c is the speed of light in a vacuum. The group and phase indices of refraction, as functions of wavelength (λ), are related via the equation $\gamma = \mu - \lambda(d\mu/d\lambda)$. The phase power of a lens can be defined as the curvature of the wavefront that emerges from the lens when the lens is illuminated steadily from a distant point source of light. The group power of a lens can be defined as the curvature of the surface of maximum energy density of light that emerges from the lens when the lens is illuminated by an extremely short pulse of light from the same distant point source.

The γ-μ method is based on the observation, derived from fundamental principles of optics, that at a wavelength at which the group power of an N-element lens attains maximum or minimum, the phase power equals the group power. In a lens that comprises three or more elements, the phase and group powers can be made both equal and independent of wavelength in the neighborhood(s) of one or more wavelength(s) (see figure). In such a wavelength neighborhood, the lens is both achromatic and confocal in phase and group power, giving this type of lens an unprecedented degree and type of achromatism, called "group achromatism." A lens of this type is denoted a group achromat.

An important byproduct of the development of the γ-μ method is a method for choosing an optimal combination of glasses for the N elements of an achromatic lens. In this method, one can easily apply chromatic constraints more general than the conventional ones. Furthermore, the computation for an N-element lens reduces to a system of linear equations that can be solved easily by a matrix formalism that involves computation of the inverse of an $N \times N$ matrix defined in terms of the indices of refraction of the glasses. The value of the determinant of the matrix, which can be interpreted in terms of an N-dimensional geometry, becomes a measure of the degree to which the combination of glasses satisfies the given set of constraints.

This work was done by Arthur H. Vaughan of Caltech for **NASA's Jet Propulsion Laboratory**. *Further information is contained in a TSP [see page 1].*
NPO-19702

Evaluating Effects of Weather on Optical Communications

A mathematical model incorporates statistics from observations of visibility through the atmosphere.

NASA's Jet Propulsion Laboratory, Pasadena, California

A method of evaluating the effects of weather on optical communication links from spacecraft to ground involves the use of an empirical mathematical model for attenuation of signals in the atmosphere. The method is related to an older method of evaluating a radio-communication link, wherein one takes account of gains and losses in estimating the amount of signal power needed to ensure some baseline level of performance, and the link is designed with greater power; the extra power is called "link margin" and can be incorporated into the design as a precaution against uncertainty in design assumptions and/or to enhance performance.

A basic assumption of the present method is that local weather at each ground receiving station severely affects reception of signals and, therefore, a satellite-to-ground optical-communication system will include multiple ground stations in a diversity reception scheme. In this case, diversity entails locating stations far enough apart (e.g., hundreds of kilometers) that they can be considered to be exposed to different weather conditions. In designing such a system and analyzing its performance, the availability of each station must be defined, and it is necessary to quantify the link margin needed to accommodate link uncertainties accurately. In the older method of calculating link margin,

one does not take atmospheric attenuation into account, with the result that a system designed by that method can end up over- or underdesigned.

In the present method, one does not use the power-based measure of link margin of the older method; instead, one uses a different metric, called the "expected data volume" (EDV), which takes account of both availability and uncertainties in atmospheric attenuation. As a prerequisite to a description of how this is done, it is necessary to define the terms "available," "unavailable," and "availability" as used in this special context. A ground station is said to be available or unavailable at given instant if, at that instant, the atmospheric attenuation there is less than or greater than α, respectively. "Availability" is defined as the nominal probability P_a that the atmospheric attenuation will be less than or equal to a specified amount α (see figure). The figure contains a representative plot of P_a versus α; the plot includes a nominal curve within a band that represents the uncertainty $\Delta\alpha$ in atmospheric attenuation.

One can construct a mathematical model of P_a and $\Delta\alpha$ as functions of α from statistical data on cloudiness. Such data are being gathered by three diverse (in the sense defined above) observatories (two in California, one in Arizona) that monitor the intensities of light received from known stars of known brightness.

Consider a set of N stations capable of viewing the spacecraft source of the optical signal under cloud-free conditions ("candidate stations," for short). The probability $P_N(m)$ that m of those stations are available is given by

$$P_N(m) = B(N,m)P_a^m(1-P_a)^{N-m},$$

where $B(N,m)$ denotes the binomial coefficient [the number of combinations of N things taken m at a time; that is, $N!/m!(N-m)!$]. The probability P_N that at least one of the stations is available is given by

$$P_N = \sum_{m=1}^{N} P_N(m) = 1-(1-P_a)^{N-m}$$

This is the "joint availability" of the network of ground stations to receive a downlink signal if everything is constant. In practice, the number of candidate stations changes with rotation of the Earth and motion of the source. Suppose that total downlink time is T, which is divided into K disjoint segments $t_1, t_2, \ldots t_K$, such that during each segment t_i there are N_i candidate stations. Suppose also that when at least one station is available, it is possible to reliably receive data transmitted from the source at a rate R. Then the expected data volume is defined as the volume of data expected to be received during T and is given by

$$EDV = R\sum_{i=1}^{K} t_i P_{N_i}$$

This is the metric for determining the capability of the link. The EDV and the underlying methodology are proposed for use when making comparisons between proposed radio-frequency and optical communication links.

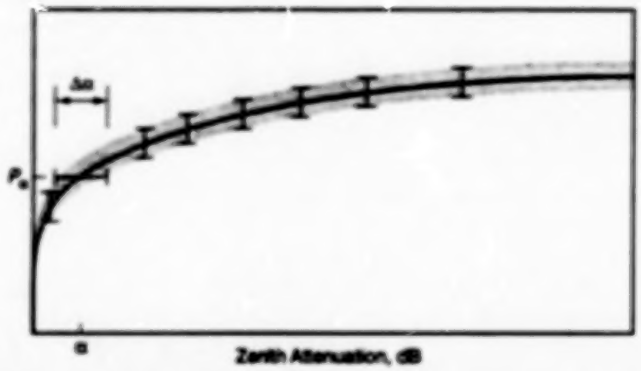

A Cumulative Probability Distribution of α for a typical ground receiving station would look like this plot. The α represented on this plot is zenith attenuation. When analyzing an optical communication link with reception from an off-zenith direction, the path length is greater and thus the value of α must be increased. For design, the α for the largest expected zenith angle should be used.

This work was done by James R. Lesh of Caltech for **NASA's Jet Propulsion Laboratory**. *Further information is contained in a TSP [see page 1].*
NPO-19774

Apparatus for Advanced Ultrasonic C-Scan Imaging

C-scan plots indicate both amplitude and depth.

Goddard Space Flight Center, Greenbelt, Maryland

Figure 1 schematically illustrates a computer-controlled ultrasonic C-scan instrumentation system that incorporates recent advances in hardware and software for better characterization of specimens. In some respects, this system operates like a typical ultrasonic C-scan apparatus of older design. The innovative aspects of this system lie in the specific combination of signal- and data-processing functions to obtain plots containing two types of data that characterize defects in specimens.

Like some other systems, this system includes an ultrasonic transducer that is scanned along in a horizontal (x,y) plane parallel to the top surface of a nominally flat plate specimen, which is typically laminated. As in other systems, the ultrasonic transducer is connected to an electronic pulser/receiver, a dual timing gate, a peak detector, and a universal timer. At each position x,y along the scan, the computer estimates the depth of any defect or other feature that reflects ultrasound, using the known or assumed speed of sound and the measured round-trip travel time (also called "time of flight," or "TOF," for short) of the ultrasonic signal between the top surface of the specimen and the defect. The peak detector operates with a time gate chosen so that its output indicates the amplitude of the signal reflected from the defect or other feature at x,y.

Some older ultrasonic C-scan systems generate similar data on depth and amplitude as functions of x and y, but they lack the means to correlate the depth and amplitude data automatically and are limited to presenting depth and amplitude data on separate plots. The software of the present system includes a program that processes the x,y scanning-position data and the associated depth and amplitude data into a single three-dimensional-appearing plot that shows both depth and amplitude as

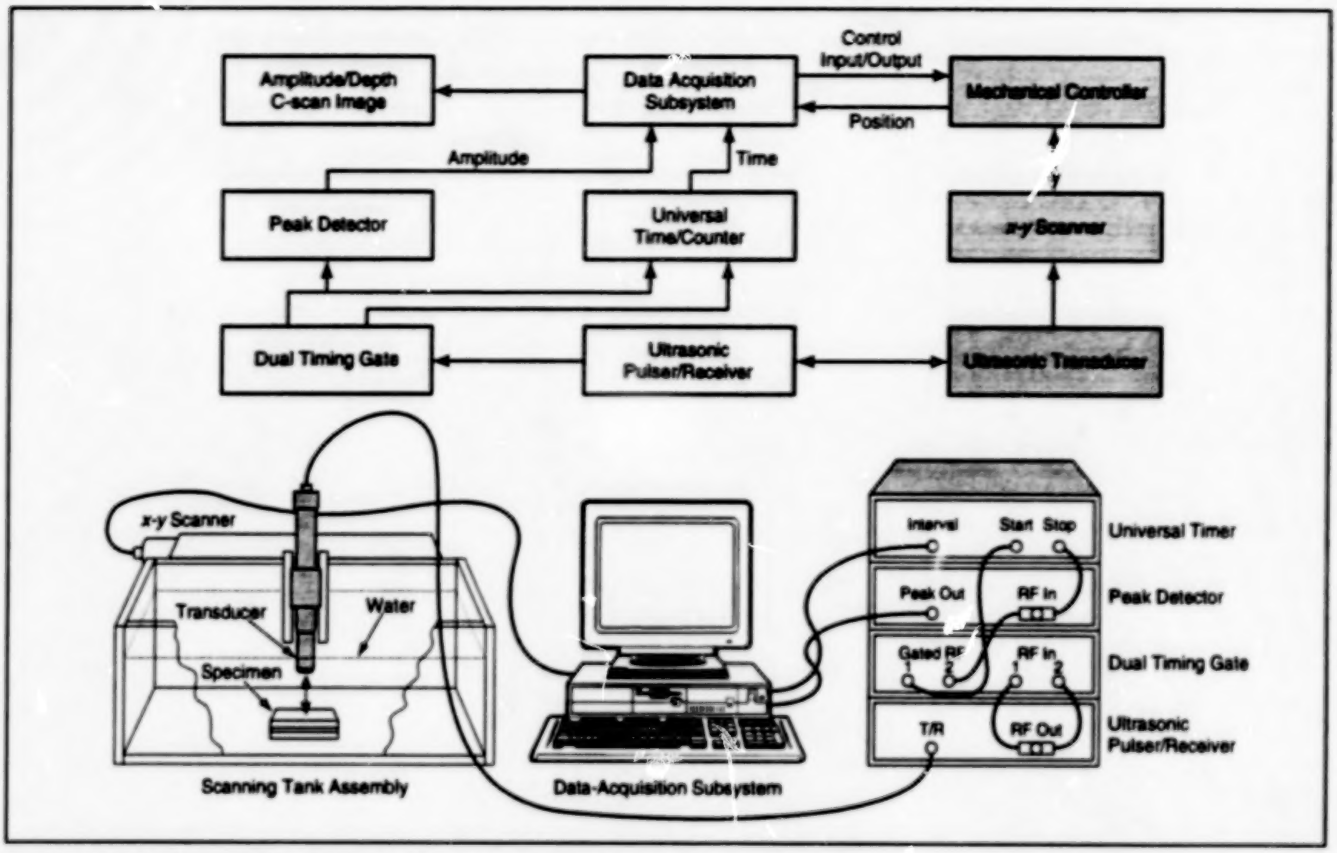

Figure 1. This Instrumentation System performs an ultrasonic C-scan of a plate specimen.

functions of *x* and *y*. Figure 2 shows an example of such a plot, wherein the vertical (*z*) axis represents depth, and a gray scale indicates amplitude. Alternatively, false color could be used to indicate amplitude.

This work was done by Engmin James Chern and David Warren Butler of **Goddard Space Flight Center**. *Further information is contained in a TSP [see page 1].*

This invention is owned by NASA, and a patent application has been filed. Inquiries concerning nonexclusive or exclusive license for its commercial development should be addressed to the Patent Counsel, Goddard Space Flight Center [see page 1]. Refer to GSC-13524.

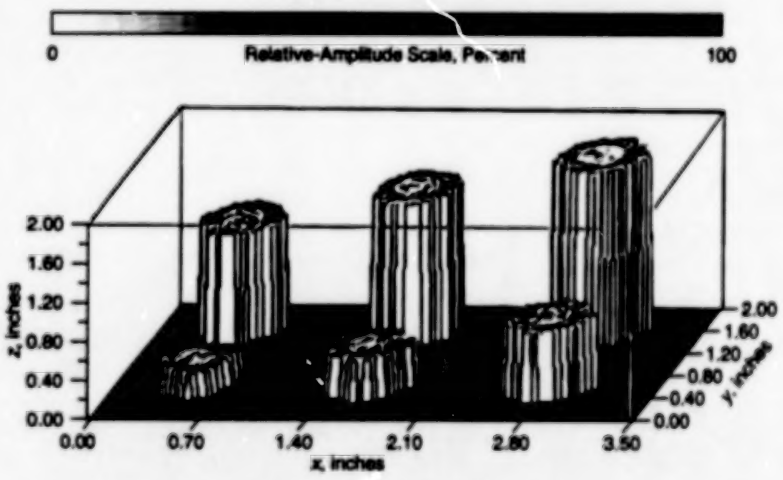

Figure 2. This Plot Presents Ultrasonic C-Scan Data from a specimen that contained six disk-shaped defects at various depths with features to reflect ultrasound with differing amplitudes.

Ultrasonic Instrument Produces Thickness-Independent Velocity Images

Thickness effects can be eliminated, yielding images indicative of properties of materials.

Lewis Research Center, Cleveland, Ohio

A weakness of conventional C-scan imaging regarding both peak amplitude and time-of-flight modes is that gray or color scale variations in images for back-surface reflections indicate part-thickness variations, as well as microstructural variations, unless the part is uniformly thick. A single transducer ultrasonic imaging method based on ultrasonic velocity measurement is described here that eliminates the effect of plate-thickness variation in the image, i.e., the method is thickness-independent. The method thus isolates ultrasonic variations due to material microstructure.

The present imaging subsystem is incorporated into a conventional ultrasonic C-scan apparatus with a single ultrasonic transducer and a computer with conventional ultrasonic-signal-processing software plus special software to implement the subsystem computations. The apparatus is set up for pulse/echo measurements of the velocity of sound in a tank of water.

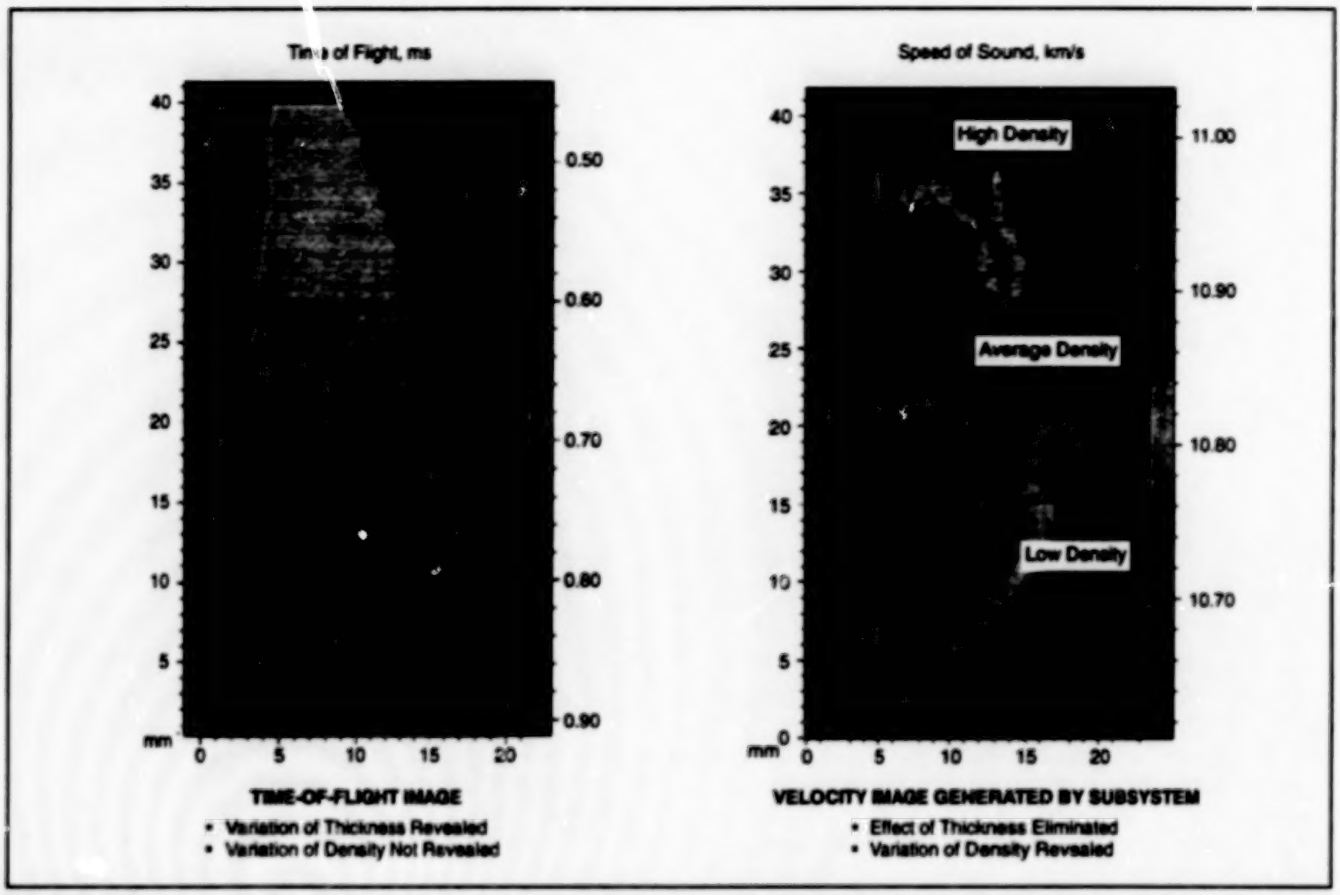

Gradients of Density are indicated in the velocity image generated by the subsystem described in the text, whereas only the variation of thickness is depicted in the time-of-flight image.

The transducer is mounted in the water on a scanning mechanism above the specimen. Below the specimen is a plate for reflecting ultrasound. At each scan position, the ultrasonic echoes from the surfaces of the specimen and the plate are analyzed to determine the speed of sound in the specimen material.

The subsystem is expected to find use in numerous applications in which there is a need for nondestructive detection of flaws in structural parts and nondestructive evaluation of spatially varying properties of materials. In the case of advanced ceramic materials undergoing development in the aerospace and automotive industries, gradients of density, porosity and chemical composition are properties that are of particular interest and that affect the speed of sound. The data generated by the ultrasonic apparatus equipped with this subsystem quantify such gradients about 10 times better than do the data generated by the same apparatus operating in the traditional peak-echo-amplitude or relative-echo-time (time-of-flight) mode.

The figure illustrates the superior capability of this subsystem for revealing gradients of density in a specimen of a ceramic material that is under consideration to replace metal parts in automobiles. The specimen is 0.3 mm thicker at the top of the figure than at the bottom, and varies smoothly from top to bottom. The specimen contains distinct regions of low (95 percent of theoretical), average (98 percent of theoretical), and high (100 percent of theoretical) density. The image in the left part of the figure was generated in an ultrasonic C-scan in a conventional time-of-flight mode; this image indicates the variation in thickness from top to bottom, but gives no indication of the variation in density. The image in the right part of the figure, generated by scanning the specimen while using the present subsystem, clearly reveals the variation in density, without the effect of thickness.

This work was done by Don J. Roth of **Lewis Research Center**, *Mike F. Whalen and J. Lynne Hendricks of Sonix, Inc., and John H. Hemann and James R. Bodis of Cleveland State University. Further information is contained in a TSP [see page 1].*

Inquiries concerning rights for the commercial use of this invention should be addressed to NASA Lewis Research Center, Commercial Technology Office, Attn: James Martz, Mail Stop 7–3, 21000 Brookpark Road, Cleveland, Ohio 44135. Refer to LEW-16257.

Optically Implementing an Algorithm for Representing Images

The matching-pursuit algorithm has been adapted to image-analysis applications.

NASA's Jet Propulsion Laboratory, Pasadena, California

A prototype optoelectronic apparatus has been developed to implement an improved scheme for the analysis and representation of images. The scheme is based on an adaptation of an algorithm, called the "matching-pursuit" algorithm, that was originally formulated for use in analyzing sound and other time-varying signals. A system that implements this scheme automatically and rapidly decomposes a two-dimensional image into a linear combination of elemental images from

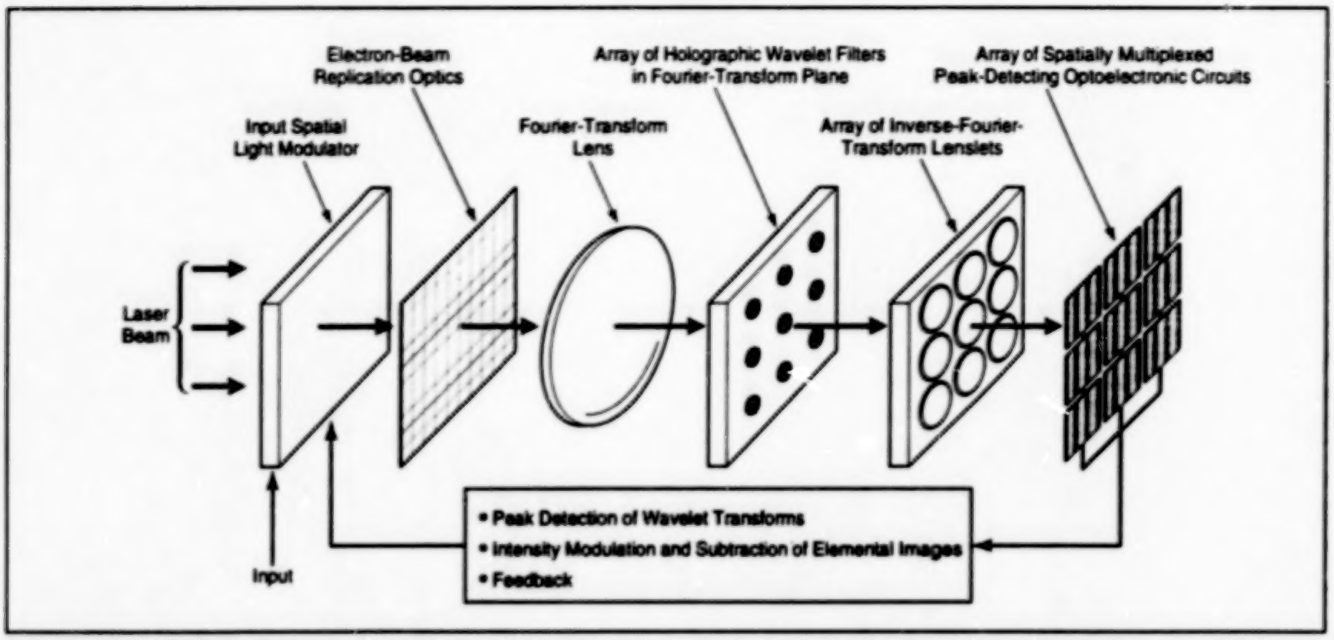
Electron-Beam Replication Optics
Array of Holographic Wavelet Filters in Fourier-Transform Plane
Array of Spatially Multiplexed Peak-Detecting Optoelectronic Circuits
Input Spatial Light Modulator
Fourier-Transform Lens
Array of Inverse-Fourier-Transform Lenslets
Laser Beam
Input
• Peak Detection of Wavelet Transforms
• Intensity Modulation and Subtraction of Elemental Images
• Feedback

This **Apparatus Optically Performs** the most computation-intensive operations of the adapted matching-pursuit algorithm as applied to representation of images.

a dictionary of such images. Thus, the scheme offers potential utility for analysis of images and compression of image data. Moreover, the elemental images could be patterns that the system is required to recognize, so that the scheme offers potential utility for industrial and military applications that involve robotic vision and/or automatic recognition of targets.

The original version of the matching-pursuit algorithm expresses a sound or other signal as a linear combination (a finite series) of unit-norm elemental waveforms from a highly redundant dictionary of waveforms. The elemental waveforms and their coefficients in the series are chosen in decreasing order of correlation with the signal, where correlations are expressed in terms of inner-product integrals and each successive term in the series is applied to only the residue left after the approximation formed by the preceding terms. Thus, the matching-pursuit algorithm is a greedy algorithm, and each successive term in the series is less significant than is the one preceding it.

Unlike sound waveforms, which are functions of time and have zero means, image data are positive distributions of light intensity in two dimensions, and it is desired to classify them in terms of known images rather than known waveforms. These considerations must be taken into account in adapting the matching-pursuit algorithm to the image-representation problem. Accordingly, the elemental functions chosen for inclusion in the dictionary are two-dimensional brightness-distribution functions (that is, elemental images) that are sufficiently similar to targets that one seeks to recognize and sufficiently dissimilar to decoys or other extraneous objects that one seeks to ignore. Similarity and dissimilarity are quantified, for these purposes, in terms of correlations or inner-product integrals over the image area. The dictionary should include all elemental images of interest, including a representative selection of translated, rotated, magnified, and minified versions of the elemental images that could be encountered in practice.

The matching-pursuit algorithm as adapted to representation of an image requires iterative performance of three basic operations: (1) two-dimensional adaptive wavelet transforms that represent the elemental images; (2) peak detection for those transforms; and (3) subtraction, from the input image, of intensity-modulated versions of the elemental images. An optical or optoelectronic image-processing system like the prototype apparatus can perform all three operations in much less time than would be needed to perform the same operations on a digital electronic computer.

The prototype apparatus (see figure) includes a spatial light modulator, electron-beam replication optics, a Fourier-transform lens, an array of holographic wavelet filters, an array of inverse-Fourier-transform lenslets, and an array of interconnected integrated-circuit chips, each of which contains a two-dimensional array of photodetectors and associated peak-detection circuitry. In order to identify the wavelet that would produce the maximum wavelet-transform peak against the input image, it is necessary to conduct an exhaustive search.

First, all wavelet elements in the dictionary are arranged in a two-dimensional array of Fourier holograms that constitutes the array of holographic wavelet filters mentioned above. Multiple replicas of the input image — one for each filter — are formed by use of electron-beam optics. The Fourier transform of each replica is formed in the corresponding filter. A two-dimensional array of lenslets inverse-Fourier-transforms the outputs from the filters, producing the corresponding wavelet transforms on the corresponding photodetector/peak-detector circuits. The output of each such circuit yields data on the locations of all pixels with intensities above a threshold level. The outputs of all of these circuits are monitored simultaneously. The threshold level is increased until the brightest of the peaks found by the photodetectors is identified. This peak value and location of this peak and the identity of the corresponding wavelet are recorded for use in subsequent operations.

The brightness of the elemental image associated with the identified wavelet is then multiplied by this peak value (this is the intensity modulation mentioned above), recentered at the identified location, and subtracted from the input image. The remaining image (residue) is then fed back as the input image for the next iteration. The iterations continue until the energy in the residue falls to

zero or exhibits a tendency to increase or oscillate with further iteration.

Some preliminary optical experiments have demonstrated that the system operates substantially as expected. In addition, the adapted matching-pursuit algorithm has been verified through computational simulation.

This work was done by Tien-Hsin Chao and Brian K. Lau of Caltech and William J. Micell of the Office of Naval Research for **NASA's Jet Propulsion Laboratory**. *Further information is contained in a TSP [see page 1].*
NPO-19471

BLANK PAGE

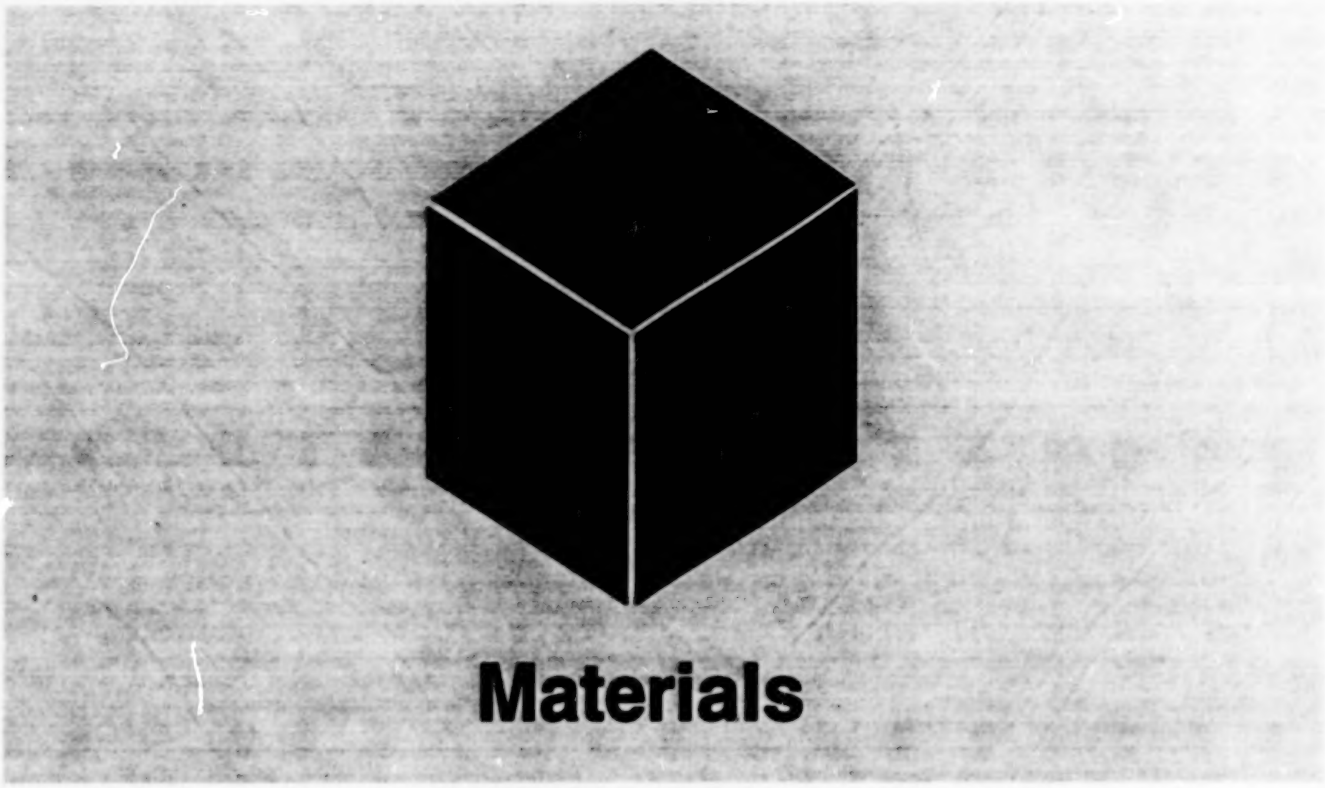

Materials

Hardware, Techniques, and Processes

35 Modification of Carbon Fibers for Higher Young's Modulus
36 Toughened Carbon/Carbon Pistons
36 High-Performance Silver-Recovery Apparatus

BLANK PAGE

Modification of Carbon Fibers for Higher Young's Modulus

The Young's modulus of carbon fibers is increased after a cycle of fluorination-defluorination treatment.

Lewis Research Center, Cleveland, Ohio

Processes for the defluorination of graphite fluoride fibers have been developed as means of producing new, chemically modified carbon-fiber materials. The starting materials and process conditions for defluorination can be chosen so that the resulting modified carbon fibers take on properties that are desired in specific applications. The chemically modified carbon materials have interplanar spacings in the range of 3.35 to 3.45 Å. Some of the modified carbon-fiber products exhibit very high moduli of elasticity, which heretofore have been achievable only with extreme difficulty. Other of these products, generally denoted as "activated graphite," can be used to make stronger metal-matrix/carbon-fiber composite materials because they are more wettable by metal matrix materials than are carbon fibers made by older methods.

In an older method of defluorination of graphite fluoride (heating in an inert environment), fluorine atoms leave the graphite fluoride and take significant numbers of carbon atoms with them. Consequently, the carbon material left after defluorination is extensively damaged and, therefore, not useful. Moreover, the process in the older method is difficult to control because the defluorination is either (a) slow and incomplete if done at a temperature < 400 °C or else (b) likely to turn explosive if heating is done rapidly at a temperature > 400 °C. In a precursor to the present method, the graphite fluoride fibers are treated in bromine vapor at a temperature of 350 °C. Defluorination in this case is faster and more complete than when done in an inert environment, but the material is still damaged significantly.

The present method involves the use of halocarbon compounds to heal some of the damage as defluorination proceeds. The figure schematically illustrates a typical process according to this method. First, the graphite fluoride fibers, obtained by fluorination of carbon fibers, are exposed to a suitable halocarbon gas (e.g., CCl_4, $CHBr_3$, $Br_2CHCHBr_2$, or $BrCH_2CH{=}CHCH_2Br$) at a temperature between ambient and 250 °C to let the halocarbon molecules diffuse into the graphite fluoride molecular structure in preparation for the defluorination-and-healing process. Then, while maintaining the same halocarbon atmosphere, the fibers are heated to a temperature between 250 and 450 °C for an interval between 2 and 10 h; this heating effects the first-step defluorination, in which the majority of fluorine atoms are detached from the carbon atoms in CF_x and quickly removed from the proximity of graphite fluoride by reacting to the halocarbons. Simultaneously with the defluorination, the halocarbons go, variously, to the sites vacated by the fluorine atoms and to sites that contain damage and defects. Thus, the halocarbon molecules not only enhance the rate of defluorination, but also prevent and heal the damage. Depending on the length of the halocarbon molecules, these molecules may produce crosslinks of the molecular structure in the carbon material and thereby produce a new carbon material; namely, graphite with its adjacent carbon layers crosslinked.

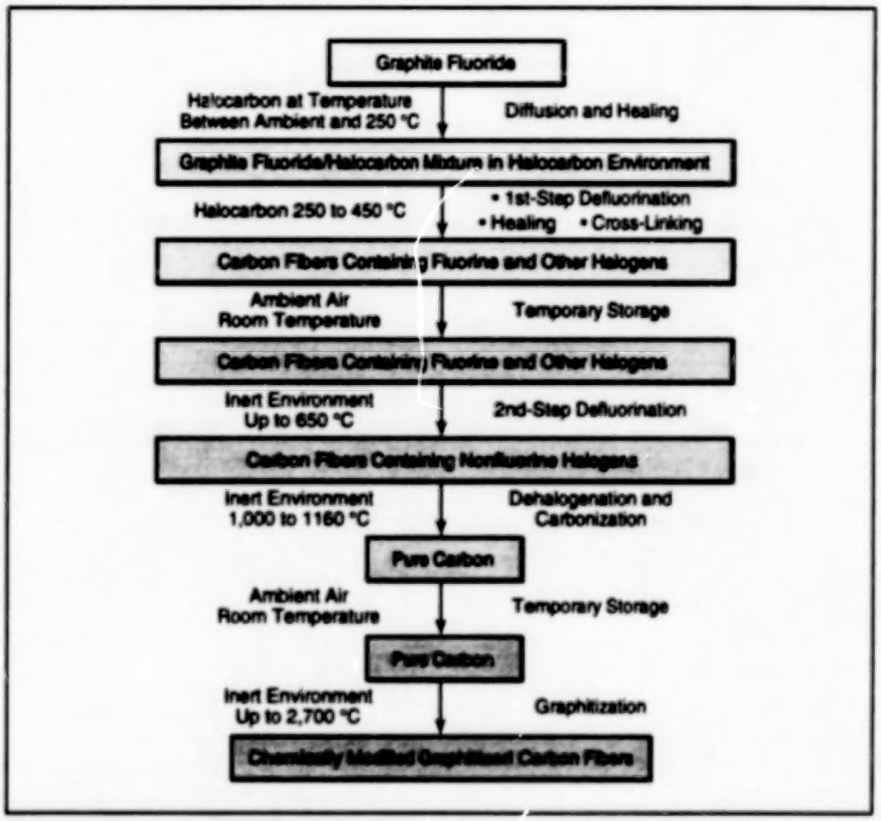
Graphite Fluoride
Halocarbon at Temperature Between Ambient and 250 °C
Diffusion and Healing
Graphite Fluoride/Halocarbon Mixture in Halocarbon Environment
Halocarbon 250 to 450 °C
• 1st-Step Defluorination
• Healing • Cross-Linking
Carbon Fibers Containing Fluorine and Other Halogens
Ambient Air Room Temperature
Temporary Storage
Carbon Fibers Containing Fluorine and Other Halogens
Inert Environment Up to 650 °C
2nd-Step Defluorination
Carbon Fibers Containing Nonfluorine Halogens
Inert Environment 1,000 to 1160 °C
Dehalogenation and Carbonization
Pure Carbon
Ambient Air Room Temperature
Temporary Storage
Pure Carbon
Inert Environment Up to 2,700 °C
Graphitization
Chemically Modified Graphitized Carbon Fibers

This Multistage Process yields graphitelike carbon fibers with physical and chemical properties that are useful in selected applications.

The halocarbon molecules should be small so that they can enter the molecular structure of the graphite fluoride. All of the fluorocarbon compounds mentioned above have molecules that are small enough; they can prevent and heal the damage during the first-step defluorination. However, with respect to effectiveness as a cross-linking agent, the ability of CCl_4 is weak or nonexistent, the abilities of $CHBr_3$ and $Br_2CHCHBr_2$ are moderate, and that of $BrCH_2CH{=}CHCH_2Br$ is strong.

After the first-step defluorination, the carbon material still contains some fluorine (up to 11 percent of the weight of the carbon) plus other halogens (up to 31 percent) from the halocarbons. Therefore, after removing this carbon material from the halocarbon environment to ambient air for temporary storage, the material is subjected to second-step defluorination, in which it is heated in an inert environment (e.g., a nitrogen atmosphere) to a temperature of 600 °C to remove most or all of the remaining fluorine and some of the other halogens. The fibers are further heated in an inert environment to a temperature between 1,000 and 1,160 °C to remove most or all of the remaining halogen atoms.

After a second interval of temporary storage in ambient air, the fibers are heated in an inert environment (argon atmosphere) to a temperature of as much as 2,700 °C to increase the degree of graphitization and thereby increase the

modulus of elasticity and thermal conductivity of the fibers. The properties of the carbon fibers thus produced depend on the temperatures and other particulars of the various stages of the process, including the final heating stage. In particular, according to the process described in the figure, when the graphite fluoride reactant was made from pitch-based carbon fibers having modulus of elasticity of 105 Msi and $BrCH_2CH{=}CHCH_2Br$ was chosen during the first-step defluorination, the final carbon fiber product was found to have modulus of elasticity value much higher than 120 Msi. Such an increase in modulus of elasticity is believed to be due to the cross-linking between the adjacent graphite layers.

This work was done by Ching-cheh Hung of **Lewis Research Center**. *Further information is contained in a TSP [see page 1].*

Inquiries concerning rights for the commercial use of this invention should be addressed to the Patent Counsel, Lewis Research Center [see page 1]. Refer to LEW-15847.

Toughened Carbon/Carbon Pistons

Three-dimensional carbon/carbon would be toughened with metal or plastic in its pores.

NASA's Jet Propulsion Laboratory, Pasadena, California

Carbon/carbon pistons of a proposed type would be tougher than those that have been tested thus far and would thus be capable of withstanding the high temperatures and high impacts of use in internal-combustion engines. The state-of-the-art carbon/carbon pistons that the proposed pistons would replace tend to fail prematurely in use because they are brittle.

The state-of-the art carbon/carbon pistons are made with carbon fibers oriented predominantly in two dimensions. However, three-dimensional carbon/carbon composite materials would be used in the proposed pistons. Fabrication of a piston would begin with weaving a preform to near net shape, using carbon fibers oriented in three orthogonal directions. The preform would then be partly densified into carbon/carbon by use of a highly graphitizable matrix precursor like petroleum or synthetic pitch, leaving a porosity of about 15 percent.

By use of resin-transfer molding, the pores would be filled with a metal or a thermoplastic like poly(ether ether ketone) (PEEK), which would serve as a toughening agent. The part would then be machined to net shape.

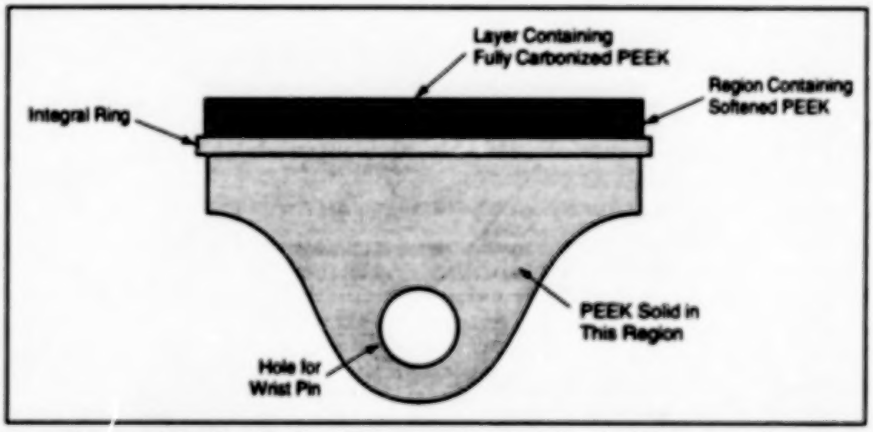

In a Proposed Carbon/Carbon Piston made of partly densified three-dimensional carbon/carbon filled with PEEK as a toughening agent, the PEEK would become carbonized at the combustion-chamber surface during operation, would be softened in the cooler layer below this surface, and would be solid (providing maximum reinforcement) in the highly stressed region around the wrist-pin hole.

During operation, in the case of PEEK, a layer of PEEK would become carbonized at the combustion chamber surface of the piston (the top surface in the figure). Immediately below that surface, the PEEK would be soft, so that the carbon/carbon composite in that region would bear all of the load. The regions farther below would be cooler, and would be coolest (at the temperature of the engine oil) in the vicinity of the wrist pin. The PEEK would be solid in these lower regions, providing the greatest support where stresses would be the greatest.

This work was done by D. Kyle Brown of Caltech for **NASA's Jet Propulsion Laboratory**. *Further information is contained in a TSP [see page 1].*
NPO-19592

High-Performance Silver-Recovery Apparatus

An apparatus at Kennedy Space Center recovers silver from liquid waste produced during the development of photographic and radiographic film. In comparison with previously available silver-recovery equipment, this apparatus recovers a greater proportion of silver from the waste stream. In this apparatus, dissolved silver is removed from the waste stream by exchanging silver ions for iron ions in sacrificial cartridges in treatment cells, while particulate silver is removed by filtering. The system includes several treatment cells in series; a "lead" (farthest upstream) cell followed by a "lag" cell followed by a tailing or "polishing" stage that comprises a dual cell plus a single cell. When the concentration of silver in the lead-cell cartridge reaches the maximum allowable, this cartridge is removed to harvest the silver, the cartridge from the lag cell is moved to the lead position, and a fresh cartridge is placed in the lag cell. The apparatus treats as much as 15 gallons (~166 liters) of waste per day, recovering more than 99.9 percent of the silver. The concentration of silver in the effluent is no more than 5 parts per million — low enough to permit the effluent to be sent to a sewage-treatment plant.

This work was done by Edsel W. Fickey, Daniel J. Tierney, and Clarence E. Gillenwater of EG&G Florida, Inc., for **Kennedy Space Center**. *Further information is contained in a TSP [see page 1].*

Inquiries concerning rights for the commercial use of this invention should be addressed to the Patent Counsel, Kennedy Space Center [see page 1]. Refer to KSC-11846.

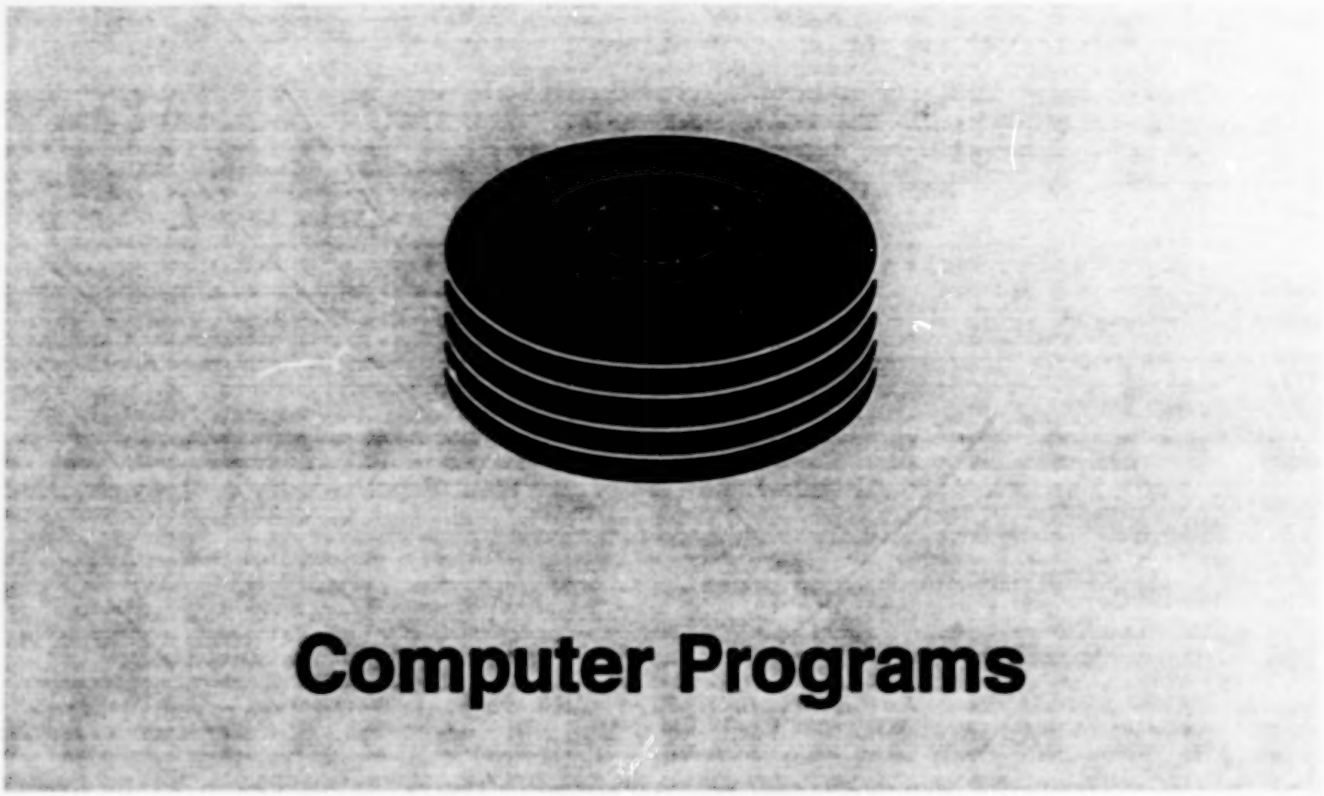

Computer Programs

Electronic Components and Circuits

39 Computing Characteristics of Dual-Reflector Antennas

Physical Sciences

39 Software for the Airborne Emission Spectrometer
39 Software for Analyzing Vibrations of Levitated Liquid Drops
40 Software for Exciting Vibrations of Levitated Liquid Drops

Mathematics and Information Sciences

40 Software Manages Recorded Data Structures
40 Automated Monitoring With Learned Envelope Functions
40 Software for Operating on Image Data

BLANK PAGE

Computer Programs

These programs may be obtained from COSMIC. Please contact

COSMIC®
Computer Services Annex
University of Georgia
Athens, GA 30602
Telephone No. (404) 542-3265.

Electronic Components and Circuits

Computing Characteristics of Dual-Reflector Antennas

Characteristics include gain, aperture efficiency, side-lobe level, and cross polarization.

The DUALREF computer program accurately predicts radiation characteristics of microwave antennas. Such antenna radiation characteristics as beam width, gain, aperture efficiency, side-lobe level, and cross polarization are used in analyzing and designing advanced antenna systems. While the single offset paraboloid has been the configuration used most extensively for satellite multiple-beam antennas, the trend toward large apertures and toward requirements for minimum degradation of scanned beams over the field of view (18° wide for full coverage of the Earth from geostationary orbit) may lead to impractically long focal lengths and large feed arrays. On the other hand, dual-reflector antennas offer packaging advantages and more degrees of design freedom to improve beam scanning and cross-polarization properties. Reflector antennas are widely used in communication satellite systems because they provide high gain at low cost. The Cassegrain and Gregorian antennas are the most commonly used dual-reflector antennas. DUALREF can calculate the secondary patterns and directivities of these antennas and of any similar generalized dual-reflector antenna system.

DUALREF uses the physical-optics-current methodology for describing the induced currents on the sub- and main reflectors. The resulting induced currents on the main reflector satisfy Maxwell's equations, so they are integrated to obtain the antenna far-zone electric fields. The output of the program describes such antenna radiation characteristics as beam width, gain, aperture efficiency, side-lobe level, and cross polarization. This program has been verified with other physical-optics programs and with measured antenna patterns, and the comparison shows good agreement in far-field side-lobe reproduction and directivity.

DUALREF is written in Microsoft Fortran PowerStation for IBM PC-compatible computers running Windows 3.1, Windows 95, or Windows NT. Microsoft Fortran PowerStation for Windows and a plotting program (e.g., MATLAB or Mathcad 5.0 Plus) are required. DUALREF has been successfully implemented on an IBM PC-compatible 486DX/33 computer running Windows 95. The standard distribution medium for DUALREF is one 3.5-in. (8.89-cm), 1.44MB, MS-DOS-format diskette. The contents of the diskette have been compressed by use of the PKWARE archiving software tools. The utility software to unarchive the files, PKUNZIP.EXE v2.04g, is included. DUALREF was released to COSMIC in 1996.

This program was written by Roberto J. Acosta of **Lewis Research Center**. *Further information is contained in a TSP [see page 1].*
LEW-16226

Physical Sciences

Software for the Airborne Emission Spectrometer

Special-purpose software has been developed to support both in-flight and ground processing of data from the Airborne Emission Spectrometer (AES), a Fourier-transform spectrometer for studying tropospheric chemistry from a variety of airborne platforms. The AES support software includes components in three categories; decommutation, cataloging, and utilities. The decommutation software transforms the spectrometer readout data from instrument format to a format suitable for calibration and further processing; it is used for both routine processing and for testing the instrument. The cataloging software generates catalog and data-quality information stored in a relational database. The utilities were developed as needed to perform specific functions, including copying data onto and from magnetic tape, "smart" downloading of data, geolocation, extraction of specified subsets of data, and averaging. The decommutation and cataloging software were designed concurrently with the AES hardware. Overlapping functional requirements in the support software were identified early in the design effort, enabling the reuse of many software components. Overall, the AES support software comprises 326 modules, of which only 171 are unique.

This program was written by Steven Larson of Caltech for **NASA's Jet Propulsion Laboratory**. *Further information is contained in a TSP [see page 1].*
NPO-19917

Software for Analyzing Vibrations of Levitated Liquid Drops

The STV-Data Analyze computer program extracts frequencies and damping parameters from raw data acquired in laboratory observations of vibrations of electrostatically levitated liquid drops. The frequencies and damping parameters of these vibrations are used to calculate the surface tensions and viscosities of the drops. The program reads a raw data file in a format used in the laboratory observations, high-pass filters the data, provides for selection of the relevant portion of the data, then performs a nonlinear least-squares fit of the filtered, selected data to the product of (1) a decaying exponential and (2) a sine wave, the frequency of which changes linearly with time. The parameters reported as a result of this fit are the exponential-decay time constant, the initial frequency, the coefficient of change of frequency with time, and the approximate standard deviations of the foregoing quantities. Optionally, the program writes the filtered, selected data to an ASCII file for further processing. The program is optimized for the specific raw-data format and the specific fitting function. The program was written as a Virtual Instrument in version 3.0.1 of the LabVIEW software system, and can be executed only within that system. Also needed for execution is a Macintosh (or

equivalent) computer with a 68040 (or better) processor and at least 16MB of random-access memory (RAM), or else a Power Macintosh (or equivalent) computer with at least 24 MB of RAM.

This program was written by Erik Sjout and Won-Kyu Rhim of Caltech for **NASA's Jet Propulsion Laboratory**. *Further information is contained in a TSP [see page 1].*
NPO-20000

Software for Exciting Vibrations of Levitated Liquid Drops

The Excite to Disk computer program governs the generation of a sinusoidal voltage of specified frequency, amplitude, and duration for exciting the vibrations described in the preceding article. Following the excitation, this program records the vibrational response, time-stamps the response data, and writes the resulting data to a hard disk in a binary format that occupies less disk space than does an ASCII format: these are the raw data mentioned in the preceding article. Also recorded on the disk are ancillary data on experimental conditions and notes written by the experimenter. The program also high-pass-filters the data, displays the filtered data as a function of time, computes a fast Fourier transform (FFT) of the filtered data under the assumption that the data represent an exponentially decaying sinusoid, displays a power spectrum based on the FFT, and estimates the values of exponential-decay time constant and the frequency from the FFT and from the period between zero crossings. Like the program described in the preceding article, this program was written as a Virtual Instrument in version 3.0.1 of the LabVIEW software system, and can be executed only within that system on either a Macintosh (or equivalent) computer with a 68040 (or better) processor and at least 16MB of random-access memory (RAM) or else a Power Macintosh (or equivalent) computer with at least 24 MB of RAM. Also needed for execution is version 4.7.03 of the NI-DAQ software.

This program was written by Erik Sjout and Won-Kyu Rhim of Caltech for **NASA's Jet Propulsion Laboratory**. *Further information is contained in a TSP [see page 1].*
NPO-20001

Mathematics and Information Sciences

Software Manages Recorded Data Structures

The Spacecraft Data Recorder (SDR) computer program enables flight software in a spacecraft (or similar software in a terrestrial application) to manage data structures (e.g., link lists and tables) recorded in a persistent medium such as a magnetic disk or a solid-state recorder based on nonvolatile random-access memory. The SDR software also prevents corruption of persistent data by errors in application programs or by rebooting of computers. The data structures are treated as objects in the C programming language. The software supports the use of an abstract data-recording device, which is also denoted "SDR." The SDR abstraction insulates the application software from the specific characteristics of the real data-storage device and, as much as possible, from traditional data-storage and -retrieval chores. The underlying principle is that an SDR provides standardized support for user data organization at object granularity and direct access to persistent user data objects, rather than supporting user data organization only at "file" granularity and requiring the user to implement access to data objects accreted within those files.

This program was written by Scott Burleigh and Alan Schlutsmeyer of Caltech for **NASA's Jet Propulsion Laboratory**. *Further information is contained in a TSP [see page 1].*
NPO-19905

Automated Monitoring With Learned Envelope Functions

The Envelope Learning and Monitoring via Error Relaxation (ELMER) computer program automates the monitoring of time series of data from multiple sensors in a complex engineering system. The basic idea in automated monitoring is to trigger an alarm when the signal from any given sensor goes beyond allowable upper and lower limits; the problem is how to specify these limits. ELMER is designed to avoid the disadvantages of both (1) traditional monitoring with fixed limits, which tends to be too imprecise (to miss alarms) and (2) monitoring based on dynamical simulation of the system, which tends to be too expensive and too precise (to generate false alarms). Starting from traditional high and low limits, ELMER uses computational models of recurrent neural networks to "learn" global functional approximations for the upper and lower limits. For each sensor, these evolving limits are embodied in a pair of functions of time, collectively denoted an "envelope." As learning progresses with time, the limits become tighter; thus, in effect, ELMER makes a gradual transition from a mode of operation that resembles traditional fixed-limit monitoring toward a mode that looks more like a compromise between fixed-limit and simulation-based monitoring. The point of compromise — the balance between false alarms and the ability to detect malfunctions — is controlled parametrically. A graphical user interface enabler presents data from multiple time series on multiple time scales, as determined by the user. ELMER has been implemented on Sun Sparc computers running Solaris 2.X and could probably be ported to other UNIX systems running C++ and Java. Large color monitors and at least 32MB of random-access memory are recommended for the graphical user interface.

This program was written by Dennis DeCoste of Caltech for **NASA's Jet Propulsion Laboratory**. *Further information is contained in a TSP [see page 1].*
NPO-20025

Software for Operating on Image Data

The Imageclass computer software simplifies the development of image-processing applications by providing a uniform programmer's interface via an object-oriented class library. Written in the C++ programming language, Imageclass is designed to provide a high-level interface to image objects so that application programmers can efficiently implement complex image-processing operations without worrying about the low-level details. Most available image-processing libraries focus on computer graphics applications and are limited to a set of commercial industry file formats. Imageclass is oriented toward the scientific uses of images. Therefore, it is designed to provide a uniform interface for images that use science data types and science data formats such as CIPE, VICAR, and FITS. The library consists of a genus of

image subclasses, each of which handles a different pixel type, such as char, int, float, and the like. For each image subclass, member functions are provided for the essential image operations, such as creation, reading/writing to/from a file display through a spawned process, and element access. In addition a wealth of other basic operations, mathematical filters, statistical analysis, data type conversion, flipping, transposition, zooming, insertion, and subsetting are provided. The file I/O (input/output) interface supports reading from and writing to image files of several popular file formats used in the NASA community, including CIPE, FITS, VICAR, and raw data format. Imageclass can easily be extended to accommodate other file formats. With the Imageclass library, image-processing applications can be developed in a faster, cheaper, and better manner.

This work was done by Ansel Teng, Hillel S. Rom, Richard J. Weidner and Meemong Lee of Caltech for **NASA's Jet Propulsion Laboratory.** *Further information is contained in a TSP [see page 1].*
NPO-19888

BLANK PAGE

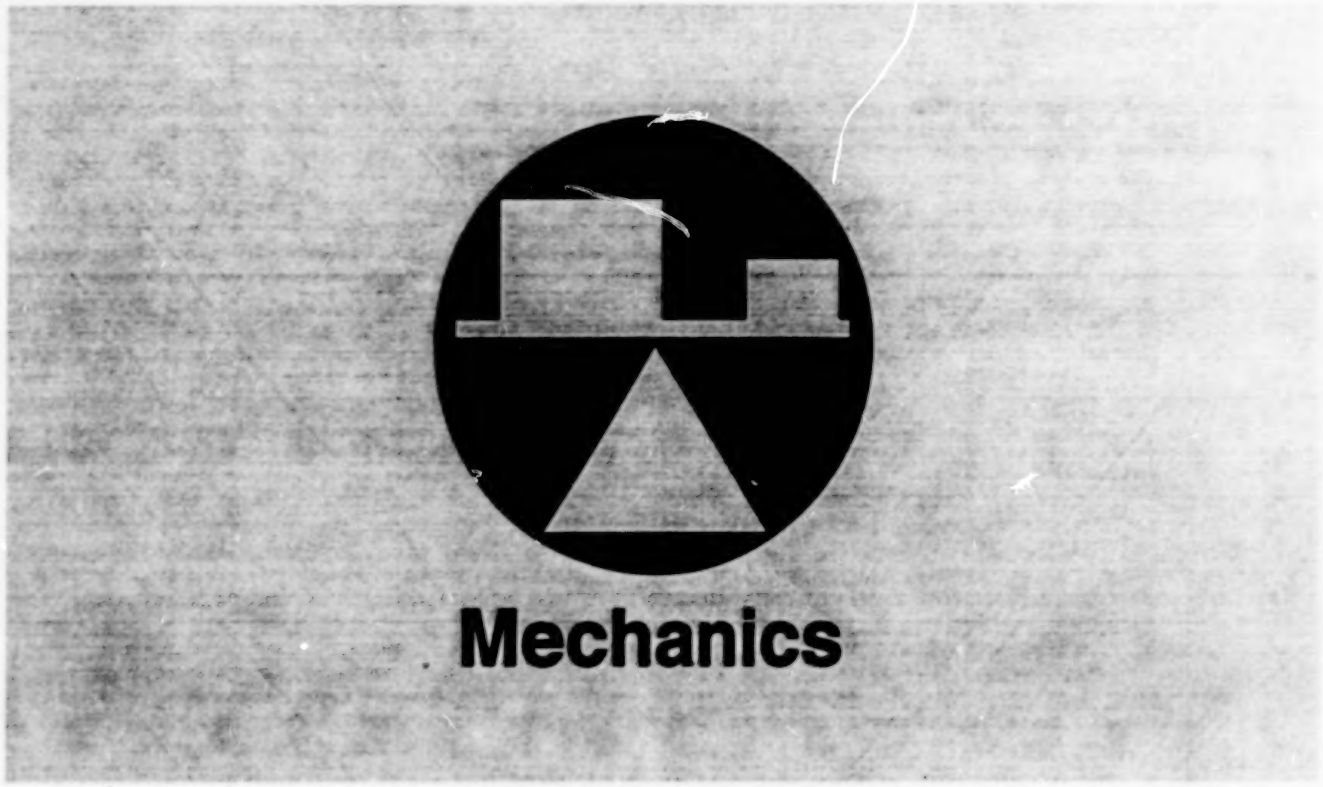

Hardware, Techniques, and Processes

45 Characterizing Worst-Case Flutter Margins From Flight Data
46 Software for Teaching Aerodynamics

BLANK PAGE

Characterizing Worst-Case Flutter Margins From Flight Data

A robust stability theory enables computation of flutter margins consistent with variations in flight data.

Dryden Flight Research Center, Edwards, California

Figure 1. The F/A-18 Systems Research Aircraft has been used in research on flutter margins.

A mathematical-modeling method for characterization of the flutter stability margins of an airplane has been formulated within the conceptual framework of a robust stability theory. The method was developed in a recent program to improve flight flutter testing on the F/A-18 Systems Research Aircraft (SRA) shown in Figure 1.

Some definitions of terms are prerequisite to an explanation of this development. "Flight envelope" denotes a range of velocities and altitudes within which it is considered to be safe and possible to operate an airplane. "Flutter stability margin" signifies a margin, defined with respect to a flight envelope, for avoiding flutter.

The development was prompted by the following considerations: Because of the danger posed by relying on inaccurate estimation of aeroelastic-stability properties, expansion of the flight envelope is costly and time-consuming. Mathematical models for preflight prediction and in-flight estimation must be accurate enough to represent the true stability margins.

In this method, the mathematical model of the airplane as an aeroelastic system comprises a nominal plant model generated as a structural model coupled with a linear state-space representation of unsteady aerodynamic forces, with associated uncertainty operators to represent modeling errors. The uncertainty operators admit variations in modal frequencies and damping parameters, nonlinearities, unmodeled dynamics. The robust stability margin is represented by a structured singular value called "μ."

Flight data are easily incorporated into the stability analysis in this method. Uncertainty operators are derived by modal validation to ensure that the dynamics observed in the data are represented in a robust mathematical model. The stability-margin parameter μ is robust to the measured variations associated with the uncertainty operators. In this sense, worst-case flutter margins are computed with respect to the flight data.

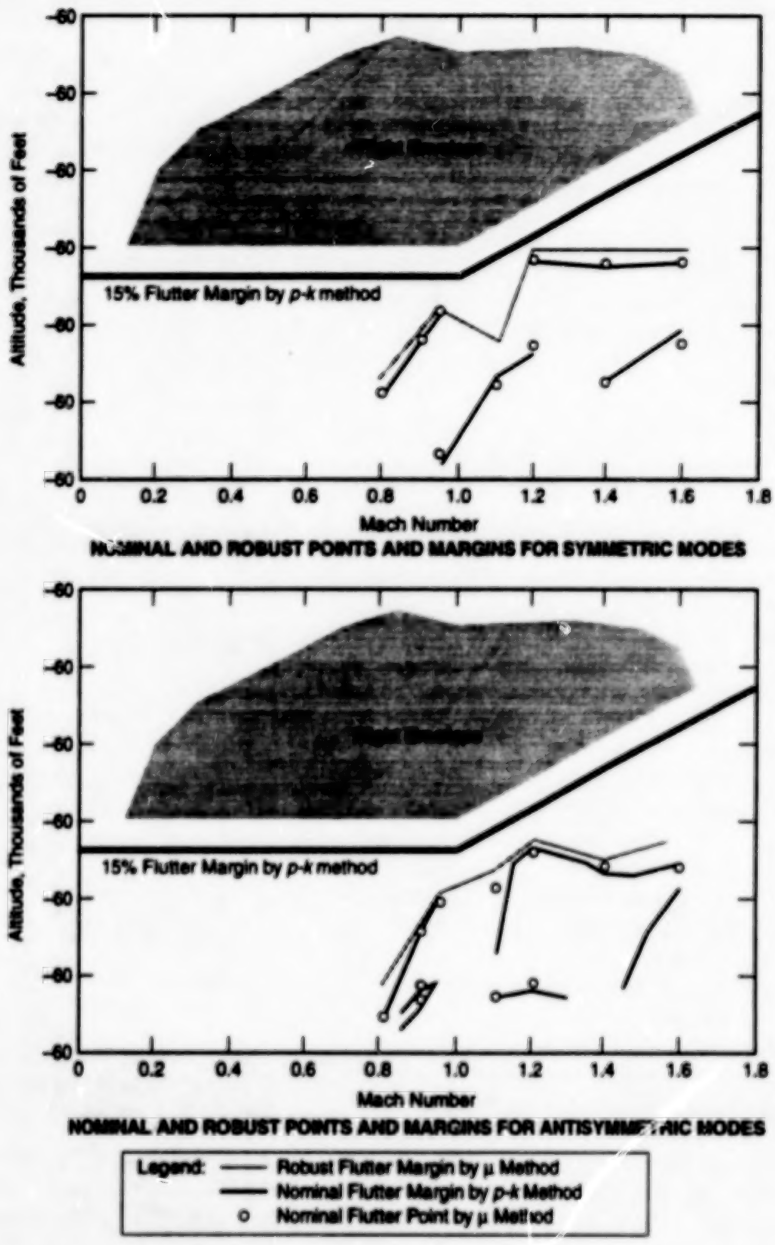
Altitude, Thousands of Feet
15% Flutter Margin by p-k method
Mach Number
NOMINAL AND ROBUST POINTS AND MARGINS FOR SYMMETRIC MODES
Altitude, Thousands of Feet
15% Flutter Margin by p-k method
Mach Number
NOMINAL AND ROBUST POINTS AND MARGINS FOR ANTISYMMETRIC MODES
Legend:
Robust Flutter Margin by μ Method
Nominal Flutter Margin by p-k Method
Nominal Flutter Point by μ Method

Figure 2. Flutter Margins were computed for symmetric and antisymmetric flutter modes by the μ-analysis method and by the traditional *p-k* method.

The worst-case flutter margins are computed for the F/A-18 SRA by use of aeroelastic-response data generated during operation of a wing-tip excitation apparatus, which includes a rotating aerodynamic vane on each wing tip to produce a modal vibration-excitation force. The frequency of rotation can be varied to obtain sine-sweep-response data. Symmetric and antisymmetric modes can be excited separately by use of in- or out-of-phase excitation, respectively, at the wing tips.

Flight data from 260 maneuvers throughout the flight envelope are used to generate uncertainty operators for a linear mathematical model with 28 structural vibrational modes. Figure 2 illustrates nominal and robust flutter margins computed with μ, along with flutter mar-

gins of a traditional type called "*p-k*," for symmetric and antisymmetric modes. The nominal margins as computed by both methods are similar, but the robust margins indicate that the flutter margins may lie closer to the flight envelope when modeling errors are taken into account.

This method offers significant advantages over traditional flutter-estimation methods. Analytical methods — for example, the one implemented by the *p-k* algorithm — rely on theoretical models to approximate the dynamics of aircraft without utilizing flight data. In-flight-estimation methods — for example, modal tracking — depend on noisy data and often produce unreliable stability estimates. The μ-analysis approach utilizes a well-developed theoretical model and realistic flight data to obtain accurate estimates of the stability properties of an aircraft.

This method may significantly decrease the cost and danger associated with flight testing for expansion of the flight envelope. A modal damping parameter of the type used heretofore for flutter estimation is merely a stability indicator (as distinguished from a stability predictor) and is truly informative only at a point of instability. On the other hand, μ is a stability predictor and can be updated throughout a flight test by revising the uncertainty operators on the basis of current measurement data and computing a new stability margin.

This work was done by Martin Brenner and Rick Lind of **Dryden Flight Research Center**. *Further information is contained in a TSP [see page 1].*
DRC-97-03

Software for Teaching Aerodynamics

Interactive graphical displays help students visualize results of flow calculations.

Lewis Research Center, Cleveland, Ohio

Six computer programs solve various aerodynamical problems, accepting inputs and presenting outputs via interactive graphical displays. These programs are designed to help undergraduate students visualize the results of their calculations and thereby gain deeper understanding of principles of aerodynamics. These programs can also be used in preliminary, approximate design analyses, enabling engineers to quickly explore the effects of variations in design parameters. Similar programs that mathematically model different phenomena could be used for similar purposes in other engineering and scientific disciplines.

These programs model classical flow phenomena as represented by simplified equations that can be solved rapidly enough for interactive analysis on modern computer workstations. As a student varies the geometry or flow conditions for a given flow problem, the new conditions are calculated immediately and the results presented to the student in graphical and numerical formats.

The programs and the problems they solve are the following:

- VU-TURBO performs design and off-design Brayton-cycle analysis for a turbojet engine with or without an afterburner, or for a two-spool turbofan engine.
- VU-FOIL uses a potential-flow model to compute flows around airfoils of various shapes.
- VU-SHOCKS computes supersonic flow past multiple wedges, producing graphical displays of the shock fronts that occur in such flows.
- VU-INLET computes supersonic flow through an external- or mixed-compression inlet.

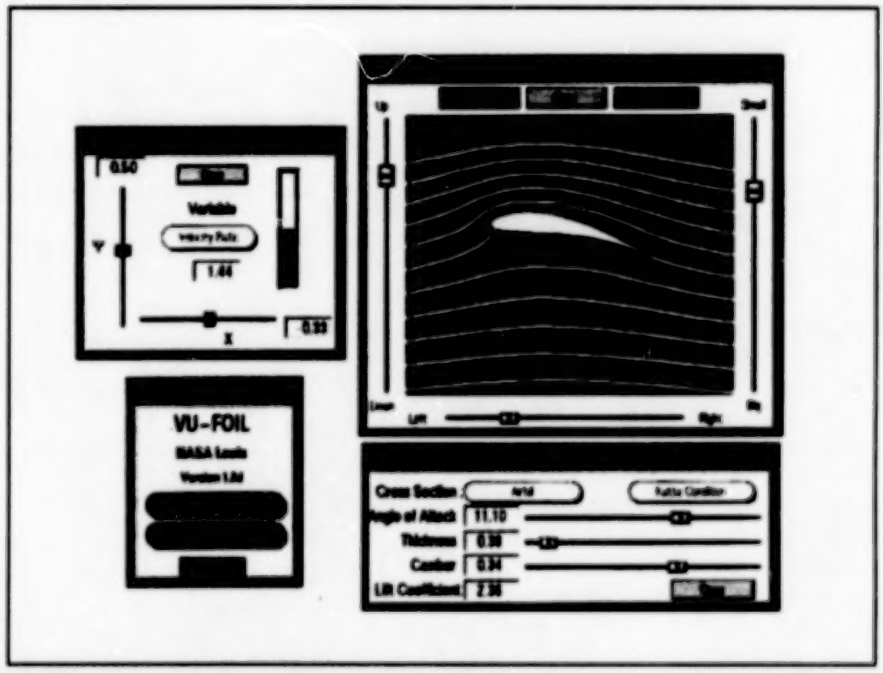

VU-FOIL Computes Flow Around an Airfoil, enabling the user to explore the effects of design parameters like thickness, camber, and angle of attack.

- VU-DUCT implements a one-dimensional model of incompressible, inviscid flow, based on simple conservation of mass and momentum, to compute the flow through an open- or closed-circuit wind tunnel.
- DUCTSIZER is used to design or study flows through multiply connected air-conditioning ducts.

The figure shows part of a typical VU-FOIL display. The student can change the shape and the angle of attack of the airfoil by use of the sliders in the lower right window. The streamlines in the upper right window are immediately updated to show the effects of these changes, and the lift coefficient is recalculated. The student can move a probe that samples the pressure and velocity; this amounts to doing a simulated wind-tunnel experiment in which probe measurements are taken at various locations to map the flow field. The student moves the probe by use of the sliders in the upper left window, the location of the probe is indicated by a red dot, which, in this case is located on the first streamline above the airfoil. The value of the flow variable being "measured" is indicated both numerically and graphically in the upper left window.

The programs have been tested on a variety of Unix computers, including SGI, IBM, HP, DEC, and Sun. They can also be executed on personal computers running Linux with an X graphics emulator. The programs can be run in either stand-alone

or client/server mode. Additional features of the programs include on-line help screens, optional printed output, restart capability, on-line references, and examination software tools.

This work was done by Thomas J. Benson of **Lewis Research Center** *and C. Fred Higgs III of Rensselaer Polytechnic Institute. Further information is contained in a TSP [see page 1].*

Inquiries concerning rights for the commercial use of this invention should be addressed to the Patent Counsel, Lewis Research Center [see page 1]. Refer to LEW-16298.

BLANK PAGE

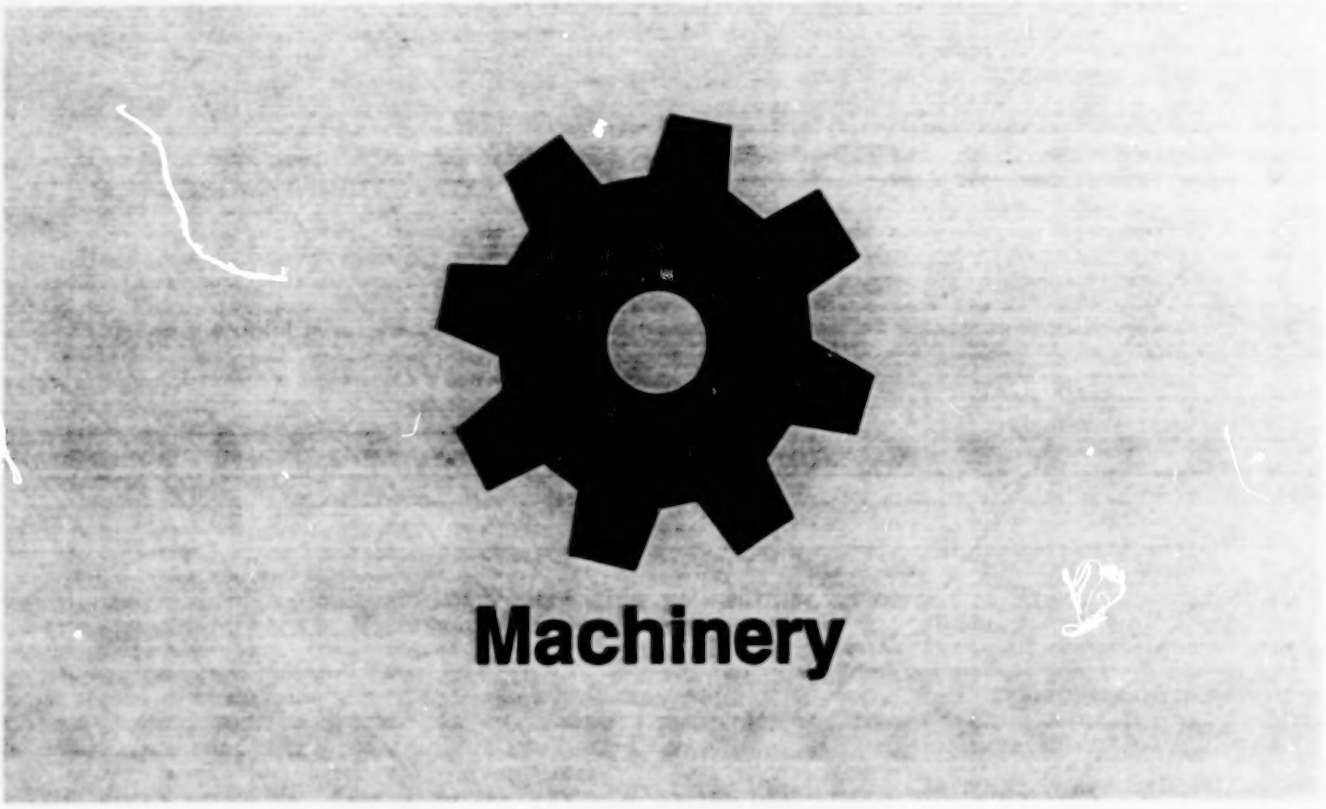

Machinery

Hardware, Techniques, and Processes

51 Piezoelectric Flexural-Traveling-Wave Pumps
52 Vacuum Four-Ball Tribometer for Testing Liquid Lubricants

BLANK PAGE

Piezoelectric Flexural-Traveling-Wave Pumps

Advantages would include small size, low power, and no sliding parts.

NASA's Jet Propulsion Laboratory, Pasadena, California

In miniature pumps of a proposed type, fluids and gases would be conveyed in a nearly frictionless manner in multiple shallow chambers formed by piezoelectrically actuated flexural traveling waves. These pumps could be useful in such applications as (1) injecting controlled small amounts of liquid medications and (2) sampling and vacuum pumping for miniature scientific instruments.

A basic piezoelectric flexural-traveling-wave pump, shown in the upper part of the figure, would include one or two stator plates with normally flat surfaces pressed together on the inside and with piezoelectric actuators attached on the outside. The flow path would be along the common contact surface of the plates. In the absence of piezoelectric actuation, the faying surfaces of the plates would remain flat and coincident with the common contact surface, so that there would be no gap between the plates and thus no flow. In other words, shutoff would occur automatically in the absence of piezoelectric actuation, and there would thus be no need for shutoff valves.

When suitably polarized and phased sinusoidal voltages are applied to the piezoelectric actuators, traveling flexural waves would be excited on the faying surfaces of the stator plates. The waves on both plates would be synchronized; this would cause the formation of shallow chambers sealed by contact between the stator plates at the crests of the waves. These chambers would capture small volumes of fluid and carry them along as the waves propagated along the plates from one end to the other. It would be desirable to drive the piezoelectric actuators at the frequency of resonance of the desired flexural-wave mode; doing so would maximize the wave amplitude, thus maximizing the depth of the wave-induced chambers and, in turn, maximize the volumetric pumping rate.

It would also be desirable to optimize the configuration of the piezoelectric actuators to maximize the wave amplitude. A practical design, illustrated in the lower part of the figure, would involve stacked piezoelectric actuators. In a typical case, chamber depths up to about 10 μm could be achieved. The pumping rate could be enhanced significantly by further optimization of design, including the choice of driving frequency (typically between 10 and 80 kHz) in conjunction with the other parameters.

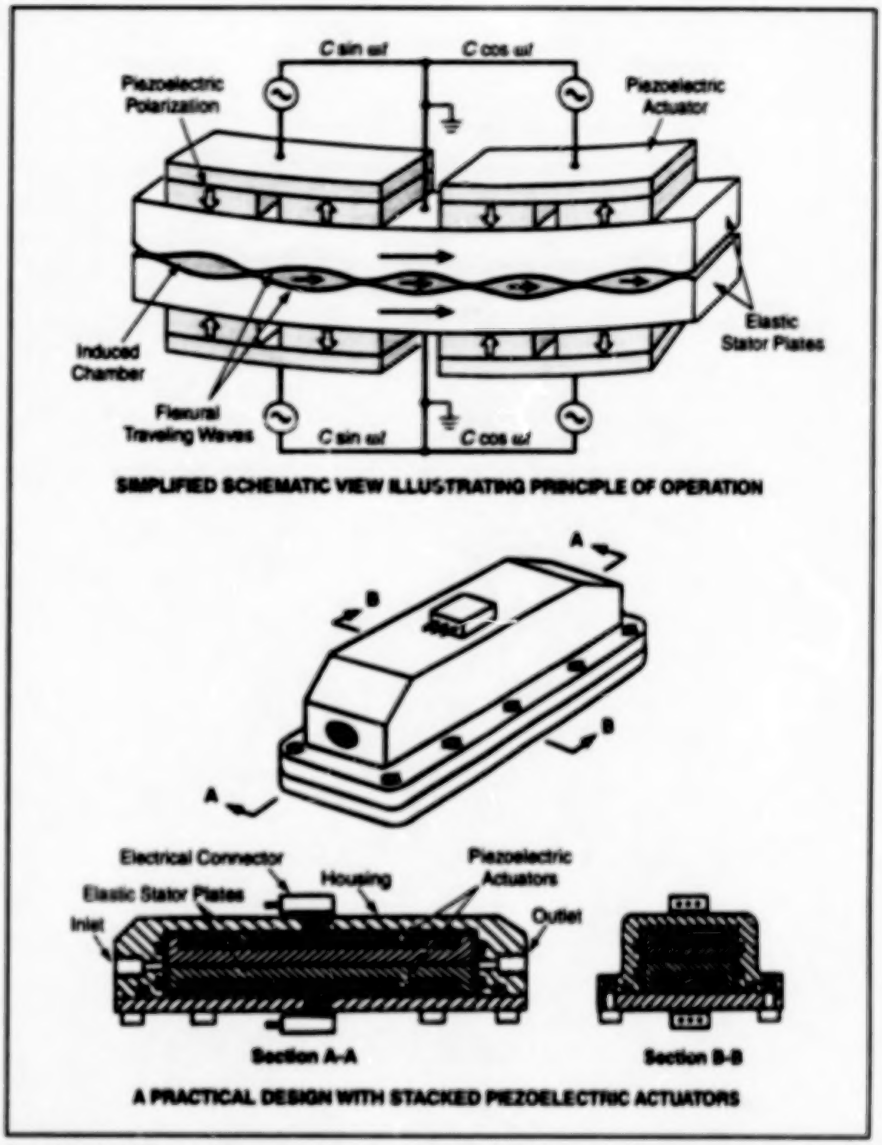

Synchronized Flexural Traveling Waves on the stator plates would form chambers that would convey fluid, effecting a pumping action reminiscent of peristalsis.

In addition to eliminating the need for valves, these pumps would offer the following advantages over other miniature pumps that are scaled-down versions of larger conventional pumps:

- Compactness;
- Low mass;
- Low power consumption;
- No sliding parts, with resultant low wear and high reliability;
- Simplicity of construction;
- Quiet operation.

This work was done by Yoseph Bar-Cohen, Benjamin Joffe, and Shyh-Shiuh Lih of Caltech for **NASA's Jet Propulsion Laboratory**. *Further information is contained in a TSP [see page 1].*

In accordance with Public Law 96-517, the contractor has elected to retain title to this invention. Inquiries concerning rights for its commercial use should be addressed to

Larry Gilbert, Director
Technology Transfer
California Institute of Technology
Mail Code 315 - 6
Pasadena, CA 91125
(818) 395-3288

Refer to NPO-19737, volume and number of this NASA Tech Briefs *issue, and the page number.*

Vacuum Four-Ball Tribometer for Testing Liquid Lubricants

This is a modified version of a standard four-ball tribometer.

Lewis Research Center, Cleveland, Ohio

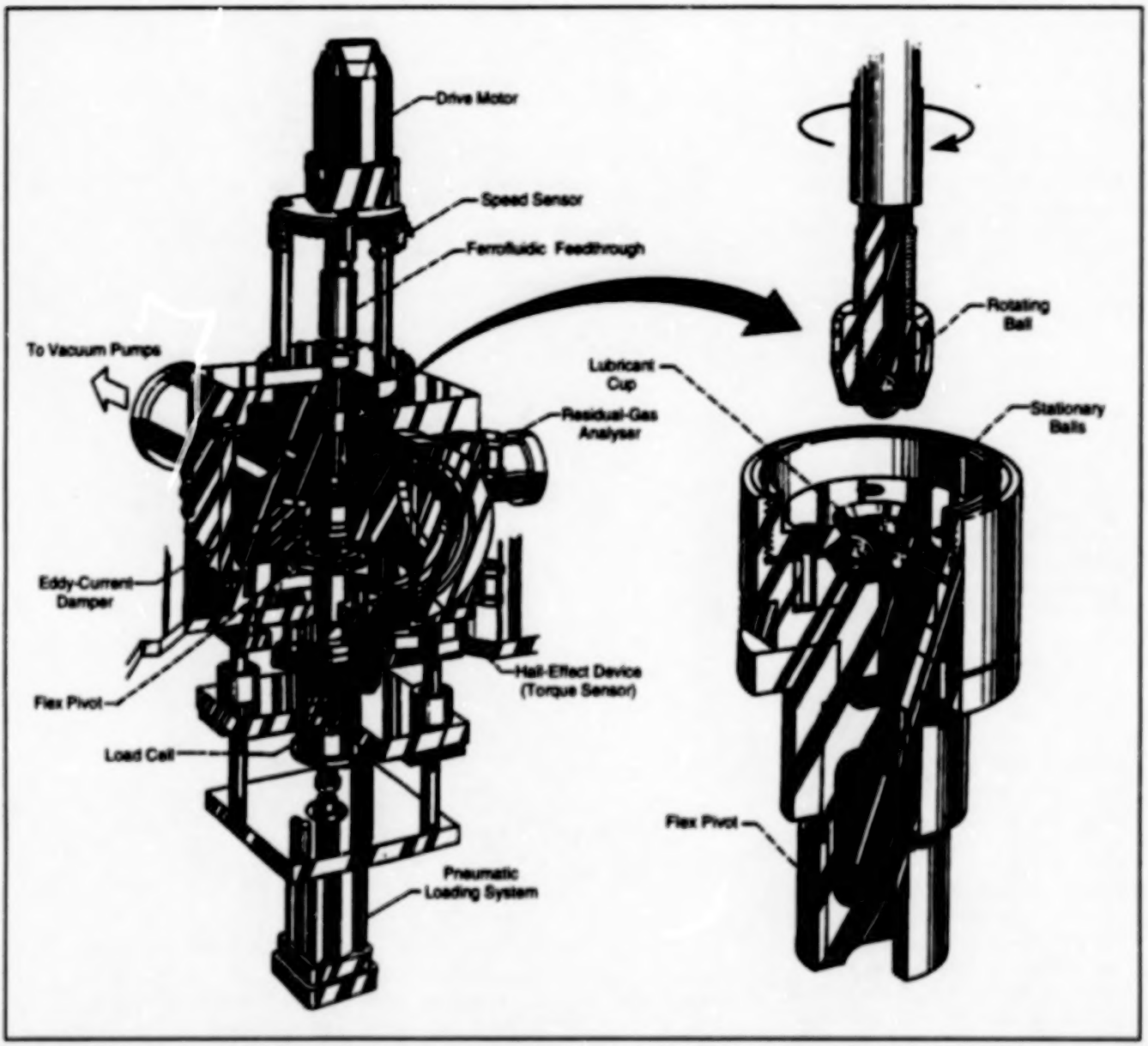

Figure 1. The Vacuum Four-Ball Tribometer features a ball configuration like that of a standard four-ball tribometer, but the balls and lubricant cup are mounted in a chamber that can be evacuated.

Figure 1 shows a four-ball vacuum tribometer for evaluating the performances of oils and greases as lubricants at room temperature. Tests can be conducted in air or nitrogen at atmospheric pressure, or in a vacuum.

The configuration of the balls is essentially the same as that of the four-ball tribometer of standard D 2783-88 of the American Society for Testing and Materials. The balls are precision bearing balls of AISI 440C stainless steel with a diameter of 0.375 in. (9.5 mm). The balls and associated components are contained in a chamber that can be evacuated by a turbomolecular pump (140 L/s) and a mechanical backing pump to achieve a vacuum with a residual pressure approximately in the range of 10^{-4} to 10^{-6} Pa. All vacuum-chamber flanges are of the knife-edge type and they are sealed by contact of the knife edges and copper gaskets, except for the chamber, which is equipped with a quick-access door sealed with an elastomeric O-ring. The vacuum chamber is equipped with a hot-filament ionization gauge for measuring pressure, plus a mass spectrometer for use as a residual-gas analyzer. Frictional torque is measured during the test, and wear patterns on the balls can be examined afterward.

The rotating upper ball is mounted on a spindle that is connected to an external motor drive via a ferrofluidic rotary feedthrough. The lower three balls are held stationary in a ball holder (lubricant cup) mounted on a stage, which can be moved vertically to press the lower three balls against the upper ball. In preparation for a test, the balls are immersed in and/or covered with the lubricant to be tested.

During a test, the lower three balls are pressed upward against the upper ball with a controlled force, and the lower balls remain stationary while the upper ball is made to rotate around its vertical axis and thus to rub against the lower balls. The speed of rotation can be set at a value between 10 and 500 r/min.

The vertical force and motion are generated outside the vacuum system by a pneumatic cylinder and transmitted to the stage via a linear-motion feedthrough sealed with a welded metallic bellows. A load cell outside the vacuum chamber measures the vertical force. The force can be set at a level between 50 and 1,032 N (11 to 232 lb).

The stage is connected to the linear-motion feedthrough via a "flex pivot," which is essentially a spring that is stiff against axial thrust, but allows some twist around the axis of the shaft. The angular deflection of the stage during a test is proportional to the frictional torque between the upper ball and the lower balls, characterized by a torsional spring stiffness of 48.6 N-m/radian (710 ft-lb/radian). Thus, the angular deflection is sensed by use of Hall-effect devices and a magnet to obtain a measure of the frictional torque. An eddy-current damper suppresses torsional oscillations that could distort the frictional-torque measurements; this damper includes a yoke and magnets affixed to the nonrotating end of the flex pivot and a copper plate that is affixed to the rotating end and that intrudes into the magnetic field.

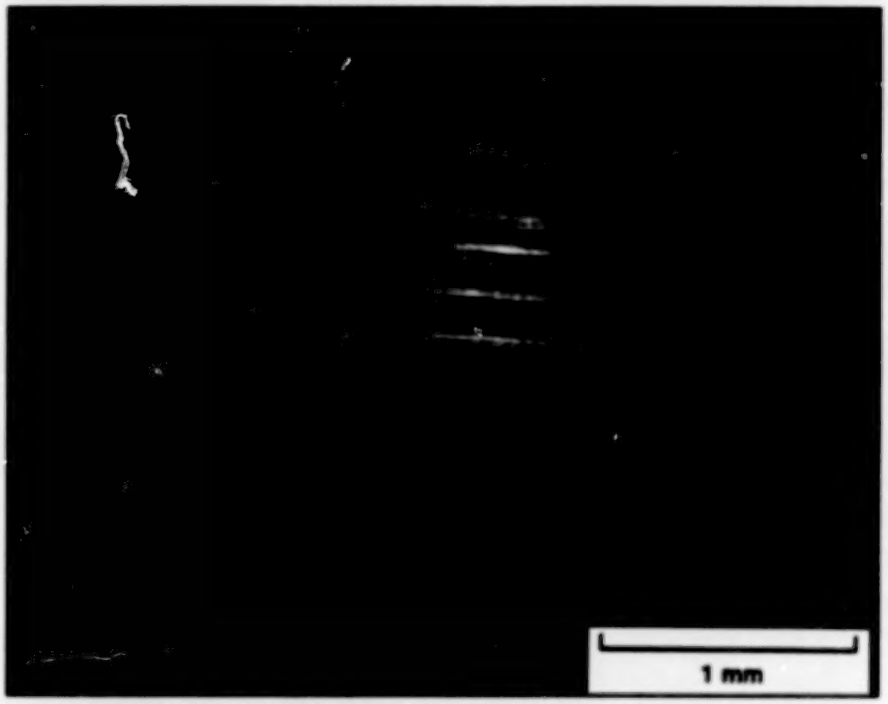

Figure 2. This Wear Scar on a Ball was produced in a vacuum with a perfluoropolyether lubricant at a load of 600 N, a speed of 100 r/min, and a sliding distance of 366 m.

Wear is determined by removing the cup from the chamber and measuring the diameters of wear scars (see Figure 2) on the three stationary balls by use of a microscope. A stage on the microscope is designed so that the diameters of the wear scars can be measured without removing the balls from the cup. If necessary, the experiment can then be resumed, using the same set of balls.

This work was done by William R. Jones, Jr., Ben Ebihara, and Stephen V. Pepper of **Lewis Research Center**; *Ralph Jansen of Ohio Aerospace Institute; Masaburni Masuko of the Tokyo Institute of Technology; and Larry S. Helmick of Cedarville College. Further information is contained in a TSP [see page 1].*

Inquiries concerning rights for the commercial use of this invention should be addressed to the Patent Counsel, Lewis Research Center [see page 1]. Refer to LEW-16194.

BLANK PAGE

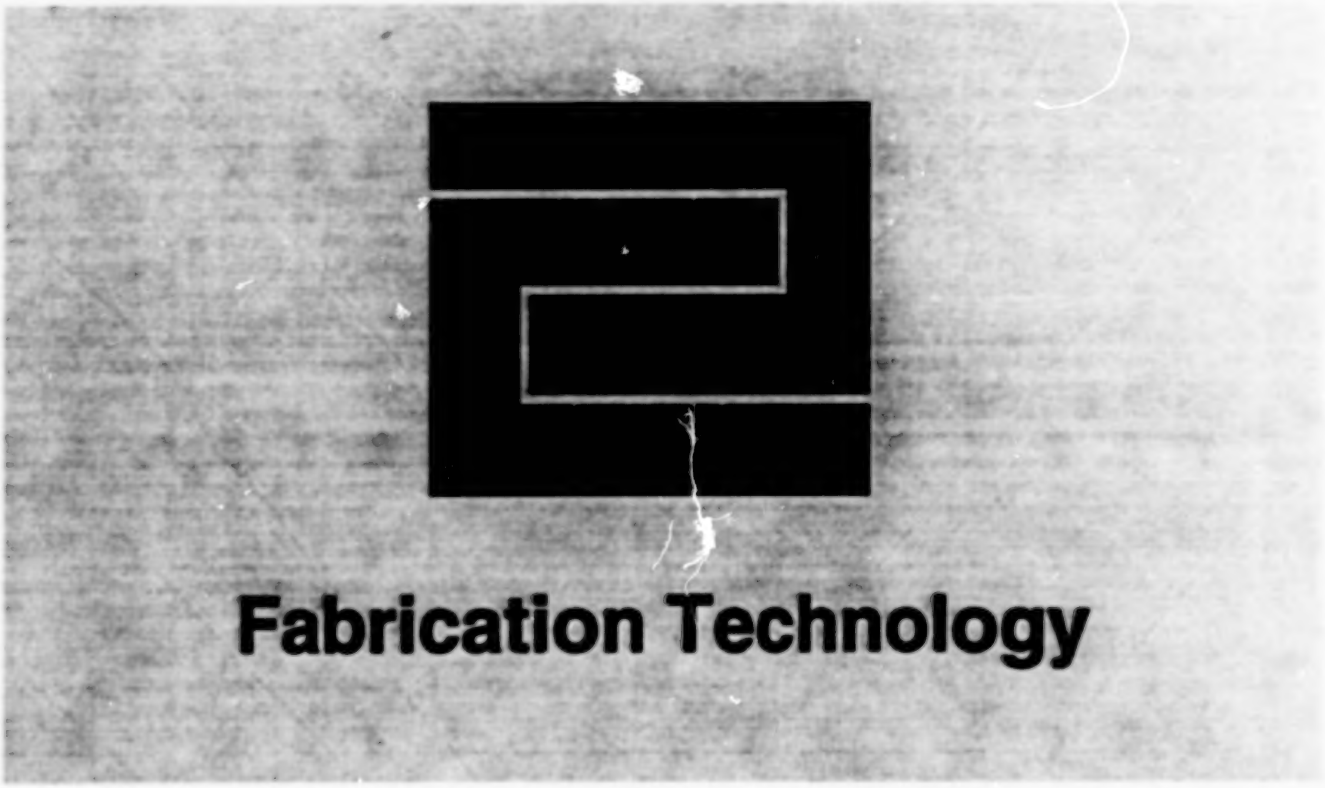

Fabrication Technology

Hardware, Techniques, and Processes

57 VPS Fabrication of Ceramic/Metal Furnace Cartridges
58 Making Structural Supports for Thinned CCD Membranes
58 Simpler Combustion Chamber, Nozzle, and Fabrication Process

BLANK PAGE

VPS Fabrication of Ceramic/Metal Furnace Cartridges

Ceramic and metal contents are graded to obtain desired properties.

Marshall Space Flight Center, Alabama

A vacuum plasma spray (VPS) process has been developed for making thin-walled ceramic/refractory metal composite furnace cartridges. These cartridges are used to contain and heat quartz ampoules that contain semiconductor materials for processing. The cartridges are required to resist chemical attack by the molten semiconductors in order to provide secondary containment should the quartz ampoules leak. The use of ceramic/refractory metal composites for this application makes it possible to utilize the corrosion resistance of the ceramics and the ductility and toughness of the metals, yielding robust cartridges that can withstand high temperatures and the stresses of fabrication and service.

In this process, a furnace cartridge is formed by VPS on a net-size-and-shape graphite mandrel, to which the deposited ceramic/metal composite material does not adhere. Upon cooling to ambient temperature after VPS, the mandrel shrinks at a greater rate than the deposited material due to its higher thermal coefficient of expansion, so that the deposit becomes the desired free-standing tube and can be slipped off the mandrel. Mandrels of this type were described in "Removable Mandrels for Vacuum-Plasma-Spray Forming" (MFS-30005), *NASA Tech Briefs*, Vol. 19, No. 5 (May 1995), page 82.

In this VPS process (see figure), refractory-metal and ceramic powders are injected into a gun that generates a plasma flame by ionization of gases in a dc arc. The plasma flame melts the powders and accelerates the molten materials, depositing them on the mandrel. The process includes the use of a controlled-powder-feeding technique that enables the formation of a deposit with a gradient of ceramic/metal composition to obtain a desired combination of thermal, mechanical, and chemical properties. For example, one experimental tube comprised an inner layer of ceramic, followed by a transition layer of half metal/half ceramic, followed by a layer of metal, followed by another metal/ceramic transition layer, followed by an outer ceramic layer.

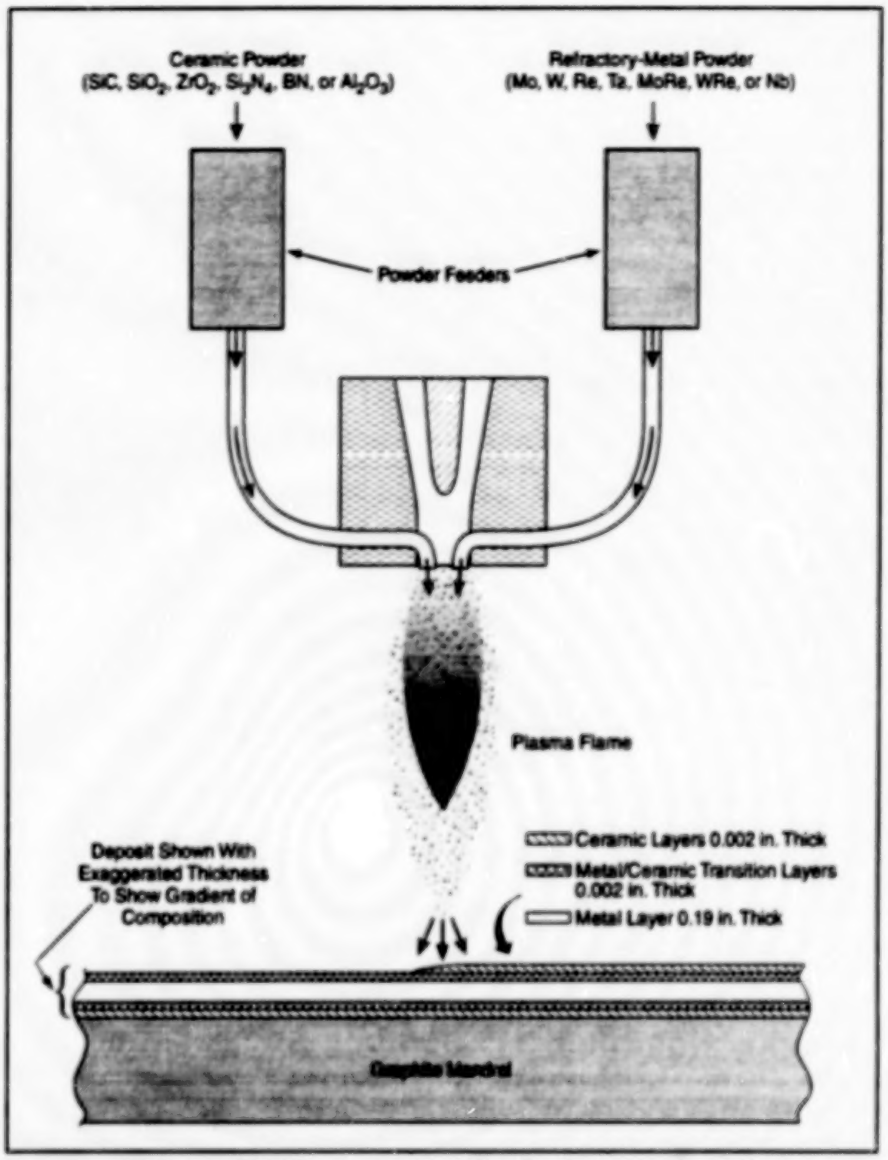
Ceramic Powder
(SiC, SiO_2, ZrO_2, Si_3N_4, BN, or Al_2O_3)
Refractory-Metal Powder
(Mo, W, Re, Ta, MoRe, WRe, or Nb)
Powder Feeders
Plasma Flame
Deposit Shown With Exaggerated Thickness To Show Gradient of Composition
Ceramic Layers 0.002 in. Thick
Metal/Ceramic Transition Layers 0.002 in. Thick
Metal Layer 0.19 in. Thick
Graphite Mandrel

Ceramic and Refractory-Metal Powders are injected into the plasma flame in variable proportions to deposit a graded-composition ceramic/metal composite on the mandrel.

The process also involves robotic manipulation of the VPS gun and the graphite mandrel; this makes it possible to complete the deposition of an entire furnace cartridge tube in one operation. Typically, as the VPS gun and mandrel are manipulated, the VPS gun is kept aimed perpendicularly to the surface of the mandrel to obtain the greatest density of deposition. Before deposition, the mandrel is preheated by operating the gun without the powder feed. Before and during deposition, the loss of heat from the mandrel is minimized by use of metal reflectors to reflect thermal radiation back into the mandrel.

This work was done by Philip D. Krotz, Douglas M. Todd, William M. Davis, Timothy N. McKechnie, Christopher A. Power, William H. Woodford, and Yoon K. Liaw of Rockwell International Corporation and Richard R. Holmes, Frank R. Zimmerman, and Richard M. Poorman for **Marshall Space Flight Center.** *Further information is contained in a TSP [see page 1].*

MFS-29998

Making Structural Supports for Thinned CCD Membranes

Structural supports would be added after high-temperature processing instead of before.

NASA's Jet Propulsion Laboratory, Pasadena, California

A technique for adding structural supports to membranes has been proposed. The technique is intended for use in fabricating charge-coupled devices (CCDs) and other microelectronic devices that are required to be very thin (7 to 15 μm in the case of some advanced CCDs) and to remain flat during use.

Heretofore, it was common practice to bond CCD substrates adhesively to structural supports by use of epoxies prior to thinning the substrates to final device thicknesses. This practice is unsuitable for fabrication of advanced CCDs because it is necessary to subject the substrates to postthinning processes at temperatures > 300 °C, at which epoxies disintegrate. Before applying the proposed technique, a CCD substrate would be thinned everywhere except at its perimeter, where a frame would be left to facilitate handling. The substrate would then be subjected to high-temperature processing. Being unsupported in the middle, the resulting CCD membrane could become wavy.

A small glass plate with many small, evenly spaced holes through its thickness would be prepared for use as the structural support. One face of the glass plate would be coated with an epoxy and placed in contact with the CCD membrane. The opposite face of the glass plate would be placed on a vacuum chuck (see figure). The suction in the chuck would act through the holes in the glass plate to flatten the membrane by drawing the membrane tightly against the plate. The suction would also draw excess epoxy through the holes. The plate and membrane could then be removed from the vacuum chuck because surface tension in the epoxy would continue to hold the membrane and plate together until they became permanently bonded together by curing of the epoxy.

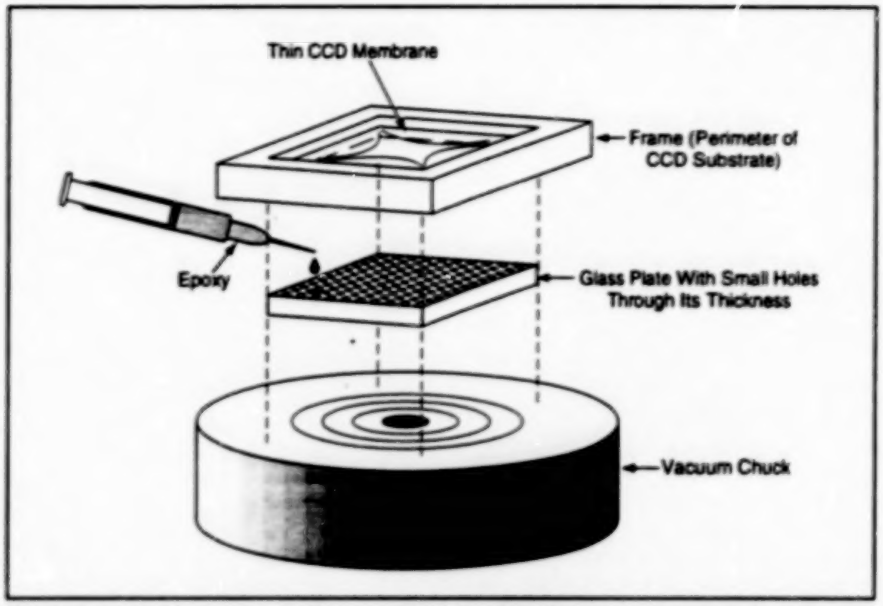

Wrinkles in the Membrane would be smoothed out when the membrane and glass plate were placed on the vacuum chuck. Excess epoxy would be drawn out by the vacuum chuck.

This work was done by Shouleh Nikzad and Michael E. Hoenk of Caltech for **NASA's Jet Propulsion Laboratory**. *Further information is contained in a TSP [see page 1].*
NPO-19655

Simpler Combustion Chamber, Nozzle, and Fabrication Process

An ablative insert would protect against excessive temperatures.

Marshall Space Flight Center, Alabama

A simplified design for the combustion chamber and nozzle of a rocket engine has been proposed to reduce the time and cost of fabrication. A conventional combustion-chamber/nozzle assembly of the type to be replaced operates with active cooling; for this purpose, it must contain integral cooling passages fed by manifolds. The fabrication of such a complex object in one integral piece involves processing of numerous piece parts through numerous steps of machining, plating, welding, and brazing, leading to long fabrication time and high cost. The proposed combustion-chamber/nozzle assembly would not be actively cooled, so that there would be no need for cooling passages, and fabrication would be simplified and accelerated accordingly.

The proposed combustion chamber and nozzle (see figure) would include a shell of refractory metal (e.g., a niobium-based alloy). An integral flange would be formed at the upper end of the shell. To provide some thermal protection and a barrier against oxidation, the inner surface of the shell would be coated with aluminum oxide or other suitable material. In the combustion-chamber region, the shell would be further lined with an ablative silica phenolic insert. During operation, resins would boil off from the phenolic, leaving behind a char layer that would, along with an remaining phenolic, protect the refractory-metal shell against overheating. The thickness of the insert would be chosen so that the char would not penetrate too deeply during the design operating life. Inasmuch as the operating temperature would decrease toward the exit (lower) end of the nozzle, the thickness of the insert would be made to taper down to the point where the coated refractory metal could survive without further protection.

The shell would be fabricated by vacuum plasma spraying (VPS) on a graphite mandrel. Optionally one could first apply the aluminum oxide or other thermal/oxidation-barrier layer to the mandrel by either a traditional coating technique or VPS. If this option were selected, then VPS would be started — initially with the thermal/oxidation-barrier material, then

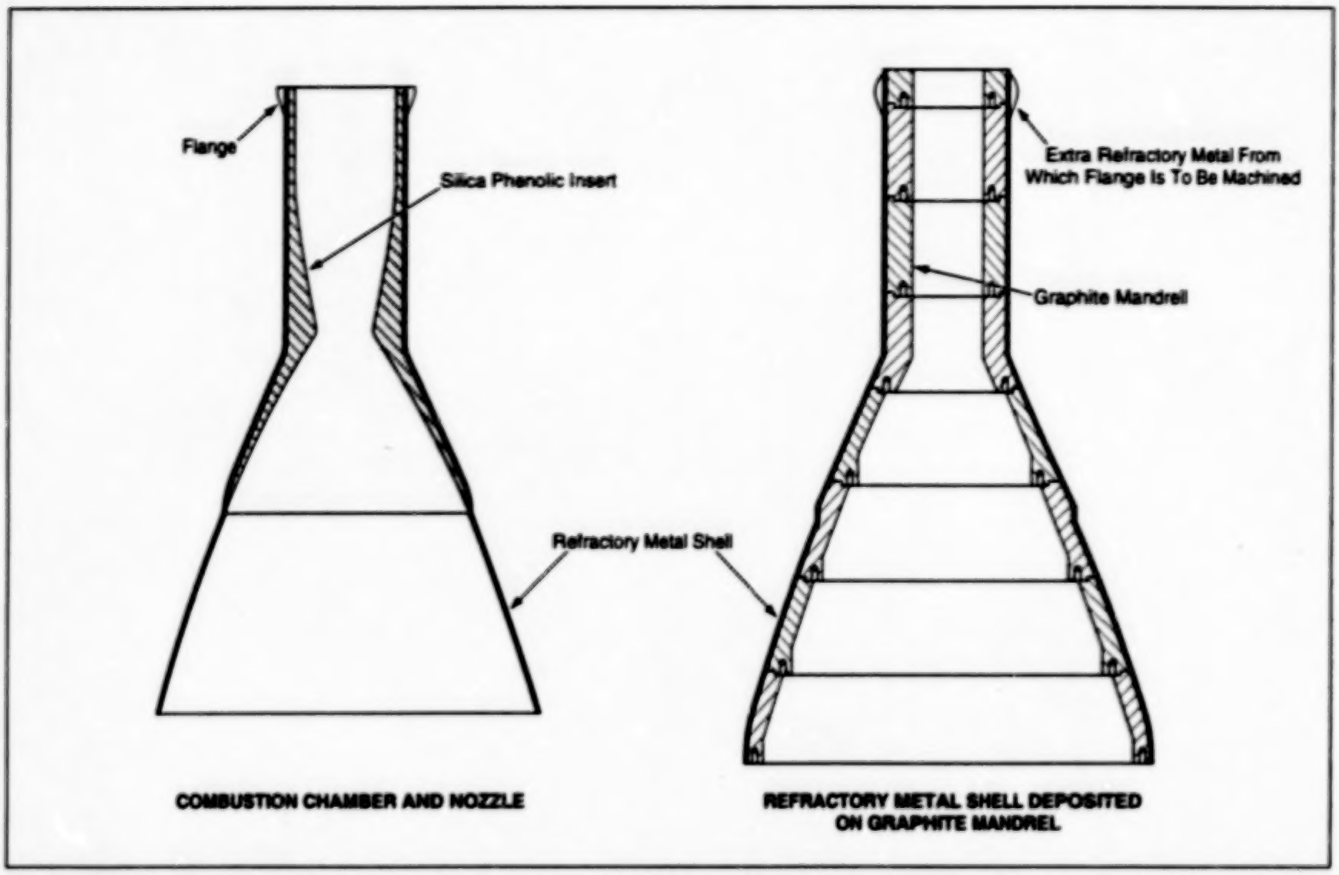
Flange
Silica Phenolic Insert
Refractory Metal Shell
Extra Refractory Metal From Which Flange Is To Be Machined
Graphite Mandrel
COMBUSTION CHAMBER AND NOZZLE
REFRACTORY METAL SHELL DEPOSITED ON GRAPHITE MANDREL

The Combustion Chamber and Nozzle would be made in only two pieces: a refractory metal shell with a silica phenolic insert bonded inside.

making a gradual transition to the refractory alloy, then continuing with the alloy to obtain the required thickness. The other option would be to deposit only the alloy by VPS, then coat the inner surface of the shell with a silicide after completion of deposition and removal of the shell from the mandrel. The alloy would be deposited to extra thickness at the upper end; the thickened upper end would then be machined to make the flange. Because of a large difference between the coefficients of thermal expansion of graphite and the refractory alloy, the shell could be easily removed from the mandrel once it had cooled from the VPS temperature.

The ablative insert would be made from silica phenolic tape wrapped on a steel mandrel, which would be configured to obtain approximately the contour of the interior of the combustion chamber. While still on the mandrel, the wrapped tape would be cured, then machined to make an insert to match precisely the contour of the combustion chamber. The insert would then be removed from the mandrel and bonded into the combustion chamber.

This work was done by Charles S. Cornelius and W. Neill Myers of **Marshall Space Flight Center**. *Further information is contained in a TSP [see page 1].*
MFS-31148

BLANK PAGE

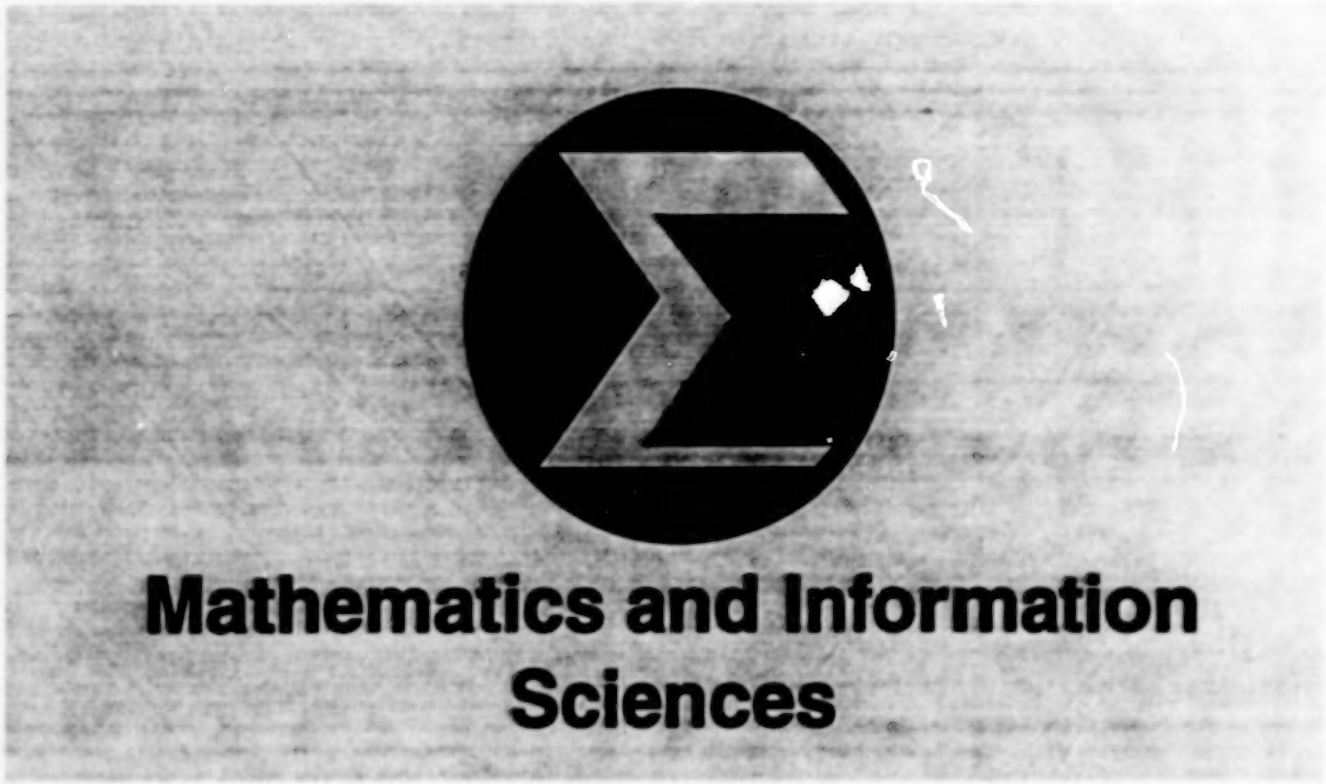

Mathematics and Information Sciences

Hardware, Techniques, and Processes

63 Multivariable State-Space Identification in Various Operators

64 Parallel Multigrid Algorithms and Code for Computations of Incompressible Flows

BLANK PAGE

Multivariable State-Space Identification in Various Operators

Operators can include z, δ, and s.

NASA's Jet Propulsion Laboratory, Pasadena, California

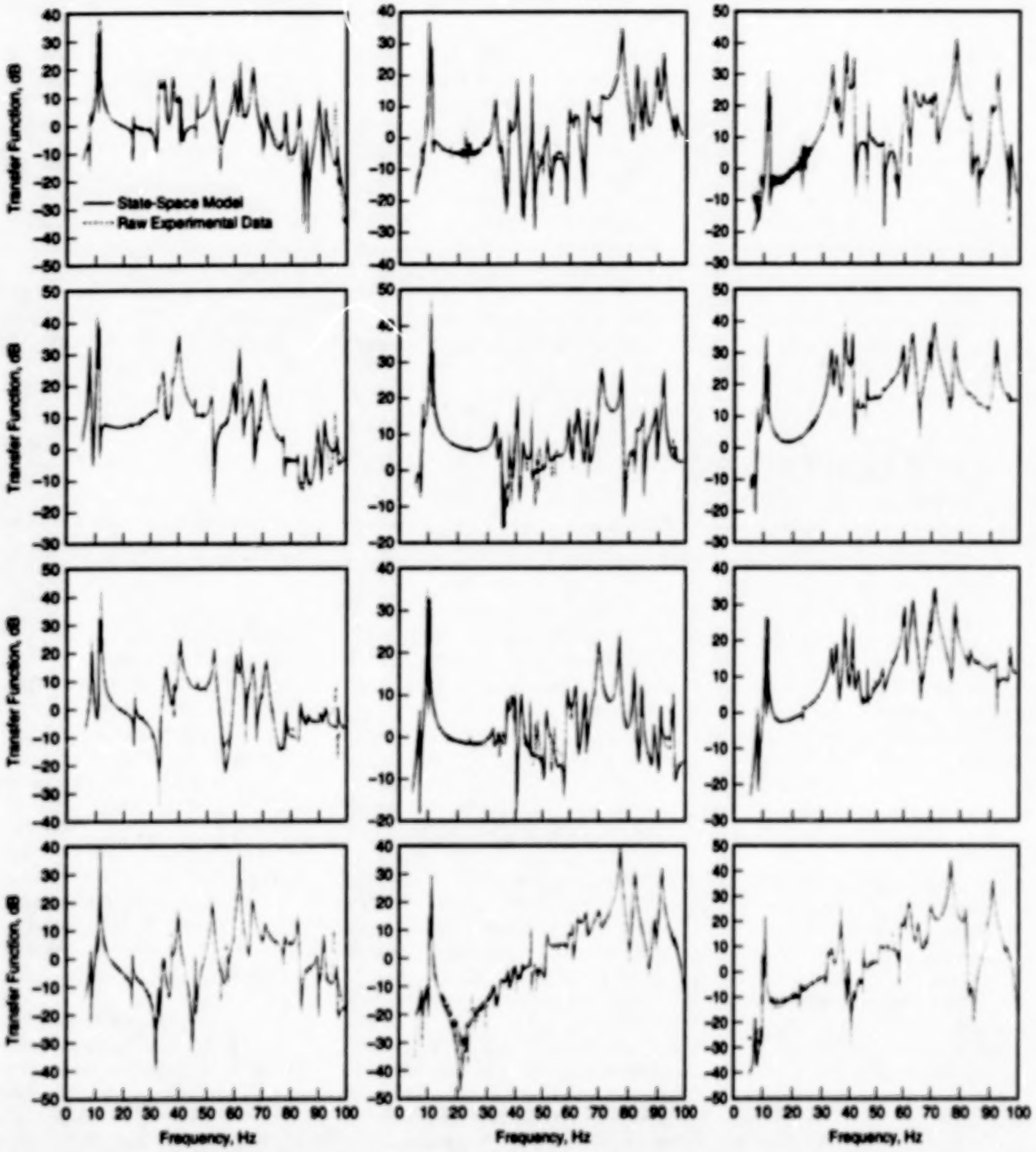

These Frequency-Domain Transfer Functions for 4 inputs and 3 outputs illustrate the ability of the extended SSFD algorithm to estimate the parameters of a mathematical model of complex dynamics.

An algorithm for estimating the parameters of state-space mathematical models of systems with complex dynamics, multiple inputs, and multiple outputs has been developed. For example, the system to be modeled may be a complex, flexible structure instrumented with actuators and sensors; the data needed for modeling are obtained by exciting the structure at each of several different actuator locations (multiple inputs) and measuring the responses at several sensor locations (multiple outputs). The present algorithm is an extended version of the State Space from Frequency Data (SSFD) algorithm, which was developed for use in modeling such systems. The present algorithm provides for modeling in any operator of interest

and is particularly suitable for the shift operator (the variable z of the z-transform), the delta operator [$\delta = (z-1)/T$], (where T is the sampling period) or the Laplace-transform complex-frequency operator (s).

State-space models are needed for designing control systems for dynamic systems; e.g., control systems to suppress vibrations in structures. It has been found that realization algorithms based on Markov parameters can help solve this state-space system-identification problem. In the past, these algorithms were developed primarily in the time domain. However, in many applications, the available data are in the frequency domain so that one must compute the Markov parameters from frequency-domain data. At this point, windowing distortions are often introduced. For example, an inverse discrete Fourier transform of the frequency data provides an estimate of the Markov parameter sequence distorted by time-aliasing effects.

The SSFD algorithm is comprised of a sequence of steps involving complex curve fitting, sparse-matrix singular-value decomposition, and balanced realization based on Hankel singular values. The SSFD algorithm estimates state-space models for systems with complex (high-order) dynamics, multiple inputs, multiple outputs, and large numbers of unknown parameters, and is not subject to windowing distortions. The basic idea is to generate Markov parameters indirectly from a transfer function that has been curve-fitted to frequency-domain data.

An important aspect of the SSFD algorithm is its use of overparameterization. It has been proven that the extra dynamics introduced by overparameterizing in the shift operator are stable, while the extra dynamics introduced by overparameterizing in the Laplace-transform complex-frequency and delta operators are generically unstable. This leads to modifications of the Laplace and delta operators to ensure stability under overparameterization.

The extended version of the SSFD algorithm has been verified by use of data from 4-input/3-output vibration experiments on the JPL Advanced Reconfigurable Control Testbed — a towerlike flexible-truss structure with vibration sensors and actuators. The algorithm performed complex curve fitting on the input and output data and estimated 780 parameters in the fitted transfer functions (see figure). Markov parameters were estimated from the transfer functions, leading to a reduced multivariable state-space model with 100 states accurate over a frequency range of 100 Hz.

This work was done by David S. Bayard of Caltech for **NASA's Jet Propulsion Laboratory**. *Further information is contained in a TSP [see page 1].*
NPO-19168

Parallel Multigrid Algorithms and Code for Computations of Incompressible Flows

These algorithms are suitable for simulations of complex incompressible flows; the parallel code scales well on massively parallel processors.

NASA's Jet Propulsion Laboratory, Pasadena, California

A parallel numerical algorithm for solving incompressible Navier-Stokes equations on two-dimensional (2D) and three-dimensional (3D) finite-difference grids and a parallel multigrid algorithm for solving general elliptic partial differential equations (PDEs) have been developed, implemented, and tested. Numerical experiments show that the algorithms are physically robust, numerically stable, and computationally efficient. The parallel solver package developed is highly modular; it can either be used as a stand-alone flow solver or be used as a template that can be modified or extended to solving a variety of physics and engineering flow problems; the elliptic kernel in the solver package can be used to solve elliptic equations on vertex-centered, cell-centered, and staggered grids.

The numerical Navier-Stokes algorithm used here is a second-order projection method applied to a staggered grid. Projection method is a type of operator-splitting method in which one solves the differential equations of the pressure and the velocity fields separately in an iterative procedure. At each time step, the momentum equations are solved first for an intermediate velocity field without the knowledge of the correct pressure field, and therefore no incompressibility condition is enforced. The intermediate velocity field is then corrected in a "projection" step in which one solves a pressure equation with properly derived boundary conditions and then uses the computed pressure to produce a divergence-free velocity field. The computation kernel used for computing intermediate velocity and pressure fields is a parallel multigrid solver based on "V-cycle" and "full-V-cycle" schemes. Multigrid schemes are a class of highly efficient iterative algorithms in which a set of hierarchical fine and coarse computational grids is used to compute a solution on the finest computational grid, a detailed description of which lies beyond the scope of this article. Briefly, V-cycle scheme performs solution relaxation, residual restriction, and solution correction in a recursive fashion on fine and coarse grids, while full-V-cycle scheme is a generalization to the V-cycle scheme with a higher convergence rate. These multigrid schemes are optimal in solving elliptic problems in that the numerical solution can be obtained in a time proportional to the number of unknowns on the finest computational grid.

The overall approach for the parallel implementation is a domain-decomposition strategy in which the computational (finest) grid is partitioned into multiple rectangular subgrids, each subgrid and its derived coarse grids being assigned to a processor in a logically rectangular processor array (see figure). Values at grid points lying on "partition boundary layers" (the thicknesses of which are usually dictated by the specific numerical schemes used) are exchanged among neighboring processors in the form of "messages" to ensure a correct implementation of the corresponding sequential numerical algorithms on the global computational grid. To deal with coarse grid processing in multigrid schemes, a set of (logically) hierarchical coarse processor arrays are constructed in a preprocessing step of the code.

The 2D and 3D parallel solver codes can readily be scaled to a large number of processors on the Intel Paragon and Cray T3D parallel processors for problems with moderate granularity. Several message-passing protocols (MPI, PVM, and Intel NX) have been coded into the solver package to make the code portable to systems that support one or more of these protocols for interprocessor communications. The flow solver was tested for both numerical and parallel performances on a few model problems. Numerical experiments include a driven-cavity flow at Reynolds numbers of 5,000, 10^5, and

10^6, and a doubly-periodic inviscid-shear flow. Parallel performances were measured, on a JPL 256-node Cray T3D system and a Caltech 512-node Intel Paragon system, in terms of speed-up in which the code was run on a different number of processors for a fixed global grid size, and scaling in which the code was run on a different number of processors for a fixed local subgrid size in each processor.

This work was done by John Z. Lou of Caltech for **NASA's Jet Propulsion Laboratory**. *Further information is contained in a TSP [see page 1].*

NPO-19593

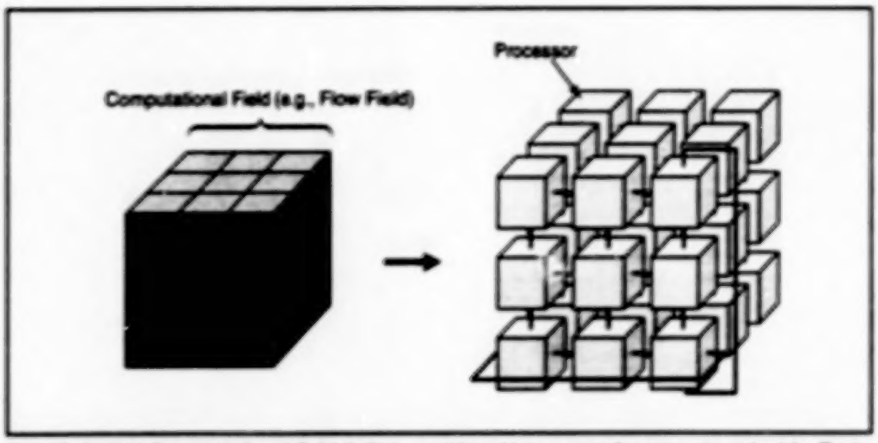

The 3D Global Computational Grid (left) is partitioned into a set of rectangular subgrids. Each subgrid is assigned to a processor in a 3D processor array (right).

BLANK PAGE

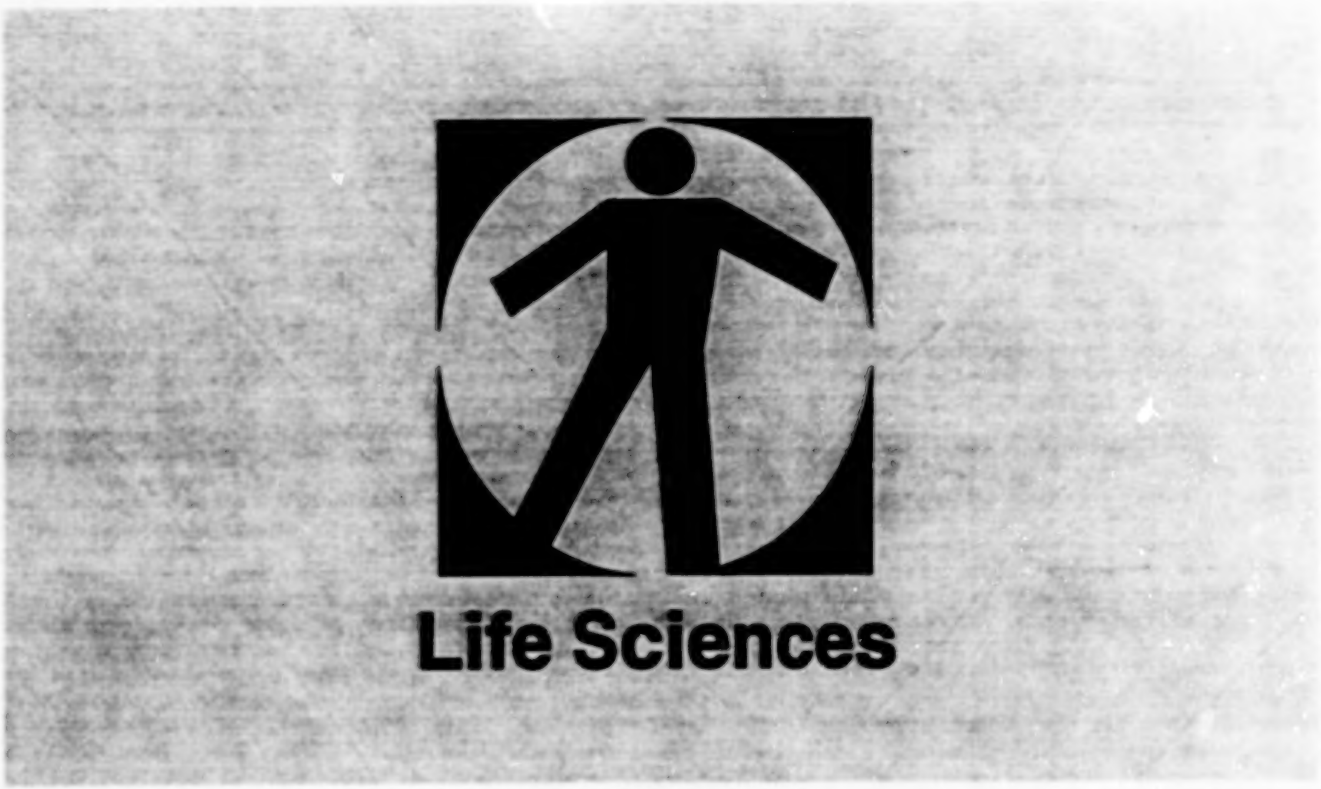

Hardware, Techniques, and Processes

69 Advanced Semicontainerless Crystallization of Proteins
69 Ring Method for Crystallization of Proteins
70 Crystallizing Proteins in Thin Wafers

BLANK PAGE

Advanced Semicontainerless Crystallization of Proteins

Crystals are formed suspended in liquids.

Marshall Space Flight Center, Alabama

Advanced methods for the semicontainerless growth of protein crystals are undergoing development. Each method involves dynamic manipulation, to various degrees, of one or more of the many parameters and conditions that affect the rates of growth, the quantities, and the types and degrees of imperfection of the crystals. These parameters and conditions include geometry, temperature, humidity, salinity, pH, concentrations of proteins in solutions, and concentrations of such other substances as solvents and precipitating agents.

"Semicontainerless," as used here, signifies that the crystals are not formed in contact with solid supports; instead, the crystals are made to grow suspended in liquids. The basic idea is to isolate each growing crystal from the adverse effects that would otherwise be exerted on its crystalline structure by a solid surface and by other, differently oriented growing crystals that would form on that surface. Of course, a liquid suspension environment can also affect a growing crystalline structure adversely, but the development of semicontainerless growth is motivated by the expectation that in many if not most cases, one could obtain crystals that are larger and more nearly perfect than are those grown by older techniques on solid supports.

One older method for semicontainerless growth of protein crystals is the hanging-drop method, which has been described previously in *NASA Tech Briefs*. More recently, four advanced methods have been investigated. These methods involve

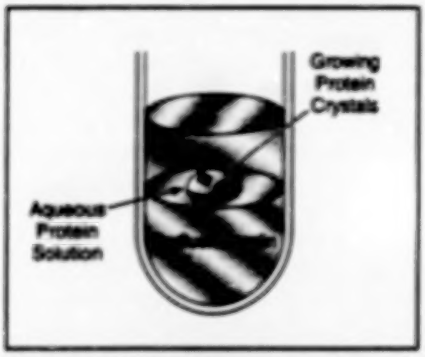

The Layer-Stacking Method is one of four advanced methods of semicontainerless growth of protein crystals. The crystals precipitate from the protein solution as water evaporates, driving the solution to supersaturation. The oil layer retards evaporation to a required low rate.

(1) stacking of layers of immiscible fluids, (2) gels under oil, (3) emulsions, and (4) lattices of bubbles.

In the layer-stacking method, one uses three or more immiscible fluids of different mass densities. In the simplest version of this method, a drop of an aqueous solution that contains the protein to be crystallized is placed on top of a denser liquid (e.g., perfluorodecalin), and an oil or other less dense liquid is placed on top (see figure). Together, the bottom and top layers suspend the protein solution in isolation from solid supports, and the top layer retards evaporation from the protein solution, as is necessary to ensure crystal growth at the optimum rate.

In the gel-under-oil method, the protein solution is contained within a gel, which is covered with an oil to retard evaporation. Growth takes place in the gel, which is used to prevent both undesired buoyant mixing (convection) of the protein solution and undesired sedimentation of crystals through the solution.

The present emulsion method differs from an older emulsion method that involved crystallization of protein in isolated drops, followed by coalescence of the growing crystals. In the present emulsion method, the protein solution is the continuous phase, and growth takes place as though in a loose gel; the discontinuous emulsified phases cushion growing crystals against sedimentation and suppress convection.

In the bubble-lattice method, bubbles are formed by blowing air through a protein solution, then the bubbles are formed into a nearly two-dimensional lattice between two microscope slides. Crystals grow on the faces of the bubbles as evaporation into the interiors of the bubbles drives the faces of the bubbles toward supersaturation, while capillarity supplies the growing crystals with more protein.

This work was done by David A. Noever of **Marshall Space Flight Center.** *Further information is contained in a TSP [see page 1].*

Inquiries concerning rights for the commercial use of this invention should be addressed to the Patent Counsel, Marshall Space Flight Center [see page 1]. Refer to MFS-31046.

Ring Method for Crystallization of Proteins

Rings provide additional control over crystallization conditions.

Marshall Space Flight Center, Alabama

The ring method of crystallization of proteins involves the use of wire rings to shape drops of protein solutions and/or position those drops with respect to adjacent and surrounding liquids. The ring method can serve as an alternative to the methods described in the preceding article "Advanced Semicontainerless Crystallization of Proteins" (MFS-31046). Rings can be added to protein-crystal-growth apparatuses along with position sensors, position actuators, and position-control circuitry to provide additional degrees of freedom for control of crystallization conditions and thereby afford additional opportunities to optimize crystallization processes to obtain larger, higher-quality protein crystals for use in biomedical and pharmaceutical research.

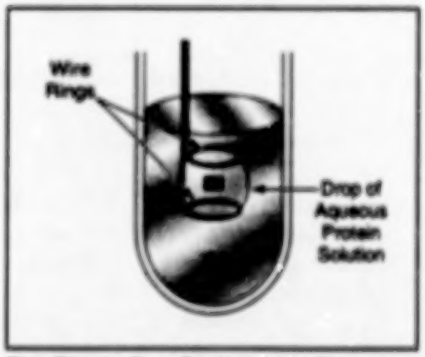

The Rings Can Be Used to Flatten or Lengthen the drop of protein solution, and/or to make the drop protrude partly above the top of the oil.

Four versions of the ring method have been tested thus far in experiments on growing crystals of hen egg-white lysozyme. In the first version, a drop of protein solution rests on an appropriately sized single ring in air, so that water can evaporate through the nearly spherical surface of the drop. The evaporation increases the concentration of the protein, eventually resulting in supersaturation and crystallization of protein. The drop can be monitored visual-

ly to observe the crystal(s) forming within it.

In the second version, a drop of protein solution is held between two rings (see figure) in air or in oil. The axial distance between the rings can be increased or decreased to lengthen or flatten the drop.

In the third version, a drop of protein rests on a single ring in a container of oil. The ring can be raised or lowered to control the position of the drop with respect to the top surface of the oil. Typically, the height is set so that the drop protrudes by a small, controlled amount, providing a small, controlled area for evaporation of water from the drop.

In the fourth version, as in the third version, a drop of protein solution rests on a single ring in a container, but in this case, the drop is positioned at an interface between two liquids that include solvents that are immiscible with each other and with the water of the aqueous protein solution. These liquids can be chosen, for example, to contain solutes (e.g., salts and precipitating agents) that are to be transported to the protein solution.

Other versions of the method have been proposed. For example, rings could be made in noncircular shapes to obtain different evaporative conditions. Alternately, combinations of three or more rings could be used to suspend multiple adjacent drops and to control flows of solutes among drops by exploiting such effects as surface tension and gradients of salinity.

This work was done by David A. Noever of **Marshall Space Flight Center**. *Further information is contained in a TSP [see page 1].*

Inquiries concerning rights for the commercial use of this invention should be addressed to the Patent Counsel, Marshall Space Flight Center [see page 1]. Refer to MFS-31047.

Crystallizing Proteins in Thin Wafers

Crystals are grown in thin gaps between parallel flat plates.

Marshall Space Flight Center, Alabama

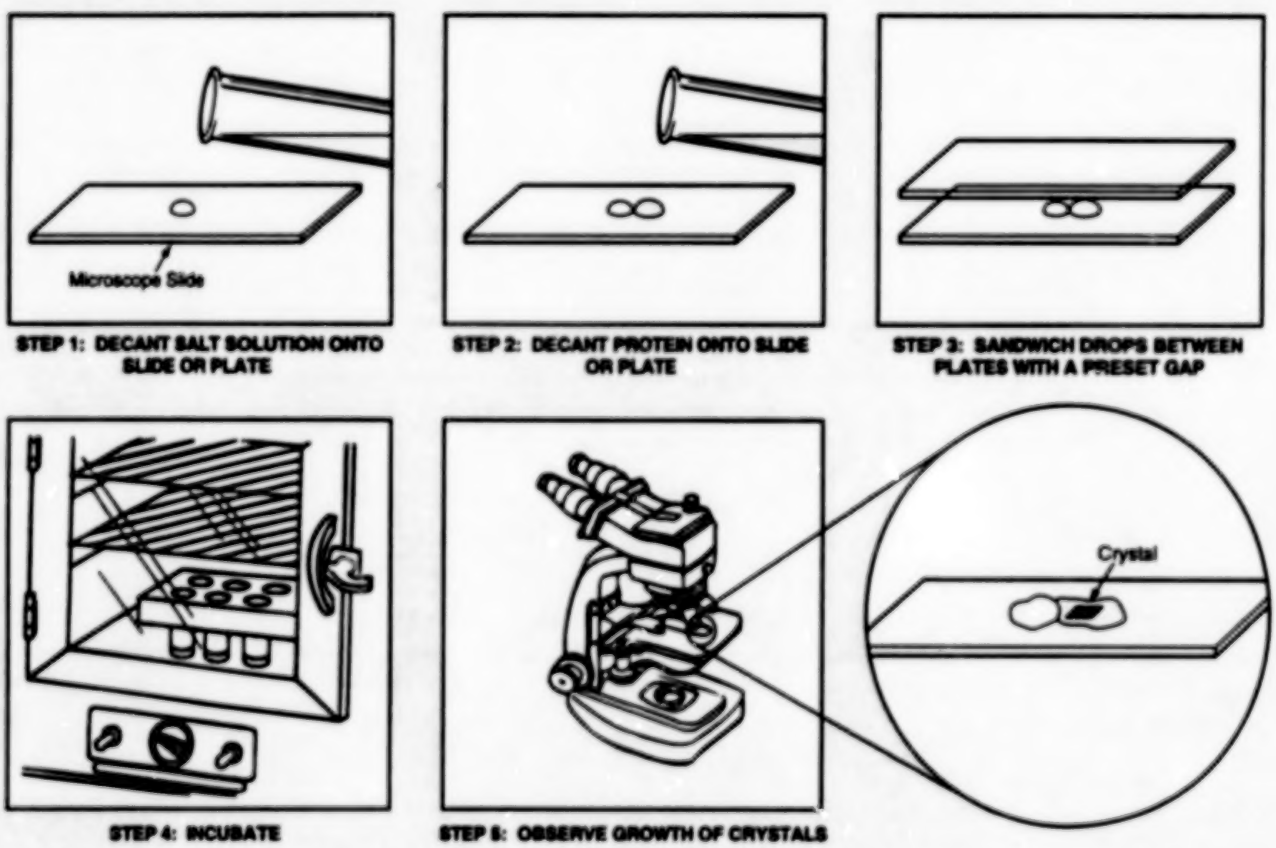
Microscope Slide
STEP 1: DECANT SALT SOLUTION ONTO SLIDE OR PLATE
STEP 2: DECANT PROTEIN ONTO SLIDE OR PLATE
STEP 3: SANDWICH DROPS BETWEEN PLATES WITH A PRESET GAP
STEP 4: INCUBATE
STEP 5: OBSERVE GROWTH OF CRYSTALS
Crystal

Protein Crystallizes by Liquid/Liquid Diffusion between a drop of protein solution and a drop of salt solution between two microscope slides.

An experiment has demonstrated the feasibility of a method of crystallizing proteins in thin, nearly two-dimensional wafers. The method exploits a combination of capillary action and diffusion within a growth chamber or well bounded by two smooth, closely spaced, parallel plates. The ability to produce thin, nearly two-dimensional crystalline protein wafers raises the possibility of novel applications in optoelectronics and electron microscopy in biomolecular systems.

The method (see figure) is best explained by describing the experiment, in which tetragonal crystals of lysozyme were grown from an aqueous solution of 4 percent lysozyme and 2 percent sodium chloride, and with sodium acetate as a buffer that was used to titrate the solution to pH 4.0. A drop of this solution was placed in one of two hemispherical depressions on an otherwise flat glass microscope slide; a drop of an aqueous solution of sodium chloride in greater concentration (to serve

as a precipitating solution) was placed in the other depression. Then a second, flat glass microscope slide was placed on top of the first slide, along with spacers to maintain a gap of 30 μm.

By capillary action, both solutions were drawn from the depressions and spread across the plates in the gap. Eventually, the two solutions met, forming a nearly one-dimensional contact front. At this front, protein crystals grew by what amounted to an approximately two-dimensional version of the established liquid/liquid-diffusion method. The lysozyme crystals that were formed along the front were nearly two-dimensional.

One of the advantages of the small-gap, parallel-plate configuration is that it inhibits the undesired mixing of the two solutions that occurs in the older three-dimensional version of the liquid/liquid-diffusion method. Another advantage of this configuration is that it is well-suited for optical observations and measurements of rates of growth. Yet another advantage is that the thickness of the crystalline protein wafer can be chosen to produce desired effects; for example, in some cases, crystals of higher quality can be obtained by making the wafers thinner.

Because of the predominance of capillarity and liquid/liquid diffusion in this method, gravitation and bulk diffusion exert little or no discernable effect on the crystallization process and thus their adverse effects on the quality of crystals are eliminated. Still another advantage of the present approach is that it provides an additional degree of freedom for optimizing crystallization conditions; for example, the parallel plates can be coated with films that repel or are preferentially wetted by selected constituents of protein solutions.

This work was done by David A. Noever of **Marshall Space Flight Center**. *Further information is contained in a TSP [see page 1].*

Inquiries concerning rights for the commercial use of this invention should be addressed to the Patent Counsel, Marshall Space Flight Center [see page 1]. Refer to MFS-31048.

National Aeronautics and
Space Administration

END

10\08\98